FABRICATION AND CHARACTERIZATION OF INTERPENETRATING METAL/TERNARY CARBIDE COMPOSITES

A Dissertation

by

LIANGFA HU

Submitted to the Office of Graduate and Professional Studies of
Texas A&M University
in partial fulfillment of the requirements for the degree of

DOCTOR OF PHILOSOPHY

Chair of Committee,	Miladin Radovic
Co-Chair of Committee,	Ibrahim Karaman
Committee Members,	Karl T. Hartwig
	Sean M. McDeavitt
Head of Department,	Ibrahim Karaman

May 2015

Major Subject: Materials Science and Engineering

ABSTRACT

Advances in various aerospace and energy technologies call for new, multifunctional materials capable of operating under conditions that are challenging to the most advanced high-temperature metallic alloys. Composites that combine attributes of both the ceramics and metals, specifically metal/ternary carbide composites, hold the greatest promise to provide such multi-functionalities. These composites have not been made because of fabrication limitations. Further explorations of their multi-functionalities are necessary. The present work concerns such composites, develops two fabrication methods (*i.e.* infiltration and powder metallurgy), and explores multi-functionalities of the newly developed composites.

The prospect of extending fabrication methods to develop new, highly reactive metal/ternary carbide composites is examined in the present work. Controlled microstructures in metal/ternary carbide composites were obtained using the carbide foams with controlled pore structures and metal infiltration. The resulting composites were lightweight and displayed exceptional mechanical properties at both ambient and elevated temperatures. Aluminum alloy 6061 (AA6061)/Ti_2AlC composites with different alloy contents and metallic phase sizes were processed and characterized. These structures achieved a compressive strength that is 3.5 times higher than the yield strength of peak-aged AA6061 at room temperature and 14 times higher at 400 ^{o}C. Strengthening mechanisms are described together with further strengthening strategies.

Spark plasma sintering (SPS) —a rapid sintering technique — was used to fabricate shape memory alloy/ternary carbide composites. Conventional methods are challenged to fabricate such composites because of severe and detrimental reactions. NiTi/Ti_2AlC and NiTi/Ti_3SiC_2 powder mixtures were processed in the 960–1100 ^oC temperature range under 100–300 MPa for 3–30 minutes. Phase transformation behavior of the composites was studied using differential scanning calorimetry and was compared with starting powders to evaluate the transformable NiTi in the composites. We studied the effects of starting materials and processing conditions (sintering temperature, soaking time, and sintering pressure) on densification, reaction, and transformation behavior. A high-pressure run produced a fully-dense NiTi/Ti_3SiC_2 composite with a maximum percent of transformable NiTi. We developed reaction mechanisms based on phase analysis of the interfacial reaction layers. It is clearly shown that SPS is a viable technique to fabricate highly reactive ceramic-metal systems with active components.

To my wife, my parents, and my sister who have given tremendous support and motivation at all times

ACKNOWLEDGEMENTS

I would like to express my respect and gratitude to my dissertation advisors, Dr. Miladin Radovic and Dr. Ibrahim Karaman, for believing in me and giving me the chance of pursuing a doctoral degree. During my four years of education and research, they have been role models for me with their unparalleled discipline, perseverance, and hard work in every aspect of life and their great enthusiasm for research.

I would like to thank Dr. Karl T. Hartwig and Dr. Sean M. McDeavitt for serving on my committee and giving valuable suggestions during my studies.

I would like to thank all the colleagues I worked with over the years, who made my stay in College Station a memorable one. These colleagues include Dr. M. Lizcano, Dr. S. Basu, R. Benitez, Dr. J. Ma, P. Gao, H. Gao, A. Kothalkar, A. Bolon, J. Xing, Dr. A. Bandyopadhyay, Dr. J.A. Monroe, Dr. E. Dogan, N. Barta, C. Hayrettin, L.W. Tseng, N. Bruno, Dr. R. Zhu, M. Kaynak, Dr. A. Evirgen, B.E. Franco, H. Ozcan, O. Karakoc, Dr. S. Wang, and T. Jozaghi. I also want to extend my gratitude to the U.S. Air Force Office of Scientific Research, which provided the funding throughout my Ph.D. research.

Last but not least, I am forever indebted to the continuous support and courage from my wife, my parents, and my sister. This dissertation would never have started or ended without their support.

NOMENCLATURE

CTE	Coefficient of thermal expansion
BPD	Basal plane dislocations
MDW	Mobile dislocation walls
IKB	Incipient kink bands
KB	Kink bands
BPT	Brittle-to-plastic transition
SMA	Shape memory alloys
FE	Finite element
K_{Ic}	Fracture toughness
SPS	Spark plasma sintering
FE-SEM	Field emission scanning electron microscopy
EDS	Energy Dispersive Spectroscopy
EBSD	Electron Backscatter Diffraction
XRD	X-ray diffractometer
JCPDS	Joint Committee on Powder Diffraction Standards
ICSD	Inorganic Crystal Structure Database
DSC	Differential scanning calorimetry
WDS	Wavelength dispersive spectrometry
RUS	Resonant ultrasound spectroscopy
WDS	Wavelength dispersive spectrometry

PS	Pressureless sintering
HIP	Hot isostatic pressing
HP	Hot pressing
AM	Arc melting
CRS	Combustion reaction synthesis
G	Shear modulus
v	Poisson's ratio
E	Young's modulus
B	Bulk modulus
γ	Surface energy
c	Pore size
IPF	Inverse pole figure
SHT	Solution heat treated
PA	Peak aged
AA6061	Aluminum alloy 6061
IPC	Interpenetrating phase composite
ROM	Rule of mixture
FE	Finite element
RVE	Representative volume element
EDM	Electric discharge machining
LFA	Laser flash analyzer
DSC	Differential scanning calorimeter

EMT	Effective media theory
KNE	Kinking nonlinear elastic
LFA	Laser flash analyzer
W_d	Dissipated energy per unit volume per cycle
ε_P	Irrecoverable strain

TABLE OF CONTENTS

Page

ABSTRACT....ii

DEDICATION....iv

ACKNOWLEDGEMENTS....v

NOMENCLATURE....vi

TABLE OF CONTENTS....ix

LIST OF FIGURES....xii

LIST OF TABLES....xx

CHAPTER I. INTRODUCTION AND LITERATURE REVIEW....1

1.1. MAX Phases....1
1.2. Metal/MAX Phase Composites....6
1.2.1. Shape Memory Alloy/MAX Phase Composites....10
1.2.2. Al Alloy/MAX Phase Composites....11

CHAPTER II. MOTIVATION AND OBJECTIVES....14

CHAPTER III. EXPERIMENTAL METHODOLOGY....17

3.1. Shape Memory Alloy/MAX Phase Composites....17
3.1.1. Sample Preparation....17
3.1.2. Density Measurement....19
3.1.3. Microstructural and Compositional Analysis....19
3.1.4. Calorimetry....20
3.1.5. Sample Designation....21
3.2. Al Alloy/MAX Phase Composites....23
3.2.1. Sample Preparation....23
3.2.2. Density Measurement....24
3.2.3. Microstructural and Compositional Analysis....25
3.2.4. Uniaxial Compression Tests....26

CHAPTER IV. FABRICATION AND CHARACTERIZATION OF TERNARY CARBIDE FOAMS WITH CONTROLLED POROSITY AND PORE SIZE....27

4.1. Introduction 27
4.2. Experimental Details 29
4.3. Results and Discussion 33
4.3.1. Phase Analysis 33
4.3.2. Characterization of Porosity 35
4.3.3. Microstructure and Pore Size Distribution 38
4.3.4. Ti_2AlC Foams with Graded Porosity 43
4.3.5. Mechanical Properties 43
4.3.6. Thermal Properties 50
4.4. Summary and Conclusions 52

CHAPTER V. A RAPID INFILTRATION APPROACH TO HIGH-PERFORMANCE METAL/TERNARY CARBIDE COMPOSITES WITH CONTROLLED MICROSTRUCTURES 54

5.1. Introduction 54
5.2. Experimental Details 57
5.3. Results and Discussion 59
5.3.1. Microstructural Characterization 59
5.3.2. Compositional, Phase, and Texture Analyses 63
5.3.3. Compressive Properties 72
5.4. Summary and Conclusions 81

CHAPTER VI. ON THE ENERGY DISSIPATION OF METAL/TI2ALC COMPOSITES UNDER CYCLIC, COMPRESSIVE LOADING 83

6.1. Introduction 83
6.2. Experimental Details 87
6.2.1. Materials and Sample Preparation 87
6.2.2. Characterization 88
6.2.3. Analysis—the “Two-Bar” Model 89
6.3. Results and Discussion 91
6.3.1. Compressive Stress-Strain Curves 91
6.3.2. Load Partitioning According to the Isostrain Calculation 97
6.3.3. Energy Dissipation: Experiments and Calculation 99
6.3.4. Application of the “Two-Bar” Model 100
6.4. Summary and Conclusions 103

CHAPTER VII. FABRICATION AND CHARACTERIZATION OF SHAPE MEMORY ALLOY/TERNARY CARBIDE COMPOSITES 104

7.1. Introduction 104
7.2. Experimental Details 107
7.3. Results and Discussion 112
7.3.1. SPS Consolidation of SMA/MAX Phase Powder Mixtures 112

7.3.2. Phase Identification: XRD Results 115
7.3.3. Optimization of Processing Conditions and Starting Materials 115
7.3.4. Phase Analysis and Reaction Mechanisms 119
7.3.5. Evaluation of Transformable NiTi 127
7.4. Summary and Conclusions 129

CHAPTER VIII. TEMPERATURE-DEPENDENT THERMAL PROPERTIES OF A SHAPE MEMORY ALLOY/TERNARY CARBIDE COMPOSITE: EXPERIMENTS AND MODELING 130

8.1. Introduction 131
8.2. Experimental Details 133
8.2.1. Thermal Diffusivity 134
8.2.2. Specific Heat Capacity at Constant Pressure 135
8.2.3. Thermal Conductivity 136
8.3. Results and Discussion 137
8.3.1. Thermal Diffusivity 137
8.3.2. Specific Heat Capacity at Constant Pressure 139
8.3.3. Thermal Conductivity 141
8.3.4. Finite Element Modeling 143
8.3.5. Thermal Conductivity: Experiments and Modeling 149
8.3.6. Validation of Predicted Thermal Conductivity of Interfaces 151
8.4. Summary and Conclusions 153

CHAPTER IX. CONCLUSIONS AND FUTURE DIRECTIONS 154

REFERENCES 158

LIST OF FIGURES

Page

Figure 1. Unit cells of $M_{n+1}AX_n$ phases for (a) n=1 or M_2AX, (b) n=2 or M_3AX_2, and (c) n=3 or M_4AX_3. [1] 2

Figure 2. Ti-Al-C ternary phase diagram at 727 ºC [54]. Conventional methods are challenged to preserve constituents in the Al-Ti_2AlC system, because the reaction of Al with Ti_2AlC — that is, moving along line 1 — should shift the overall composition into the Ti_2AlC-$TiAl_x$-TiC_x compatibility triangle. The proposed CAPAI method provides controlled reaction between liquid aluminum and solid carbide, offers the opportunity for rapid processing with compositional and microstructural control, and could be viable to realize materials that are far from equilibrium, *e.g.* Al/Ti_2AlC in this case, with potentially unprecedented properties. 8

Figure 3. Schematic of a rapid infiltration approach showing the coupled current/pressure (item 1), the graphite die set (items 2 and 5), and the 'sandwich'-like set-up of the metal (item 3) and porous preform (item 4). 24

Figure 4. FE-SEM images of (a) Ti_2AlC powders with particle sizes of 45–90 μm, and (b) NaCl powders with particle sizes of 180–250 μm. The inset illustrates the nanolaminated structure of the ternary carbide. 30

Figure 5. Typical XRD spectra of starting Ti_2AlC powder and sintered Ti_2AlC foams prepared with 40 vol.% of NaCl powders. The particle sizes of the NaCl powders are 355–500 μm. The identification of phases was according to the ICSD collection code 165460 for Ti_2AlC, 153266 for Ti_3AlC_2, 10425 for Al_2O_3 and 44494 for TiC. 33

Figure 6. Variations of overall and open porosities with volume percent of NaCl pore former. Particle sizes of NaCl pore former: (a) 45–90 μm, (b) 180–250 μm, and (c) 355–500 μm. (d) a comparison of overall porosity in all samples. Insets show the open/overall porosity ratio as a function of volume percent of NaCl pore former. 37

Figure 7. Variation of overall porosity with the particle size of Ti_2AlC powders. Both samples were processed with 80 vol.% NaCl pore former (180–250 μm particle sizes).....38

Figure 8. SEM images of Ti_2AlC foams with different pore sizes formed by addition of 60 vol.% NaCl pore former with different particle sizes: (a) 45–90 μm, (b) 180–250 μm, and (c) 355–500 μm. (d) shows typical microstructure of fracture surface (60 vol.% pore former with particle sizes of 180–250 μm). The overall porosity is comparable: (a) 56.0 vol.%, (b) 50.9 vol.%, (c) 50.6 vol.%, and (d) 50.9 vol.%.....39

Figure 9. Pore size distribution of Ti_2AlC foams with different pore sizes formed by NaCl powders with different particle sizes: 45–90 μm, 180–250 μm, and 355–500 μm.....40

Figure 10. SEM images of Ti_2AlC foams with increasing porosity: (a) 9.3 vol.%, (b) 23.6 vol.%, (c) 39.3 vol.%, and (d) 56.0 vol.%. Sample (b), (c) and (d) were processed from NaCl pore former with the same particle size (45–90 μm). 42

Figure 11. Micrograph of the Ti_2AlC foams with graded porosity. The particle size of the NaCl pore former: 180–250 μm. The overall porosity: 33.2 vol.%. 42

Figure 12. (a)Young's and (b) shear moduli of Ti_2AlC as functions of porosity. Dots are experimental data determined from the SPS samples (triangle, green), HIP samples (square, purple) [96], and PS samples (round, blue). Also included are the predictions from the CSM model (dash, blue line), Hasselman model (dash, black line), and exponential model (solid, red line).....46

Figure 13. (a) Relative compressive strength of Ti_2AlC as a function of porosity. The loading direction is normal to aligned pore axis. Dots are experimental data of a HIP sample (square, red) [96] and PS samples (round, black). Also included are the corresponding data for Al_2O_3 (dash, blue line) [101] and Si_3N_4 (dash, red line) [103]. Compression samples after testing: (b) a Ti_2AlC sample processed without using NaCl pore former, porosity = 21%; (c) a Ti_2AlC sample processed using 20 vol.% NaCl pore former (355–500 μm), porosity = 33%. Teflon tape was applied between sample and fixture to reduce the effects of friction.....47

Figure 14. FE-SEM images of fracture surface of a post-compression sample processed with 40 vol.% NaCl pore former (180–250 μm). The porosity is 41%, and the magnification is: (a) × 430, (b) × 1100, and (c) × 9000. Compressive strength as a function of (d) the particle size of NaCl pore former (the loading direction is normal to aligned pore axis) and (e) loading direction, *i.e.* normal ($\sigma_{\perp}$) and parallel ($\sigma_{//}$) to aligned pore axis. The samples were processed with 20 vol.% NaCl pore former (355–500 μm). (f) Schematic of the loading direction versus the aligned pore axis. 49

Figure 15. Room temperature thermal conductivity versus porosity and pore size (*i.e.* particle size of NaCl pore former). (b) Comparison of the experimental results with the theoretical models (*i.e.* the EMT model and the Maxwell-Eucken upper bound). 51

Figure 16. SEM images of Ti_2AlC foams with different pore sizes fabricated using NaCl particles as pore formers; the ranges of the pore size are (a) 42–83 μm, (b) 77–276 μm, and (c) 167–545 μm. All three foams were fabricated using the same volume fraction (40 vol.%) of the NaCl particles. The infiltration of these three foams with AA6061 resulted in AA6061/Ti_2AlC composites with different interpenetrating phase sizes: (d) 42–83 μm, (e) 77–276 μm, and (f) 167–545 μm; the interpenetrating phase size are formerly pore size in the foams before infiltration. Insets show photographs of both the foams and the composites after electrical discharge machining to dimensions of 3.5 mm × 3.5 mm × 7 mm. Scale bars in optical photograph: 2mm. Scale bars in the SEM images: 100 μm. Scale bars in the photographs: 2 mm. 60

Figure 17. Micro-CT images of the constituents of a cuboid specimen: (a) AA6061, and (b) Ti_2AlC. The dimensions of the cuboid specimen are 1.8 mm × 1.8 mm × 2.3 mm, and the interpenetrating phase size is 167–545 μm. Scale bars: 300 μm. Arrows in an enlarged view of (a) show the connectivity of the Al alloy. 62

Figure 18. (a) XRD results of the AA6061/Ti_2AlC composite and its pure constituents, namely AA6061 and Ti_2AlC. The identification of phases was done according to the Inorganic Crystal Structure Database (ICSD) collection code 165460 for Ti_2AlC, 153266 for Ti_3AlC_2, 10425 for Al_2O_3, and 43423 for Al. (b) Backscattered SEM image of the composite showing AA6061 (1, dark grey), titanium aluminide (2, light grey), Ti_2AlC (3, light), and Al_2O_3 (4, dark). Inset shows a backscattered SEM image at low

magnification. The composition of phases 1, 2, 3, and 4 are determined according to the EDS results (Table 7) and EBSD results (Figure 19). 64

Figure 19. A phase map and four element maps, namely Ti, Al, C, and O, of the AA6061/Ti_2AlC composite with interpenetrating phase sizes of 167–545 μm. Both identified and unidentified phases are color coded in the phase map. 82.0 % of all phases were identified, and 18.0 % were not identified. The identified phases include Ti_2AlC, Ti_3AlC_2, Al, $TiAl_3$, and Al_2O_3. The percent of each phase is listed in Table 8. Scale bars: 100 μm. 66

Figure 20. (a) Atomic percent of the trace elements in solution heat treated (SHT) AA6061 and Al alloy in the composites. (b) A back scattered SEM image showing phase distribution (dark grey: Al alloy, grey: $TiAl_3$, and light: Ti_2AlC) around the Al alloy-Ti_2AlC interfaces inside the composites. (c) An X-ray map showing Si diffusion from Al alloy to the Ti_2AlC. Red crosses annotate locations where microprobe quantitative analyses were carried out. The quantitative analyses results are shown in Table 9. 69

Figure 21. (a) A typical inverse pole figure (IPF) map of grains in the as-processed composites. Grain with uniform colors denote ones in which little evidence for plastic deformation was observed (which is mostly the case for the ceramic grains). The rainbow colored grains (which are almost all the aluminum grains), on the other hand, indicate ones in which plastic deformation occurred and has resulted in local misorientations. (b) A zoom-in image of the region within the rectangular frame in (a); the region is labeled as area A. (c) trace of the misorientation angle along line B in 5(b), indicating that significant deformation occurred in the AA6061 grain. Scale bars: 100 μm. 71

Figure 22. (a) Typical compressive stress-strain curves of Ti_2AlC, 27%Al alloy/Ti_2AlC, and 40%Al alloy/Ti_2AlC. (b) Ultimate strength of Ti_2AlC, 27%Al alloy/Ti_2AlC, and 40%Al alloy/Ti_2AlC. (c) Ultimate strength and failure strain of the composites with different interpenetrating phase sizes. (d) Open and closed porosities of the composites as a function of interpenetrating phase size. The interpenetrating phase size is formerly the pore size of the Ti_2AlC foams. 72

Figure 23. (a) Typical compressive stress-strain curves of the 27%AA6061/Ti_2AlC composites, solution heat treated (SHT)

AA6061, and Ti_2AlC foam. (b) Specific strength of the AA6061/Ti_2AlC composites, peak aged (PA) AA6061, and Ti_2AlC foam, the Ti_3AlC_2/Al composites [21], solution heat treated AA6061, and pure aluminum. 74

Figure 24. (a) Compressive stress-strain curves of the 27%AA6061/Ti_2AlC composites and AA6061 at 25 °C and 400 °C. (b) Specific strength as a function of compression test temperature for the 27%AA6061/Ti_2AlC composites from the present study (red curve), Ti_3AlC_2/Al composites [21] (blue curve [1]), B_4C/Al composites [64] (pink curve [2]), Al_2O_3/Al composites [62] (purple curve [3]), and PA AA6061 (black curve)..... 75

Figure 25. Surface morphology of a post-compression composite. Loading direction was vertical. The inset shows that the sample failed by cracking in the direction of approximately 45 ° relative to the loading direction with a tortuous crack path. Cracks in the ceramic phase were arrested ((b), (c), and (e)), deflected ((b) and (c)), or bridged ((d) and (f)) by the metallic phase..... 81

Figure 26. (a) Typical compressive stress-strain curves obtained when Ti_2AlC, 40% Al alloy/Ti_2AlC, and solution heat treated (SHT) Al alloy were cycled three times to a peak stress of 450 MPa, 450 MPa, and 100 MPa, respectively. The pink, dash line represents the yield strength $\sigma_{0.002} = 110(MPa)$ of the SHT Al alloy. The other three plots show compressive stress-strain curves obtained when (b) Ti_2AlC was cycled three times to a peak stress of $\sigma(MPa)$, where $\sigma = 500$, 600, 700, and 800, (c) 27%Al alloy/Ti_2AlC composite was cycled three times up to a peak stress of $\sigma(MPa)$, where $\sigma = 500$, 600, 700, and 800, and (d) 40%Al alloy/Ti_2AlC composite was cycled three times up to a peak stress of $\sigma(MPa)$, where $\sigma = 300$, 350, 400, and 450. The highest peak stress value $\sigma_{\max}(MPa)$ is determined such that $\sigma_{\max}/\sigma_{ucs} \approx 0.7$, where $\sigma_{ucs}(MPa)$ is the ultimate compressive strength. 92

Figure 27. Characteristics of stress-strain curves of Ti_2AlC, 27%Al alloy/Ti_2AlC, and 40%Al alloy/Ti_2AlC: (a) relative Young's modulus E/E_0, (b) irrecoverable strain ε_P, and (c) dissipated energy W_d. All characteristics are illustrated in the inserted schematic. The relative Young's modulus at a stress of σ_c was determined by dividing the Young's modulus of the material after

a cyclic loading at the stress of σ_c with the value of the Young's modulus of the as-processed material. 95

Figure 28. Calculated stresses carried by the individual constituents in (a) 27% Al alloy/Ti_2AlC composites and (b) 40% Al alloy/Ti_2AlC composites as functions of the external applied stress $\sigma_c(MPa)$ and the ratio of σ_c/σ_{ucs}, where $\sigma_{ucs}(MPa)$ is the ultimate compressive strength of the composites. The black, dash lines represent the yield strength $\sigma_{0.002} = 110(MPa)$ of the SHT Al alloy. 98

Figure 29. Dissipated energy per unit volume per cycle, W_d, as functions of the square of the external applied stress σ_c^2 and the external applied stress σ_c of (a) 27%Al alloy/Ti_2AlC composites and (b) 40%Al alloy/Ti_2AlC composites. The bounds calculated according to equation (23) are also plotted in comparison with the experimental results. For the 27%Al alloy/Ti_2AlC composites, the $W_d^2(\sigma_2)\cdot V_2$ in equation (23) is from fully dense Ti_2AlC, because the density measurements show that the density of the 27%Al alloy/Ti_2AlC composites is close to its theoretical density. For the 40%Al alloy/Ti_2AlC composites, the $W_d^2(\sigma_2)\cdot V_2$ in equation (23) is from 7% porous Ti_2AlC, because the density measurements show that the porosity of the 40%Al alloy/Ti_2AlC composites is 7%. 100

Figure 30. (a) Calculated stresses carried by the individual constituents (*i.e.* Mg and Ti_2AlC) of previously reported 50%Mg/Ti_2AlC composites [23] as functions of the external applied stress $\sigma_c(MPa)$ and the σ_c/σ_{ucs}, where $\sigma_{ucs} = 700(MPa)$ [23] is the ultimate compressive strength of the composites. (b) and (c) The W_d as a function of the square of the external applied stress σ_c^2 and the σ_c/σ_{ucs} [23]. The bounds were calculated according to equation (23), where $W_d^2(\sigma_2)\cdot V_2$ is the contribution from a fully dense Ti_2AlC in (b). The bounds were calculated according to equation (23), where $W_d^2(\sigma_2)\cdot V_2$ is the contribution from a 7% porous Ti_2AlC in (c). 101

Figure 31. FE-SEM images of (a) the Ti_2AlC powder, (b) the Ti_3SiC_2 powder, and (c) the NiTi powder. The insets in (a) and (b)

illustrate the nanolaminated structure of Ti_2AlC and Ti_3SiC_2, respectively.....107

Figure 32. (a) Sintering curves (*i.e.* temperature, sintering pressure, and punch displacement as functions of time) of a NiTi/Ti_2AlC powder mixture. (b) Shrinkage curves (*i.e.* punch displacement as a function of time) of the NiTi powder, the Ti_2AlC powder, and the NiTi/Ti_2AlC powder mixture. All samples were processed at 1233 K under 100 MPa for 8 minutes. 113

Figure 33. XRD results of (a) the Ti_3SiC_2 powder, (b) the Ti_2AlC powder, (c) the NiTi powder, (d) A-1233-8, and (e) B-1233-8. All data were collected at room temperature. The identification of phases was done according to the JCPDS card number 27-0344 for B19', as well as ICSD collection code 165460 for Ti_2AlC, 153266 for Ti_3AlC_2, 10425 for Al_2O_3, 44494 for TiC, and 86213 for Ti_3SiC_2. 114

Figure 34. Back scattered SEM images of (a) A-1233-8, (b) A-1233-20, (c) A-1233-30, (d) A-1253-10, and (e) A-1273-3. The insets show lower magnification micrographs. Plots (f) and (g) show the relative density and interface thickness.....116

Figure 35. Back scattered SEM images of (a) A-1233-20 and (b) B-1233-20. The insets show low magnification micrographs. Dash lines were added to highlight the interfaces. 117

Figure 36. (a) The relative density of NiTi/Ti_3SiC_2 composites as a function of sintering pressure. Back scattered SEM images of (b) A-1233-8 and (c) B-1233-8‡ (sintered at a higher pressure of 300 MPa). The insets show lower magnification micrographs. Dash lines were added to highlight the interfaces.....118

Figure 37. (a) A SEM image of B-1233-8. EBSD phase maps of regions (b) A and (c) B. 119

Figure 38. (a) Back scattered SEM images of A-1233-30. The inset shows a lower magnification micrograph. (b) EDS line profiles for Ti, Al, and Ni across the interface. (c) An EBSD phase map at interfacial area. 121

Figure 39. (a) DSC curves of the NiTi powder, B-1233-8, and A-1233-8. Both samples were processed at 1233 K under 100 MPa for 8 minutes. (b) The percent of transformable NiTi (W_{trans}) as a function of soaking time for both the NiTi/Ti_3SiC_2 and NiTi/Ti_2AlC composites.....128

Figure 40. Temperature dependency of the thermal diffusivity upon heating in 300–1224 K range for the NiTi/Ti_3SiC_2 composite. Also included are the corresponding data for monolithic NiTi and Ti_3SiC_2 which were fabricated separately. 137

Figure 41. Temperature dependencies of specific heat (C_p) upon heating in 300–600 K range for the NiTi/Ti_3SiC_2 composite and its pure constituents, *i.e.* NiTi and Ti_3SiC_2. Specific heat at higher temperatures than 600 K was not measured due to the instrument limitation. M: martensite, and A: austenite. 139

Figure 42. Temperature dependencies of thermal conductivity upon heating in 300–600 K range for the NiTi/Ti_3SiC_2 composite and its pure constituents, *i.e.* NiTi and Ti_3SiC_2. 142

Figure 43. Back scattered SEM images showing (a) phase distribution and morphology and (b) interface. 3-D RVEs of the NiTi/Ti_3SiC_2 composite: (c) in configuration A, grey represents pore, pink NiTi, and transparent Ti_3SiC_2; (d) in configuration B, grey represents pore, pink NiTi, transparent Ti_3SiC_2, and cyan interface; (e) FE meshes on the configuration A RVE; and (f) FE meshes on the configuration B RVE. 145

Figure 44. Temperature-dependent thermal conductivity of the NiTi/Ti_3SiC_2 composite: comparison between experiment and simulation results. Simulations results based on both configuration A and B are shown. 150

Figure 45. Temperature dependencies of thermal conductivity upon heating in 300–600 K range for the NiTi/Ti_3SiC_2 composite (measured), interface in the composite (FE predicted), and interface in the NiTi-Ti_3SiC_2 bilayer (FE predicted). 152

LIST OF TABLES

Page

Table 1. Metal/MAX phase composites investigated to date. Processing methods include: PS—pressureless sintering, HIP—hot isostatic pressing, HP—hot pressing, AM—arc melting, CRS—combustion reaction synthesis, and SPS—spark plasma sintering.....6

Table 2. Starting powder, sintering temperature, soaking time, relative density, interface thickness, percent of transformable NiTi ($W_{trans.}$), and phase transformation temperature (M_s) of all composites.....22

Table 3. Molar percent of phases in the starting Ti_2AlC powders and sintered Ti_2AlC foams as determined by the relative intensity of the highest XRD peaks of each phase. 34

Table 4. Pore sizes of Ti_2AlC foams with comparable porosities. Average pore size and standard deviation were determined from the measured values as $\bar{x} = \frac{1}{N}\sum_{i=1}^{N} x_i$ and $s = \sqrt{\frac{1}{N}\sum_{i=1}^{N}(x_i - \bar{x})^2}$ respectively, where N is the total number of values measured from SEM images, x_i is the pore size, and $\bar{x}$ is the average pore size.....40

Table 5. Particle size of starting Ti_2AlC powder, pore former size and volume percent, sintering method, dimensions of testing samples, density ρ, porosity P, shear modulus G, Young's modulus E, Poisson's ratio v, and bulk modulus B of all tested samples for elastic moduli. 45

Table 6. Empirical constant (b) and coefficient of correlation (R^2) from the regression analysis of the experimental data and the model values.....46

Table 7. EDS results of spot analysis in Figure 18(b). EBSD results from Figure 19 are also listed for comparison. 65

Table 8. Color and percent of phases in the phase map of Figure 4. 67

Table 9. Microprobe quantative analyses results of locations 1 and 2 in Figure 20. 70

Table 10. Compressive properties, *i.e.* yield strength, ultimate strength, and failure strain, at both room and elevated temperatures of a number of aluminum-ceramic composites. 77

Table 11. Starting powder, sintering temperature, soaking time, relative density, interface thickness, percent of transformable NiTi, and transformation temperature of all composites. 111

Table 12. EDS spot analysis results of the locations 1–7 in Figure 38(a). EBSD results of the corresponding regions are listed. 123

Table 13. The specific heat of NiTi and Ti_3SiC_2 in 300–600 K range in comparison with the literature data. 140

Table 14. Thermal conductivity of NiTi and Ti_3SiC_2 in 300–600 K range in comparison with the literature data. 143

Table 15. Volume percent of constituents (*i.e.* Ti_3SiC_2, NiTi, pore, and interfacial layer) in the NiTi/Ti_3SiC_2 composites. 147

Table 16. FE results of temperature-dependent thermal conductivity along different temperature-gradient directions, *i.e.* x, y, and z. 149

CHAPTER I

INTRODUCTION AND LITERATURE REVIEW

Advances in various fields, such as aerospace, transportation, power generation, and energy conversion, call for new, multi-functional, structural materials capable of operating under conditions that are challenging to even the most advanced high-temperature metallic alloys. Composites that combine attributes of both the ceramics and metals, specifically metal/ternary carbide composites in the present study, hold the greatest promise to provide such multi-functionalities. This chapter summarizes previous literature related to the objectives of the present study and provides background for the reader to better interpret the experimental results. This literature review is presented in the same order as the objectives presented in Chapter II.

1.1. MAX Phases

In the last 15 years, a new class of ceramics has emerged and has challenged the typical description of ceramics as materials that are hard, difficult to machine, and susceptible to damage and thermal shock. This new class of ceramics—known as the MAX phases—is a family of ternary carbides and nitrides that not only have many chemical and physical properties in common with their binary counterparts, but also show some unique properties that are more typical of metals than ceramics. The MAX phases are defined by their chemical formula and crystal structure listed below [1]:

1. Common chemical formula $M_{n+1}AX_n$, where n = 1, 2, or 3, M is an early transition metal (Sc, Ti, V, Cr, Zr, Nb, Mo, Hf, or Ta), A is an A-group element mostly from groups 13–16 (Al, Si, P, S, Ga, Ge, As, In, Sn, Tl, Pb, or Cd), and X is C and/or N;
2. Nano-layered, hexagonal crystal structure (space group P63/mmc) with two formula units per unit cell. The X atoms fill the octahedral sites between the closely packed M layers, forming edge-sharing M_6X octahedra. The A-group elements are located at the centers of trigonal M-prisms. Every unit cell consists of alternating layers of the M_6X octahedra and group-A elements (Figure 1 [1]).

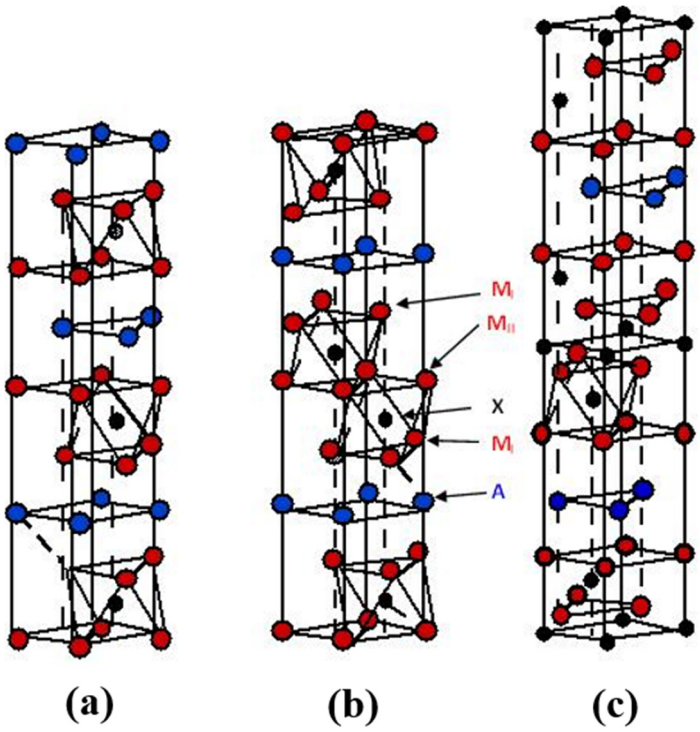

Figure 1. Unit cells of $M_{n+1}AX_n$ phases for (a) n=1 or M_2AX, (b) n=2 or M_3AX_2, and (c) n=3 or M_4AX_3. [1]

Depending on stacking sequences of M_6X octahedra and A-elements layers, the MAX phases can be divided into: (i) M_2AX phases when n = 1 (Figure 1a), (ii) M_3AX_2 phases when n=2 (Figure 1b), and (iii) M_3AX_2 phases when n=3 (Figure 1c) [1]. The MAX phases with more complex stacking sequences, *e.g.* M_5AX_4, M_6AX_5, and M_7AX_6, have also been reported [2, 3]. Apart from over 60 MAX phases that contain one of each the M, A, and X elements, the number of solid solutions on M, A, or X sub-lattices is practically indefinite for the MAX phases. Although Nowotny and co-workers [4] discovered most of the MAX phases in powder form about 40 years ago, Barsoum and El-Raghy's report in 1996 [5] on the synthesis and the unusual properties of bulk Ti_3SiC_2 renewed interest in the MAX phases.

The main reason for the growing interest in the MAX phases in general, and their utilization in ceramic-metal composites in particular, lies in their unusual and sometimes unique set of chemical, physical, and mechanical properties. These properties can be traced back not only to their layered crystal structure, but also to their electronic structure and characteristics of atomic bonding. Recent efforts on theoretical modeling of electronic structure and chemical bonding in the MAX phases showed that [6-14]: (i) similar to their corresponding binary carbides and nitrides (MX), atomic bonding in the MAX phases has a combination of metallic, covalent, and ionic characters; (ii) the M and X atoms form strong, directional covalent bonds in the M_6X octahedra layers that are comparable to those in the MX binaries; (iii) M–d–M–d metallic bonding dominates the electronic density of states at the Fermi level, $N(E_F)$; (iv) in most MAX phases, the M–A bonds are relatively weaker than the M–X bonds, which is particularly important

for the processing of the MAX phase-based composites, because relatively weakly bonded A elements are the most reactive.

Given the similarities between some aspects of the atomic bonding in the MX compounds and MAX phases, it is not surprising that they share many common properties. Like their corresponding MX compounds, the MAX phases are elastically stiff (Young's modulus, 178–362 GPa) [15], thermally conductive (thermal conductivity, 12–60 W/m·K), and electrically conductive (electrical resistivity, 0.2–0.7 μΩ·m) [16]. Both MX compounds and MAX phases have relatively low coefficients of thermal expansion (CTE, $11–14\times10^{-6}$ K^{-1}) [1]. They are also resistant to chemical attack, and some of them (*e.g.* Ti_3SiC_2) are quite refractory with decomposition temperatures above 2300 °C. In most cases, the MAX phases are relatively lightweight materials with densities in the 4–5 g/cm^3 range. Lastly, the MAX phases oxidize at high temperatures, and their oxidation resistance depends on the nature of M oxides and A oxides. The most oxidation-resistant MAX phase is Ti_2AlC, because it forms a stable and protective Al_2O_3 layer that can withstand thermal cycling up to 1350 °C for 10000 cycles without spallation or cracking [17].

The mechanical properties of MAX phases cannot be more different from those of the corresponding MX compounds. The MAX phases are relatively soft (Vickers hardness, 2–8 GPa [15]), readily machinable, thermal shock resistant, and damage tolerant. The room-temperature fracture toughness (K_{Ic}, 5–20 MPa·m$^{1/2}$ [1]) of MAX phases is quite respectable when compared with those of common ceramics. The MAX phases are pseudo-ductile when loaded under confined deformations or elevated

temperatures, but are brittle at room temperature, especially when loaded in tension at room temperature [1]. Only basal plane dislocations (BPD) are abundant, mobile, and able to multiply in the MAX phases at ambient temperature [18]. However, their confinement to the basal planes results in an important and unique deformation micro-mechanisms, *i.e.* formation of dislocation pile-ups, mobile dislocation walls (MDW), incipient kink bands (IKB), and kink bands (KB) during loading [19].

Although the MAX phases are elastically stiff, the formation and annihilation of IKB during cyclic loading lead to fully reversible, hysteretic stress-strain loops [19]. For example, Ti_3SiC_2 can be compressed to stresses as high as 1 GPa at room temperature and fully recover upon removal of the load while dissipating 25% of the mechanical energy [19]. The practical implication of this phenomenon for structural applications cannot be overestimated, because the MAX phases can dissipate a large portion of harmful structural vibrations or acoustic loads. At higher temperatures, they undergo a brittle-to-plastic transition (BPT) and can be plastically deformed to more than 25% strain before failure in tension [20]. In other words, they creep above the BPT temperature, which is around 1000 ^{o}C for most of the MAX phases. In fact, the creep resistance of the MAX phases is good when compared to other creep-resistant materials [16]. The characteristics and properties listed above suggest a “semi-metallic” nature of the MAX phase.

1.2. Metal/MAX Phase Composites

It is the "semi-metallic" nature of MAX phases that has stimulated the development of more than a dozen metal/MAX phase composites. These metal/MAX phase composites are listed in Table 1. The rationale for using the MAX phases is to utilize their unusual properties for (i) light-weight composites with exceptional mechanical damping, high specific strength, and good oxidation resistance, (ii) low friction resistance, low wear resistance, and (iii) electrically conductive composites with improved mechanical properties when compared to conductive metals.

Table 1. Metal/MAX phase composites investigated to date. Processing methods include: PS—pressureless sintering, HIP—hot isostatic pressing, HP—hot pressing, AM—arc melting, CRS—combustion reaction synthesis, and SPS—spark plasma sintering.

Composite systems			Processing method	Reference(s)
Metal		MAX phase		
Light metals	Al	Ti_3AlC_2	PS or HIP	[21]
	Al alloy	Ti_2AlC	Infiltration	[22]
	Mg	Ti_2AlC	Infiltration, HIP	[23]
	Mg	Ti_3SiC_2	HIP	[24]
Transitional metals	Ag	Ta_2AlC, Cr_2AlC	HIP	[25-27]
	Cu	Ti_3SiC_2, Ti_3AlC_2, Ti_2SnC	SPS or HP	[28-32]
	W	Ti_3AlC_2	SPS	[33]
	Ni or Co	Ti_3SiC_2	PS	[34]
	Ti	Ti_3SiC_2	HP	[35]
Intermetallic compounds	TiAl, TiAl(Cr), TiAl(Nb), TiAl(Mn)	Ti_2AlC, Ti_2AlN	CRS, AM, or HP	[36-46]
	NiAl	Ti_3SiC_2	SPS	[47]
	NiTi	Ti_3SiC_2, Ti_2AlC	SPS	[48-50]
	$Nb_5(Si, Al)_3$	Nb_4AlC_3	SPS	[51]

Conventional methods used to fabricate the metal/MAX phase composites include powder metallurgy, infiltration, stir casting, diffusion bonding, and deposition [52]. Infiltration of molten metals into porous ceramic preforms, one of the most popular methods, can be divided into two categories: (i) pressureless infiltration, where molten metals wet the preforms sufficiently to be spontaneously drawn into the preforms, and (ii) pressure infiltration, in which an external pressure is used to actively drive molten metals into the preforms [52]. One problem with pressureless infiltration is poor wettability of preform substrate with molten metal, which slows infiltration and sometimes makes infiltration impossible. Poor wetting can also yield weak bonding between metals and preforms, resulting in inferior mechanical properties of the composites [53]. This problem can be overcome by using pressure infiltration to force molten metals into the preforms. However, new phases could form even in pressure infiltration because of rapid reactions. The new phases not only cage the pores to prevent further infiltration, but also degrade constituents of the composites. Therefore, reducing the severe and detrimental reactions and preserving constituents during high-temperature processing are the most challenging fabrication issues.

One of the fundamental challenges related to the fabrication of such novel composites is to understand reaction mechanisms and kinetics and to control reaction rate, which are crucial in controlling the composition and microstructure to yield tailored and sometimes unprecedented properties. It is particularly challenging to maintain the stoichiometry of the MAX phase — a lined-up compound only that only exists in a narrow compositional range, as illustrated in Figure 2 in the case of Ti-Al-C [54].

Addition of M and A elements results in a multi-phase equilibrium composition, including the MAX phase, MA intermetallic, M(A) solid solutions and/or different binary (MX or AX) compounds, and other ternary carbides (*e.g.* M_3AX).

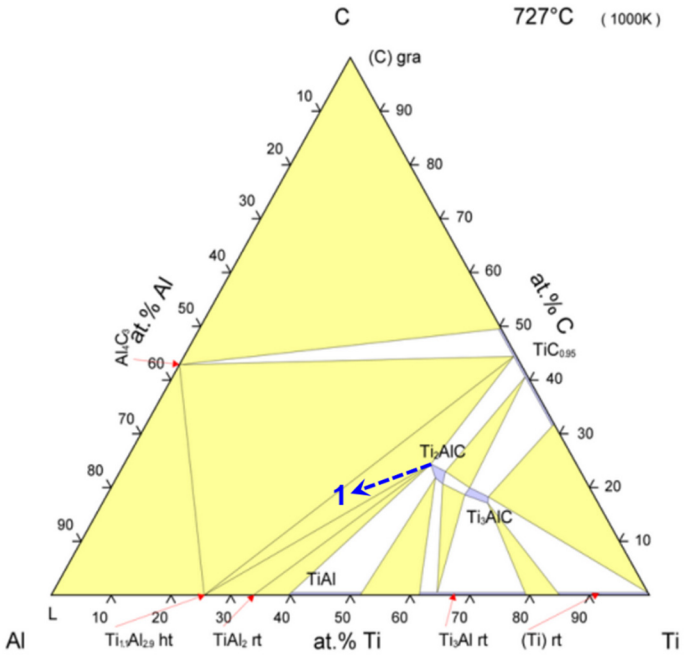

Figure 2. Ti-Al-C ternary phase diagram at 727 ºC [54]. Conventional methods are challenged to preserve constituents in the Al-Ti_2AlC system, because the reaction of Al with Ti_2AlC — that is, moving along line 1 — should shift the overall composition into the Ti_2AlC-$TiAl_x$-TiC_x compatibility triangle. The proposed CAPAI method provides controlled reaction between liquid aluminum and solid carbide, offers the opportunity for rapid processing with compositional and microstructural control, and could be viable to realize materials that are far from equilibrium, *e.g.* Al/Ti_2AlC in this case, with potentially unprecedented properties.

The present work intends to develop fabrication methods for producing metal/MAX phase composites, where severe and detrimental reactions prohibit application of conventional methods. The development requires fundamental understanding of the steps involved in the processing, namely 1) infiltration kinetics of

the multi-phase reactions, and 2) reaction rate to yield tailored composition and microstructure. This development cannot be overestimated, because it provides controlled multi-phase reactions, offers the opportunity for rapid processing with compositional and microstructural control, and could realize materials that are metastable or even far from equilibrium, *e.g.* Al alloy-Ti_2AlC system illustrated in Figure 2. The metastable or far-from-equilibrium materials not only open a new realm of materials that have never been stabilized before, but also allow us to realize a potentially unprecedented combination of lightweight, strength, ductility, and damping. The combination is critical to developing energy efficient technologies, *e.g.* aerospace and transportation, powder generation, and energy conversion.

It would be unrealistic to expect to study all metal/MAX phase composite systems in the limited time frame of the present work. The author focuses on two model systems, namely shape memory alloy (SMA)/MAX phase and Al alloy/MAX phase, because the controllable "processing-composition-microstructure" space helps us to better understand the mechanism and kinetics of multi-phase reactions. The approach and knowledge developed in the model systems are readily applicable to other composite systems and will provide a guideline for future development of new composite materials for energy efficiency in aerospace and transportation, power generation, and energy conversion.

1.2.1. Shape Memory Alloy/MAX Phase Composites

The SMA/MAX phase is a unique system, because both constituents demonstrate two different pseudo-elastic mechanisms. SMAs distinguish themselves from other metals by having two characteristics originating from a reversible, martensitic transformation [55]. First, a two-step operation allows recovering the original shape before mechanical deformation; this operation involves deforming the martensite phase of a SMA and then heating that deformed SMA. The behavior is known as the shape memory effect. Second, an isothermal application of mechanical load to the austenite phase of a SMA at sufficiently high temperatures allows it to transform to its martensite phase. Unloading returns it to the original austenite phase, which is known as pseudo-elasticity. Nickel titanium (NiTi), the most studied SMA, has been implemented in various composite materials due to its high ductility, strength, corrosion resistance, and damping capability [56-58]. Previous efforts have explored high damping capability of such composites as NiTi/TiC [56], Mg/NiTi [57], and NiTiAl/InSn [58]. However, it has never been studied to combine SMAs to another material that demonstrates pseudo-elastic mechanisms.

The motivation to combine SMA with MAX phases in the SMA/MAX phase composites is to achieve a higher damage tolerance and mechanical damping than either SMA or MAX phases alone. It is expected that two benefits would result from combining them in the composites: (i) capability of controlling residual stresses in the composites through their composition, phase morphology, and thermo-mechanical conditioning; (ii) colossal mechanical damping during cyclic loading. Both benefits rely

on the fraction of transformable SMA in the composites. To reach optimum damage tolerance and mechanical damping, the fabrication of the composites must preserve as much transformable SMA as possible; however, severe and detrimental reactions between SMA and MAX phases prohibit the application of conventional methods to fabricate the composites. It has been shown through a series of inter-diffusion experiments that MAX phases highly react with SMA to form thick and complex reaction layers consisting of multiple phases [59, 60]. Further, a slight variation in the composition of SMA during fabrication affects its capability to undergo martensitic transformation that is responsible for the mechanical damping. Once again, the challenge for fabricating the composites is to reduce the severe and detrimental reactions and to preserve constituents during the high-temperature processing.

1.2.2. Al Alloy/MAX Phase Composites

Al alloy is the most attractive metal used in ceramic-metal composite materials for aerospace and transportation applications, where lightweight composite materials are critical. Particularly, development of newer generation aircraft calls for Al alloy with high performance in an extended temperature range. An approach to obtain improved high-temperature properties is to combine Al alloy and ceramics, such as Al_2O_3 [61-63], B_4C [64-66], and SiC [67-69], in composite materials. However, MAX phases have not been used in Al-based composites until recent studies on Ti_3AlC_2/Al [70] and Al alloy/Ti_2AlC [22].

The introduction of MAX phases in Al-based composites brings additional advantages, which could not otherwise be obtained using traditional ceramics (*e.g.* Al_2O_3, B_4C, or SiC). First, a typical MAX phase, like Ti_3SiC_2, has higher fracture toughness (~7 $MPa \cdot m^{1/2}$) than Al_2O_3 (~4 $MPa \cdot m^{1/2}$), B_4C (~3.7 $MPa \cdot m^{1/2}$), and SiC (~4.6 $MPa \cdot m^{1/2}$). The high toughness reduces the sensitivity of the composites to brittle fracture. Second, unlike the traditional ceramics, MAX phases have high transport properties that originate from the atomic bonding with mixed covalent, ionic, and metallic characters. The high transport properties preserve the functional properties of Al, namely thermal and electrical conductivities. Third, MAX phases can be compressed to stresses as high as 1 GPa, fully recover their original shapes upon removal of the stress, and dissipate 25% of the mechanical energy during this process. The addition of MAX phases in Al introduces energy dissipation to the composites, which is unique compared to traditional Al/ceramic composites. Lastly, unlike traditional ceramics, MAX phases are machinable even at room temperature, which reduces the manufacturing cost. Therefore, Al alloy/MAX phase composites deserve further investigation.

As mentioned above, the Al alloy/MAX phase could be an effective approach to improving high-temperature properties of the composites, and the SMA/MAX phase system could achieve a higher damage tolerance and mechanical damping than either SMA or MAX phases alone. Preserving the constituents during high-temperature processing is vital to realizing these advantages. However, the reactions between molten metals and MAX phases are so severe and detrimental to the composite properties that

conventional methods are challenged to realize these composite systems. To solve the problem, two methods, *i.e.* infiltration and powder metallurgy, will be developed. The objectives of developing each method are described below.

CHAPTER II

MOTIVATION AND OBJECTIVES

The overall goal is to develop fabrication approaches for producing selected composite systems, namely SMA/MAX phase and Al alloy/MAX phase, to understand reaction mechanism and kinetics, and to control reaction rate to yield tailored composition and microstructure. The author proposes to use high-throughput, high-temperature synthesis and characterization techniques to investigate structure and thermo-mechanical properties of these materials, as well as to investigate fundamental mechanism and kinetics for the multi-phase reactions during high-temperature processing. The results will develop fundamental understanding of the effects of large "composition-microstructure" space in selected composite systems on their properties at finite temperatures. The specific objectives of the proposed research program are:

1. Elucidate the mechanism and kinetics of multi-phase reactions during high-temperature processing to yield novel metal/MAX phase composites with controlled composition and microstructure and a potentially unprecedented combination of lightweight, strength, ductility, and damping, which is critical to develop energy efficient technologies, *e.g.* aerospace and transportation, powder generation, and energy conversion;
2. Develop tools for controlling the structures, *e.g.* grain size, interpenetrating phase sizes and contents, and interfacial structures, through experimental studies of the effects of processing condition on microstructure evolution.

3. Generate a fundamental understanding of the effects that the large "composition-microstructure" space of novel metal/MAX phase composites has on their thermodynamically stability and character and their thermo-mechanical properties at finite temperatures.

It will be demonstrated that SPS is a viable technique to fabricate highly reactive SMA/MAX phase composites with active (shape memory) constituents. The shape memory behavior will be characterized by conducting isobaric heating-cooling experiments under compressive stresses. The damping behavior under uniaxial compressive cyclic loadings at room temperature will be studied. The introduction of residual stresses by thermo-mechanical cycling and their effect on damping behavior of the composites will be investigated. The thermal diffusivity and specific heat of the SMA/MAX phase composites in a temperature range of 300–1224 K will be measured; the thermal conductivity will be thus calculated. The measurement results will be validated by a survey of data for the thermal diffusivity, specific heat, and thermal conductivity of monolithic NiTi and Ti_3SiC_2. The thermal conductivity will be predicted using finite element (FE) modeling.

As discussed in Chapter I, poor wettability and severe reactions are the most challenging issues of conventional infiltration methods. To solve these issues, a current-activated, pressure-assisted infiltration (CAPAI) method will be developed. The new method will allow the fabrication of highly reactive metal/MAX phase composites with preserved constituents. A combination of the CAPAI method and MAX phase foams with customizable pore structures will be used to enable manipulating structures of

metal/MAX phase composites. The author will characterize the microstructures and micro-tomography of the resulting composites, develop the reaction mechanisms during processing, and tailor the damping capability and ultimate compressive strength of the composites by controlling the microstructure. The author will also discuss the possibility of adapting this method in designing complex hierarchical structures to mimic natural composites.

CHAPTER III

EXPERIMENTAL METHODOLOGY

The aim of this chapter is to present details on the fabrication of the materials, density measurement, microstructural and compositional analysis, and mechanical tests throughout the study.

3.1. Shape Memory Alloy/MAX Phase Composites

3.1.1. Sample Preparation

Ti_2AlC and Ti_3SiC_2 powders (MAXthal312, Sandvik, Sweden) with particle size in 45–90 μm range and NiTi prealloyed powder (Special Metals, New Hartford, NY; gas atomized from the alloy ingot with the nominal composition of $Ni_{50}Ti_{50}$) with particle size in 88–105 μm range were used.

NiTi/Ti_2AlC and NiTi/Ti_3SiC_2 powder mixtures, each with a 50/50 volume ratio (that corresponds to 61 wt% and 59 wt% of NiTi, respectively, in NiTi/Ti_2AlC and NiTi/Ti_3SiC_2 powder mixtures), were mixed for 1 hour by ball milling. No balls were used during the milling to avoid contamination, and the rotation speed was 300 rmp. The powder mixtures were poured into a graphite die (20 mm in diameter) and processed in SPS (25-10, GT Advanced Technologies, CA) in 1233–1373 K under 100–300 MPa uniaxial pressure for 3–30 minutes. The processing conditions were selected for two reasons: (i) temperatures lower than 1233 K and soaking time shorter than 3 minutes resulted in low densities and were not preferable; (ii) temperatures higher than 1373 K

and soaking time longer than 30 minutes resulted in total reactions and were not selected. Fully-dense Ti_2AlC samples were normally obtained at higher temperatures using SPS—1523 K under 20 MPa for 5 min [71] or 1473 K under 30 MPa for 8 min [72]. However, NiTi melts at such high temperatures, leading to catastrophic reactions [59]. The chamber was evacuated and held at 10^{-4} Pa for 10 minutes before heating. The heating rate was 200 K/min, and the whole sintering process was conducted under a flowing, ultra-high-purity argon atmosphere. A high dc current was applied, increasing from 0 to 1450–1620 A in 4 min and then stabilizing at 1120–1330 A for soaking. The pulse cycle was 10 ms on and 10 ms off. Graphite foils were applied between the powder mixtures and the graphite die. Since the highest pressure for graphite die is 100 MPa, silicon carbide (SiC) die (20 mm in diameter) was used for higher sintering pressures (*i.e.* 200 MPa and 300 MPa). The as-fabricated sample is approximately 19.6 mm in diameter and 6 mm in thickness.

The temperature was measured in a drilled hole of the bottom graphite punch, which was immediately below the surface that was in contact with the sample. The temperature was calibrated by measuring the temperature at which bulk, high-purity copper melts (results not shown here). The melting point of copper is compared to the temperature at which the position of the upper piston suddenly changes from thermal expansion to shrinkage as a result of melting, and the latter is 13 K below the former. The actual temperature is thus calibrated as 13 K above the thermocouple reading.

3.1.2. Density Measurement

The density was determined by alcohol immersion method based on Archimedes' principle, as specified in ASTM C20-00 [73]. Theoretical density values of 4.11 g/cm^3 [74], 4.52 g/cm^3 [74], and 6.45 g/cm^3 [75] for Ti_2AlC, Ti_3SiC_2, and NiTi, respectively, were used to calculate the density of the composites according to the rule of mixture (ROM). It was assumed that the effect of the eventual reaction phases on density was negligible. The relative density is the measured density value divided by the ROM values (*i.e.* 5.28 g/cm^3 for the NiTi/Ti_2AlC and 5.48 g/cm^3 for the NiTi/Ti_3SiC_2). Three samples per case were used to determine the average value and standard deviation.

3.1.3. Microstructural and Compositional Analysis

The microstructure, composition, and distribution of phases in the interfacial reaction layers were characterized using a combination of a FE-SEM (JSM-7500F, JEOL, Tokyo, Japan) equipped with Energy Dispersive Spectroscopy (EDS), and another FE-SEM (Zeiss Ultra Plus, Carl Zeiss, Oberkochen, Germany) equipped with an EDS and Electron Backscatter Diffraction (EBSD). Both spot and line scans of EDS were utilized for quantitative analysis of interface chemistry. The accelerating voltage and emission current were 15 kV and 20 mA, respectively. The durations of spot and line scans of EDS were 60 seconds and 15 minutes per spectrum, respectively. Interface thickness (*i.e.* the total thickness of the interfacial reaction layers) was measured and averaged from SEM images at two randomly-selected locations on each sample (five values per image). The EBSD scans were run with an accelerating voltage of 20 kV and

an aperture size of 60 or 120 μm. Large-area scans have a step size of 0.3 μm, while the small-area scans in the interfacial area have a step size of 0.03 μm.

The phase composition of starting powders and composites was determined using an X-ray diffractometer (XRD, D8 Discover, Bruker, WI, USA) with Cu *Kα* radiation (wavelength = 1.542 Å) at 40 kV and 30 mA. The two theta range was 20–80 º with a step size of 0.04 º and a step time of 1.5 s. The results were analyzed utilizing both Joint Committee on Powder Diffraction Standards (JCPDS) and Inorganic Crystal Structure Database (ICSD).

3.1.4. Calorimetry

Differential scanning calorimetry (DSC, Model Q20, TA Instruments, DE) was carried out on 20–80 mg specimens from the composites or the NiTi powder in a flowing nitrogen atmosphere. The heating and cooling cycles are in 213–423 K temperature range with heating and cooling rates of 10 K/min. Each run continuously tracked 3–10 cycles. Transformation temperatures were determined from the peaks observed in the second cycle using the slope line extension method [76]. The enthalpy of phase transformation was calculated from the area under the transformation peaks. Weight percent of transformable NiTi was calculated as follows:

$$W_{trans.} = \frac{(\Delta H^{m\to a} + \Delta H^{a\to m})}{(\Delta H_0^{m\to a} + \Delta H_0^{a\to m})} \times 100\% \quad (1)$$

where $\Delta H^{m\to a}$ and $\Delta H^{a\to m}$, respectively, are enthalpy values of "martensite → austenite" and "austenite → martensite" phase transformations of the composites. $\Delta H_0^{m\to a}$ and $\Delta H_0^{a\to m}$ are the corresponding values of the NiTi powder.

3.1.5. Sample Designation

Table 2 lists starting powder, sintering temperature, soaking time, relative density, interface thickness, percent of transformable NiTi, and phase transformation temperatures of all composites. Each sample is labeled as X-Y-Z where X is A for NiTi/Ti_2AlC or B for NiTi/Ti_3SiC_2, Y is the sintering temperature in K, and Z is the soaking time in minutes. For example, NiTi/Ti_2AlC composites processed at 1233 K for 8 minutes are labeled as A-1233-8.

Table 2. Starting powder, sintering temperature, soaking time, relative density, interface thickness, percent of transformable NiTi ($W_{trans.}$), and phase transformation temperature (M_s) of all composites.

Sample		Materials				Processing conditions			Properties			
		MAX phase	Particle size (μm)	SMA	Particle size (μm)	Sintering temperature (K)		Soaking time (min)	Relative density (%)	Interface thickness (μm)	$W_{trans.}$ (wt. %)*	M_s (K)
						Thermocouple reading	Calibrated					
A	A-1233-8	Ti_2AlC	45–90	NiTi	88–105	1233	1246	8	86.1±2.1	2.9±0.6	46.1	343±1.5
	A-1233-20							20	87.7±2.5	5.3±1.7	34.5	339±1.3
	A-1233-30							30	90.5±0.8	6.9±1.3	24.5	343±1.1
	A-1253-10					1253	1266	10	89.4±0.1	6.1±2.8	32.6	343±1.7
	A-1273-3					1273	1286	3	89.5±0.4	6.9±1.6	41.2	343±1.4
	A-1373-5					1373	1386	5	97.3±0.5	N/A	5.6	343±1.6
B	B-1233-8	Ti_3SiC_2				1233	1246	8	83.3±1.1	< 1	60.4	344±1.9
	B-1233-8†								89.1±0.7		60.4	346±1.1
	B-1233-8‡								96.3±1.3		60.3	346±1.5
	B-1233-20							20	83.5±0.8		60.1	347±0.9
	B-1233-30							30	87.8±0.3		53.3	347±0.8
	B-1253-10					1253	1266	10	83.6±1.1		58.3	347±2.0
	B-1273-3					1273	1286	3	82.8±0.9		50.1	347±2.1

* Defined in equation (1).
† Processed under a 200 MPa sintering pressure.
‡ Processed under a 300 MPa sintering pressure.

3.2. Al Alloy/MAX Phase Composites

3.2.1. Sample Preparation

Ti_2AlC powders (MAXthal 211, Sandvik Heating Technology AB, Sörkvarnsvägen, Sweden) with particle size in the 45–90 μm range, and NaCl powders (Sigma-Aldrich, St. Louis, MO, USA) with a variety of particle sizes, *i.e.* 45–90 μm, 180–250 μm, and 355–500 μm, were used to process Ti_2AlC foams using procedures described elsewhere [77]. The preparation of the foams involves three steps: (i) cold pressing a NaCl-Ti_2AlC powder mixture with 20/80 or 40/60 volume ratio; (ii) dissolving the NaCl in distilled water, and (iii) pressureless sintering of the Ti_2AlC under flowing argon at 1400 ºC for 4 hours. Pore size of the foams was determined by measuring the size of 50 pores in SEM images using the intercept method, as specified in ASTM E112-13 [78]. Four SEM images from randomly selected locations on each sample were used. Aluminum alloy 6061 (AA6061) discs (McMaster-Carr, GA) with a diameter of 20 mm and a thickness of 4 mm were used for the infiltration process.

A disc (20 mm in diameter and 4 mm in thickness) of Ti_2AlC foam was "sandwiched" between two AA6061 discs and placed in a graphite die (Figure 3), followed by infiltration at 750 ºC under 5 MPa uniaxial pressure for 1 minute. The "sandwich" set-up enables more uniform infiltration of molten metal. The infiltration was carried out in a spark plasma sintering system (SPS 25-10, GT Advanced Technologies, CA). A direct current was applied from 0 to 1250 A in 4 min and stabilized at 860 A for 1 min at 750 ºC; the pulse cycle was 10 ms on and 10 ms off. The

chamber was evacuated and held at 10^{-6} torr for 10 minutes before heating. The heating rate was 200 ^{o}C/minute. It takes less than 10 minutes for a complete infiltration process including heating/melting, soaking, and cooling/solidification. Graphite foils were applied between samples and graphite die before infiltration. The temperature was calibrated and measured using procedures described elsewhere [48].

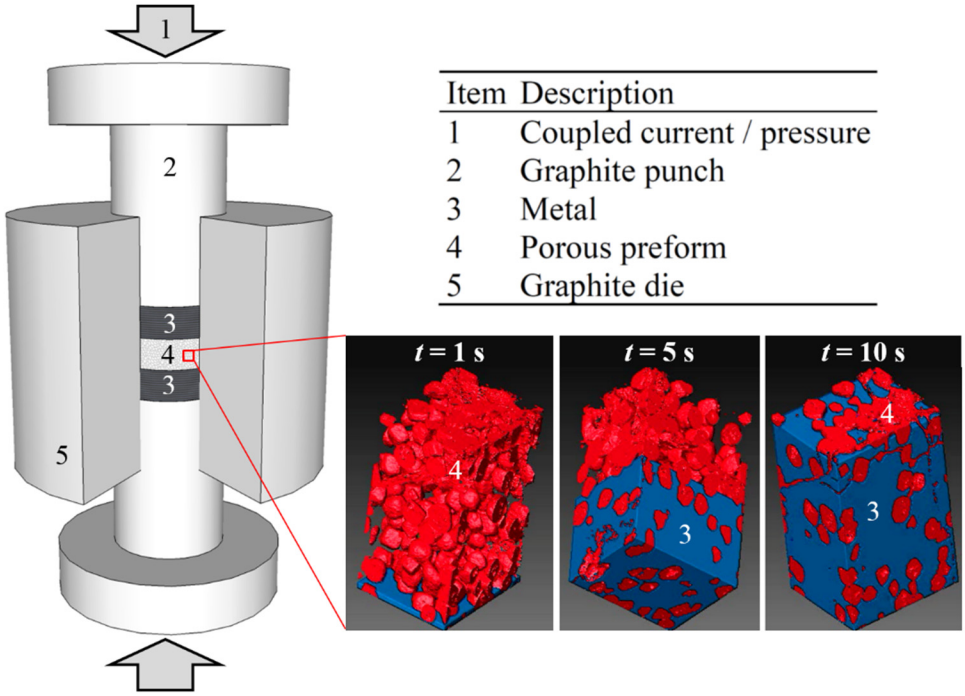

Figure 3. Schematic of a rapid infiltration approach showing the coupled current/pressure (item 1), the graphite die set (items 2 and 5), and the 'sandwich'-like set-up of the metal (item 3) and porous preform (item 4).

3.2.2. Density Measurement

The density and porosity (both open and closed) were determined by alcohol immersion method based on Archimedes' principle, as specified in ASTM C20-00[73]. The theoretical density values of 4.11 (g/cm^3)[74] and 2.70 (g/cm^3)[73] for Ti_2AlC and

aluminum, respectively, were used to calculate the theoretical density of composites using the rule of mixture. It was assumed that the effect of eventual reaction on the theoretical density is negligible. The relative density equals the measured value divided by the rule-of-mixture value, *i.e.* 3.55 g/cm^3.

3.2.3. Microstructural and Compositional Analysis

The phase composition of the starting powders and the as-infiltrated composites was determined using an X-ray diffractometer, XRD (*D8* Discover, Bruker, WI) with Cu *Kα* radiation (wavelength = 1.542 Å) at 40 kV and 30 mA. The two theta range was from 8 º to 80 º with a step size of 0.04 º and a step time of 1.5 s. The XRD results were analyzed utilizing the Inorganic Crystal Structure Database (ICSD). The microstructure, phase composition and distribution were characterized using a Field Emission Scanning Electron Microscopy, FE-SEM (JSM-7500F, JEOL, Tokyo, Japan), equipped with Energy Dispersive Spectroscopy (EDS). Also used was another FE-SEM (Zeiss Ultra Plus, Carl Zeiss, Oberkochen, Germany) equipped with an Oxford Instrument AZtec EDS and a Nordlys-S Electron Backscatter Diffraction (EBSD) system. The accelerating voltage and emission current were 15 kV and 20 mA, respectively. The duration of spot scan of EDS was 60 seconds per spectrum. The EBSD scans were run with an accelerating voltage of 12 kV, an aperture size of 60 μm or 120 μm depending on the specimen, and a step size of 0.3 μm. The 3D microstructure showing the phase distribution was obtained using an Xradia MicroXCT-400 Micro-Computed Tomography (Zeiss, Germany). The composition of the AA6061 and the Al alloy in the

composite was measured using a Cameca SX-100 electron microprobe with a wavelength dispersive spectrometry (WDS) system.

3.2.4. Uniaxial Compression Tests

The compressive strength was measured by using a universal testing machine (MTS810, MTS, MN) with a strain rate of 1.4×10^{-4} s^{-1}. The compressive stress-strain responses of the specimens under cyclic loading was measured using a MTS insight electromechanical test frame with a strain rate of 7×10^{-4} s^{-1}. The strain was measured using an MTS extensometer with a gage length of 3 mm, and the extensometer was attached directly on the specimens. All specimens for compressive testing were cut by electrical discharge machining to dimensions of 3.5 mm × 3.5 mm × 7 mm.

CHAPTER IV

FABRICATION AND CHARACTERIZATION OF TERNARY CARBIDE FOAMS WITH CONTROLLED POROSITY AND PORE SIZE *

In this chapter, a simple and inexpensive method is developed to fabricate ternary carbide foams, *i.e.* Ti_2AlC, with controlled porosity and pore size. The Ti_2AlC foams were systematically characterized to determine their composition, microstructure, and mechanical properties. The Ti_2AlC foams are used as preforms for molten metal infiltration to fabricate metal/ternary carbide composites described in the next chapter.

4.1. Introduction

For infiltration processes, ceramic preforms have to be made before the metal is infiltrated. The preform structures are normally packed particles or fibers [79] and can be solid foams [80]. Desired preforms not only maintain their pore structures during handling and placement prior to the infiltration process, but also survive the stresses during the infiltration process. To that end, MAX phases are selected to prepare such preforms, because MAX phases are kinking-nonlinear elastic solids which can dissipate significant amount of energy during cyclic loading. The energy dissipation is due to the formation and annihilation of fully reversible incipient kink bands [19].

---

* Reprinted from Acta Materialia, Vol. 60, Liangfa Hu, Rogelio Benitez, Sandip Basu, Ibrahim Karaman, Miladin Radovic, Processing and characterization of porous Ti_2AlC with controlled porosity and pore size, 6266–6277, Copyright (2012), with permission from Elsevier.

Ti_2AlC is one of the most studied MAX phases, but few studies focused on Ti_2AlC foams [81-84]. MAX phase foams, including Ti_2AlC foams, deserve further studies, because control of the porosity and pore size can be used to tailor mechanical properties. Such tailoring of properties has been reported by Fraczkiewicz *et al.* [81] for Ti_3SiC_2, Zhou *et al.* [82] for Ti_2AlC, and Sun *et al.* [83] for Ti_3SiC_2. More recently, it was shown that Mg/MAX phase composites with exceptional mechanical properties can be fabricated by molten metal (Mg) infiltration of MAX phase foams [23]. The Mg/Ti_2AlC composites exhibited higher strength in both tension (350 ± 40 MPa) and compression (700 ± 10 MPa) than other Mg composites, as well as exceptional damping capabilities [24]. Apart from structural applications, MAX phase foams are also potential substrates for catalytic coatings in gas exhaust catalyst devices [85].

MAX phase foams were prepared in a few studies using one of two methods: (1) incomplete sintering of MAX phase powders or elemental powders [81-84], and (2) the replica method based on highly dispersed aqueous suspension using polyurethane sponges as a pore former [85]. Although the first method is simple and straightforward, it does not allow control of porosity and pore size. The second method allows control of porosity and pore size, but it is complicated, time consuming, and not feasible for processing samples with a low porosity.

A simple and inexpensive method is reported in the present work to fabricate Ti_2AlC foams with controlled porosity and pore size using NaCl powders as a pore former. The first use of NaCl powders as the pore former was reported in 1960s by Polonsky and co-workers [86]. Since then, this method has been utilized to fabricate

aluminum foams [87-89], shape memory alloy foams [90, 91], titanium foams [92], and other metal foams [93, 94]. It has several advantages to use NaCl powders as the pore former. First, NaCl powders can be easily and completely removed by dissolving in water after cold pressing but before sintering. This eliminates reactions between the pore former and the MAX phase, which has been a challenge to conventional replica methods. Before this work, pore formers can react with the MAX phase during sintering to form new phases, *e.g.* binary carbides [95]. The new phases are detrimental, because they degrade constituents of the composites. Second, NaCl powders are inexpensive and commercially available in a broad range of particle sizes, which enables the control of pore size.

In this chapter, the composition, microstructure, and mechanical properties (*i.e.* elastic moduli and compressive strength) of Ti_2AlC foams are systematically characterized. The effect of porosity and pore size on the mechanical properties of Ti_2AlC are discussed. The discussion involves the comparison of different samples prepared both with and without using NaCl powders as the pore former, as well as samples prepared using spark plasma sintering (SPS). The results show that the developed methodology is viable to prepare MAX phase foams with graded porosity and consequently functionally graded properties.

4.2. Experimental Details

Ti_2AlC powders (MAXthal312, Sandvik, Sweden) with particle sizes of 45–90 μm or <20 μm were used. Figure 4 shows a field emission scanning electron microscopy

(FE-SEM) image of Ti_2AlC powders with particle sizes of 45–90 μm, while the inset illustrates the nanolaminated nature of the ternary carbide. NaCl powders with particle sizes of 45–90 μm, 180–250 μm and 355–500 μm were used as the pore former (Figure 4). The Ti_2AlC powders and 0, 20, 40, 60 and 80 vol.% NaCl powders were mixed for 1 h by ball milling and cold pressed in a cylindrical steel die (12.7 mm in diameter) using a pressure of 800 MPa. Green bodies were soaked in water overnight to dissolve the NaCl pore former and rinsed in water several times to remove all remaining NaCl. The green bodies were then sintered in flowing argon at 1400 °C for 4 h in a tube furnace. A Ti_2AlC sample with graded porosity was also prepared using this method, but the steel die was filled in this case with four different layers containing 0, 20, 40 and 60 vol.% NaCl pore former. For comparison, some Ti_2AlC foams were prepared by incomplete sintering using SPS (25-10, Thermal Technologies, CA) of Ti_2AlC powders in the 1100–1200 °C temperature range under 50–100 MPa for 20 min.

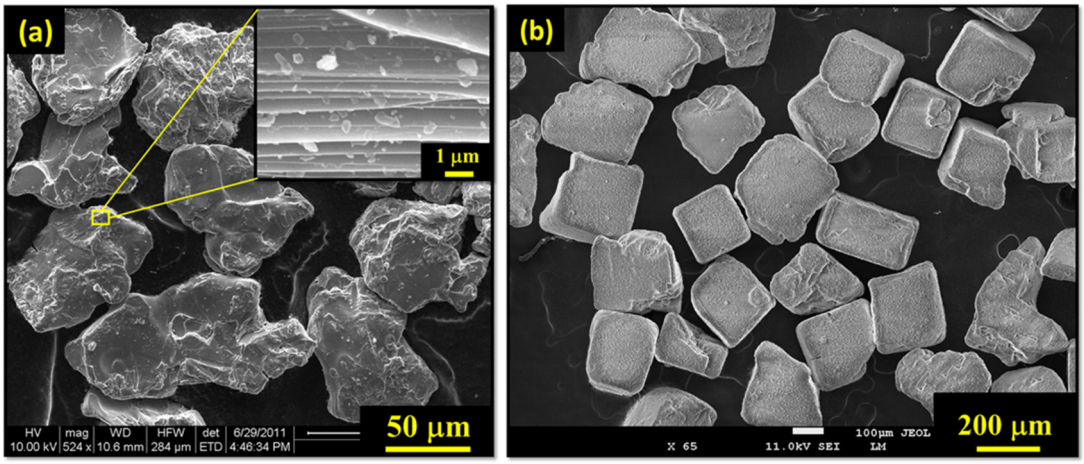

Figure 4. FE-SEM images of (a) Ti_2AlC powders with particle sizes of 45–90 μm, and (b) NaCl powders with particle sizes of 180–250 μm. The inset illustrates the nanolaminated structure of the ternary carbide.

The microstructure was characterized using a FE-SEM (Quanta 600 FEG, FEI, Oregon, USA or JSM-7500F, JEOL, Tokyo, Japan). Pore size distribution was determined by measuring the size of 30 pores using the intercept method, *i.e.* ASTM E112-10. The measurement is based on SEM images in the 4 randomly selected locations on each sample, which enables calculation of the fraction of the pores with the size in a certain range. The porosity was measured by alcohol immersion method based on Archimedes' principle, as specified in ASTM C20-00 using the following equations:

$$\rho = \frac{m_{dry} \times \rho_{ethanol}}{m_{wet} - m_{suspended} + m_{wire}} \tag{2}$$

$$P_{overall} = (1 - \frac{\rho}{\rho_{theoretical}}) \times 100 \tag{3}$$

$$P_{open} = \frac{m_{wet} - m_{dry}}{m_{wet} - m_{suspended} + m_{wire}} \times 100 \tag{4}$$

where m_{dry} is dry mass (g) of the sample, $m_{suspended}$ is mass of the sample suspended in 200% proof ethanol, m_{wet} is mass of the sample after soaking in the ethanol, m_{wire} is mass of the suspending system, $\rho_{ethanol}$ is density (g/cm^3) of the ethanol, $P_{overall}$ is overall porosity (vol.%), and P_{open} is open porosity (vol.%). The theoretical density of 4.11 g/cm^3 [74] for fully dense Ti_2AlC was used as a reference to calculate the porosity according to equation (3).

The phase composition of starting Ti_2AlC powder and sintered Ti_2AlC sample was determined using an X-ray diffractometer, XRD (D8 Discover, Bruker, Madison, USA) with Cu K_α radiation (wavelength = 1.542 Å) at 40 kV and 30 mA. The two theta

values vary from 8 º to 80 º with a step size of 0.04 º and a step time of 1.5 s. The results were analyzed utilizing the Inorganic Crystal Structure Database (ICSD).

Elastic moduli of the Ti_2AlC foams were measured by resonant ultrasound spectroscopy (RUS, Magnaflux Quasar Systems, NM), which is based on measuring the spectrum of the resonant mechanical vibrations for a specimen with known geometry, dimensions, and mass [96-98]. All samples for RUS were machined to sharp edges and a parallelism with less than 1 % error of thickness. Ti_2AlC foams (12.7 mm or 25.4 mm in diameter and 3.5 mm in thickness) were placed on 3 piezoelectric transducers. One of these transducers, *i.e.* transmitting transducer, generates an elastic wave at constant amplitude but varying frequency. The other 2 transducers detect responses from the specimen, generating resonant spectrum. The elastic, bulk, and shear moduli were determined by matching measured resonant peaks to calculated ones using a software, *i.e.* multidimensional algorithm Quasar RuSpec (Magnaflux Quasar Systems, NM). The software iteratively minimizes deviations between the measured and calculated resonant peaks by changing the initial elastic constants, until converging values are achieved.

The compressive strength of the samples with dimensions of 5 × 5 × 8 mm was measured using a universal testing machine (MTS810, MTS, MN) under displacement control mode with a strain rate of 5×10^{-3} s^{-1}. Teflon tape was applied between sample and fixture to reduce frictions. All samples for compressive testing were cut by diamond saw and additionally ground to achieve parallelism with less than 1 % error of thickness.

4.3. Results and Discussion

4.3.1. Phase Analysis

Figure 5 shows typical XRD spectra of sintered Ti_2AlC foams in comparison to starting Ti_2AlC powders. Two major phases in both starting Ti_2AlC powders and sintered Ti_2AlC foams are Ti_2AlC and Ti_3AlC_2, whereas Al_2O_3 and TiC were present only in a small amount as impurities. No presence of NaCl was observed in sintered porous sample, suggesting that all NaCl pore former was completely removed before sintering. This was also confirmed by EDS (results not shown here).

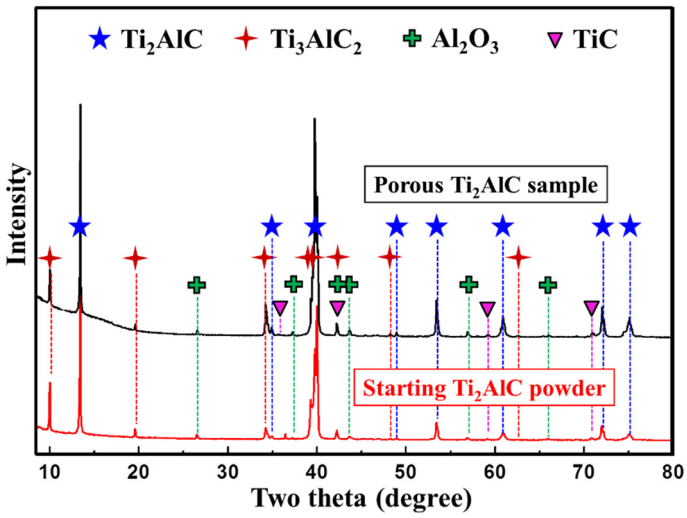

Figure 5. Typical XRD spectra of starting Ti_2AlC powder and sintered Ti_2AlC foams prepared with 40 vol.% of NaCl powders. The particle sizes of the NaCl powders are 355–500 μm. The identification of phases was according to the ICSD collection code 165460 for Ti_2AlC, 153266 for Ti_3AlC_2, 10425 for Al_2O_3 and 44494 for TiC.

To better understand what happened during the sintering process, quantitative information is needed to compare the phase contents of sintered Ti_2AlC foams to those

of starting Ti_2AlC powders. To that end, the molar percent of phases was determined by the relative intensity of the highest XRD peaks of each phase (Table 1). Note that the amounts of Ti_2AlC and TiC decrease, whereas the amount of Ti_3AlC_2 increases after the sintering process. It is known that Ti_2AlC reacts with TiC to form Ti_3AlC_2, leading to more Ti_3AlC_2 in the sintered Ti_2AlC foams than starting Ti_2AlC powders. The decrease in the amount of TiC is negligible when compared to the decrease of Ti_2AlC. The change is caused by decomposition of Ti_2AlC according to the following reaction: [99]

$$2Ti_2AlC(s) \rightarrow Ti_3AlC_2(s) + TiAl_{1-x} + xAl(g \text{ or } l) \quad (5)$$

where $x \leq 1$. The composition of $TiAl_{1-x}$ depends on how much Al is lost to the surrounding. The extreme situation is that only pure Ti remains when Al is totally lost [99]. This reaction explains not only the fact that the decrease of Ti_2AlC is approximately twice the increase of Ti_3AlC_2, but also that the intensity ratio of Ti_2AlC/Ti_3AlC_2 decreased from 4.0 to 3.6 — a 10% drop for the intensity ratio. The decomposition (equation (5)), could be even more severe when compared to the fully dense samples, because the high surface area in the foams allows faster loss of the Al.

Table 3. Molar percent of phases in the starting Ti_2AlC powders and sintered Ti_2AlC foams as determined by the relative intensity of the highest XRD peaks of each phase.

Material	Molar percent of phases, %				Phase ratio
	Ti_2AlC	Ti_3AlC_2	Al_2O_3	TiC	Ti_2AlC / Ti_3AlC_2
Starting Ti_2AlC powders	77.0	19.2	1.3	2.5	4.0
Sintered Ti_2AlC foams	74.5	20.7	2.5	2.3	3.6

Another observation is a total weight loss of ~1% after sintering. This may be attributed to the loss of Al, even possibly some Ti, because both Al and Ti vaporize at

high temperatures and go to the surroundings. Both Al and Ti may react with oxygen to form oxides. However, the Gibbs free energy of $4Al + 3O_2 \rightarrow 2Al_2O_3$ is more negative than that of $Ti + O_2 \rightarrow TiO_2$, [100, 101] indicating that Al reacts with oxygen more easily than Ti. This most likely explains why no TiO_2 but Al_2O_3 peaks were detected by XRD in the sintered Ti_2AlC foams. This also follows that the increase of Al_2O_3 is not surprising, because some of the Al released from the reaction (5) can react with the residual oxygen in the sintering atmosphere to form Al_2O_3.

4.3.2. Characterization of Porosity

The porosity was quantitatively characterized by determining values of overall and open porosities of Ti_2AlC foams, as described in Experimental Details. Figure 6 shows the variations of overall and open porosities with volume percent of NaCl pore former. The variations are shown for different sizes of the NaCl particles, i.e (a) 45–90 μm, (b) 180–250 μm, and (c) 355–500 μm. The lowest overall porosity of around 9–10 vol.% was measured in the sample sintered without using any NaCl as the pore former. This porosity is due to the presence of inter-granular pores (closed pores) and channels (open pores) that remained in the structure as a result of incomplete sintering.

Both overall and open porosities increase linearly with increasing volume percent of NaCl pore former. The trend is independent of particle size of NaCl pore former. This is obvious in Figure 6(d), where overall porosity of the Ti_2AlC foams with different amount of pore former was plotted as a function of volume percent of NaCl pore former. This finding cannot be overemphasized, since it suggests that the size of pore former in

general does not affect shrinkage during the sintering process. The overall porosity is not always lower than volume percent of NaCl pore former added before sintering. Figure 6 clearly shows that the overall porosity is larger than the volume percent of pore former for Ti_2AlC foams processed with less than 40 vol.% of NaCl pore former. In contrast, for Ti_2AlC foams processed with more than 40 vol.% of NaCl pore former, the overall porosity is lower than the volume percent of pore former. This observation suggests that porosity in sintered samples not only comes from pore former, but also result from incomplete sintering of Ti_2AlC powder.

Figure 6 shows that the difference between overall and open porosities becomes smaller as the volume percent of NaCl increases. For example, Figure 6(c) shows that the open/overall porosity ratio increased from 0.61, 0.95, 0.96 to 0.99 as the volume fraction of NaCl pore former increased from 0, 20, 40 to 60 vol.% (for the samples processed using NaCl pore former with particle sizes of 355–500 μm). It indicates that the number of the connected pores increases with increasing volume percent of NaCl pore former. More individual NaCl particles means a higher probability for any two neighboring NaCl particles to connect to each other, leading to a higher connectivity.

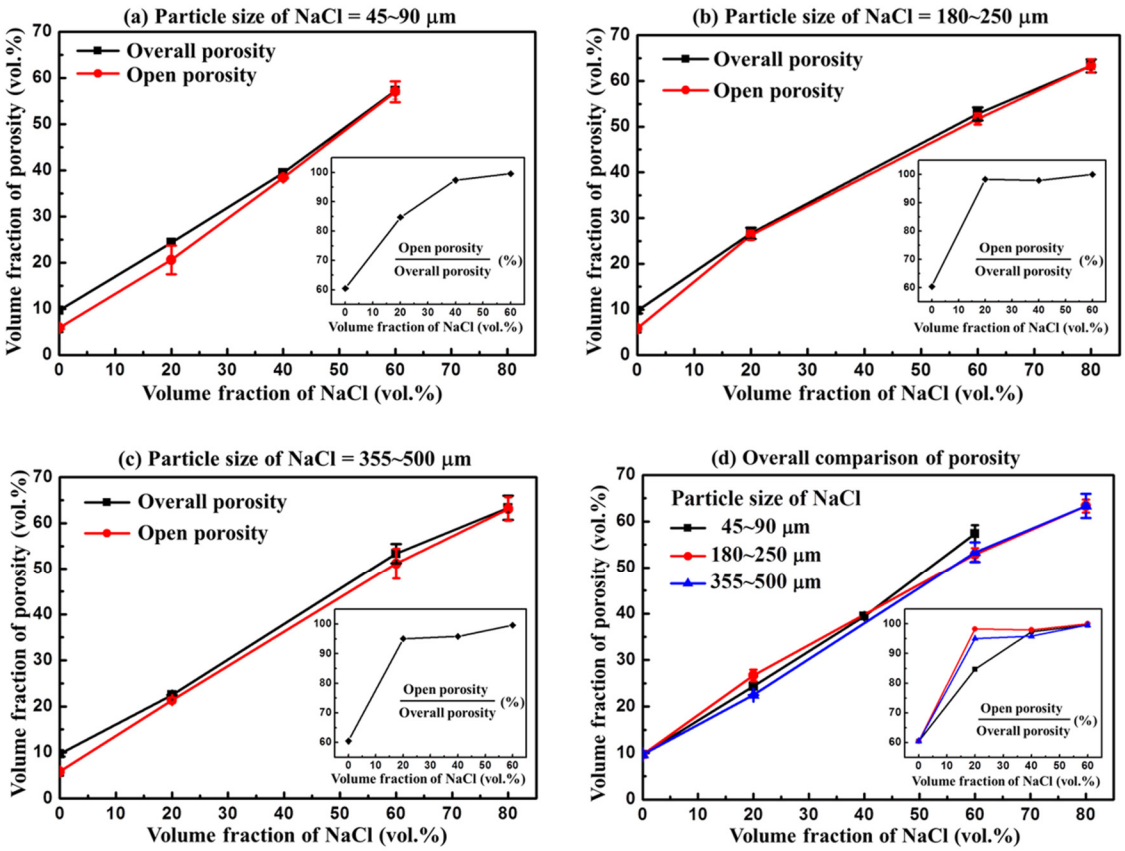

Figure 6. Variations of overall and open porosities with volume percent of NaCl pore former. Particle sizes of NaCl pore former: (a) 45–90 μm, (b) 180–250 μm, and (c) 355–500 μm. (d) a comparison of overall porosity in all samples. Insets show the open/overall porosity ratio as a function of volume percent of NaCl pore former.

Figure 6 also suggests that when the size of the NaCl particles is significantly larger that the Ti_2AlC particles, almost all pores are interconnected when porosity is above 20%. However, when the size of the NaCl particles is comparable to that of the Ti_2AlC particles, open porosity increases slowly with the amount of pore former. This suggests that even higher open porosities could be achieved using finer Ti_2AlC powders. Indeed, Figure 7 shows the highest overall porosity, *i.e.* 71 vol.%, in the sample with fine Ti_2AlC powders (<20 μm particle sizes). This porosity value is 13% higher than that

of the sample with coarse Ti_2AlC powders (45–90 μm particle sizes). It indicates that the particle size of Ti_2AlC powders, in addition to volume percent and particle size of NaCl powders, is another parameter to tailor porosity and pore connectivity in Ti_2AlC foams.

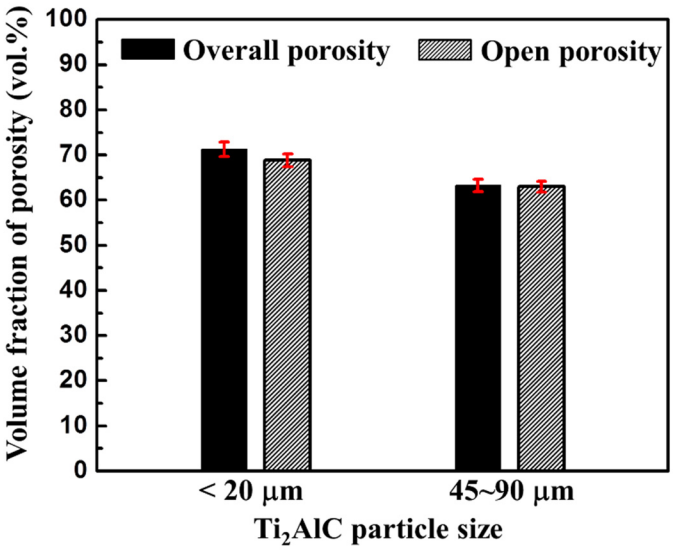

Figure 7. Variation of overall porosity with the particle size of Ti_2AlC powders. Both samples were processed with 80 vol.% NaCl pore former (180–250 μm particle sizes).

4.3.3. Microstructure and Pore Size Distribution

Figure 8 shows SEM images of Ti_2AlC foams with different pore sizes. All three samples in Figure 8(a)–(c) have relatively comparable porosities of 56.0, 50.9 and 50.6 vol.%, although they were prepared with pore former sizes of 45–90 μm, 180–250 μm, and 355–500 μm, respectively. Although pores in Figure 8(a) appear to be more connected than those in both Figure 8(b) and (c), Figure 6 shows that all three samples have comparable open porosities. The fracture surface of Ti_2AlC foams in Figure 8(d)

better illustrates the typical connectivity of Ti_2AlC grains and formation of the sintering necks. The strong network of Ti_2AlC grains is critical to obtain high strength.

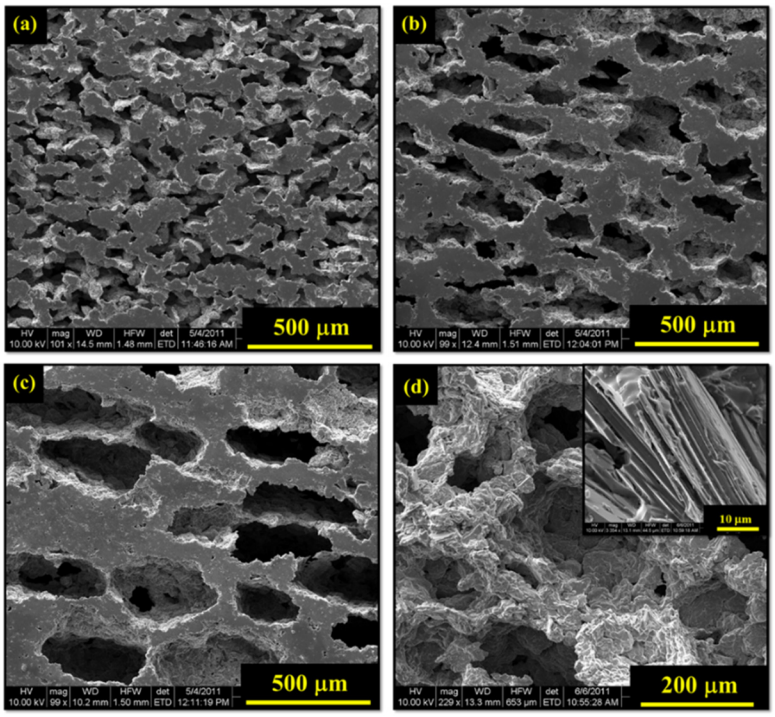

Figure 8. SEM images of Ti_2AlC foams with different pore sizes formed by addition of 60 vol.% NaCl pore former with different particle sizes: (a) 45–90 µm, (b) 180–250 µm, and (c) 355–500 µm. (d) shows typical microstructure of fracture surface (60 vol.% pore former with particle sizes of 180–250 µm). The overall porosity is comparable: (a) 56.0 vol.%, (b) 50.9 vol.%, (c) 50.6 vol.%, and (d) 50.9 vol.%.

Figure 8 also shows that the pore shape becomes more and more elliptical with increasing pore size. The elliptical pores have conjugates in the loading direction of cold pressing, *i.e.* vertical direction in Figure 8, and transverse diameters perpendicular to loading direction. Taking into account that the shape of NaCl particles is cubic (Figure 4(b)) rather than elliptical, the elliptical shape of the pores is most likely consequence of the cold pressing. During the cold pressing, larger NaCl particles deform, crush, and

compact along the loading direction. This is confirmed by microscopic observations on the cross-section of as-pressed samples (not show here).

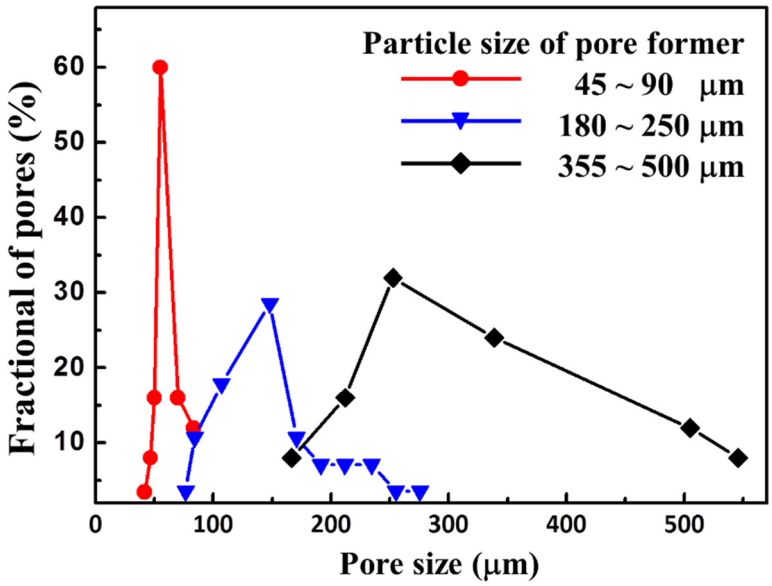

Figure 9. Pore size distribution of Ti_2AlC foams with different pore sizes formed by NaCl powders with different particle sizes: 45–90 μm, 180–250 μm, and 355–500 μm.

Table 4. Pore sizes of Ti_2AlC foams with comparable porosities. Average pore size and standard deviation were determined from the measured values as $\bar{x} = \frac{1}{N}\sum_{i=1}^{N} x_i$ and $s = \sqrt{\frac{1}{N}\sum_{i=1}^{N}(x_i - \bar{x})^2}$ respectively, where N is the total number of values measured from SEM images, x_i is the pore size, and $\bar{x}$ is the average pore size.

Particle size of NaCl (μm)	Volume fraction of NaCl (%)	Porosity (vol.%)	Average pore size (μm)	Standard deviation (μm)
45–90		56	59	11.7
180–250	60	50.9	148	55.5
355–500		50.6	346	133.1

The pore size distributions were quantitatively characterized by measuring the pore sizes in the samples shown in Figure 8, and the results were summarized in Table 4 and Figure 9. Table 4 summaries the average pore sizes and standard deviations for each pore size distribution curve shown in Figure 9. The average pore size increases from 59 μm, 148 μm, to 346 μm with increasing particle size of NaCl pore former. The pore size distribution becomes broader with increasing particle size of NaCl pore former. The increasingly broader particle size range of NaCl pore former (45 μm, 70 μm and 145 μm) is the main reason for the increasing pore size range. Note that the samples processed from coarser NaCl particles have a more elliptical pore shape, and both transverse and conjugate diameters were taken into account for pore size measurements. This also broadened the pore size range. This also explained that the sample processed from 355–500 μm NaCl powders had some measured pore size at 550 μm, which was larger than the maximum size of the pore former particles.

Figure 10 illustrates the microstructure of Ti_2AlC foams processed with different volume percent (0, 20, 40 and 60 vol.%) but fixed particle size (45–90 μm) of NaCl pore former. After dissolving and sintering, Ti_2AlC foams samples without processing cracks were obtained with a maximum porosity of 56.0 vol.%. As illustrated in Figure 10(d), the sample with highest porosity shows interconnected pores, which are homogeneously dispersed in the Ti_2AlC matrix. A sample with lower porosity was processed using no NaCl pore former for comparison (Figure 10(a)), *i.e.* only pressureless sintering of starting Ti_2AlC powders.

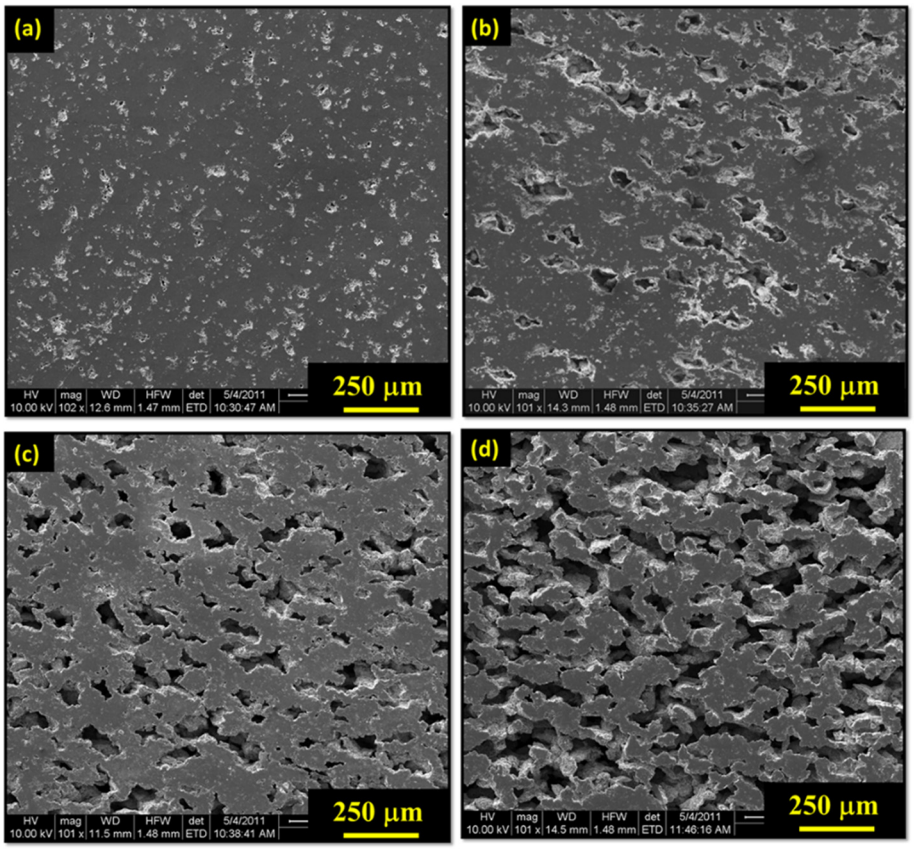

Figure 10. SEM images of Ti_2AlC foams with increasing porosity: (a) 9.3 vol.%, (b) 23.6 vol.%, (c) 39.3 vol.%, and (d) 56.0 vol.%. Sample (b), (c) and (d) were processed from NaCl pore former with the same particle size (45–90 µm).

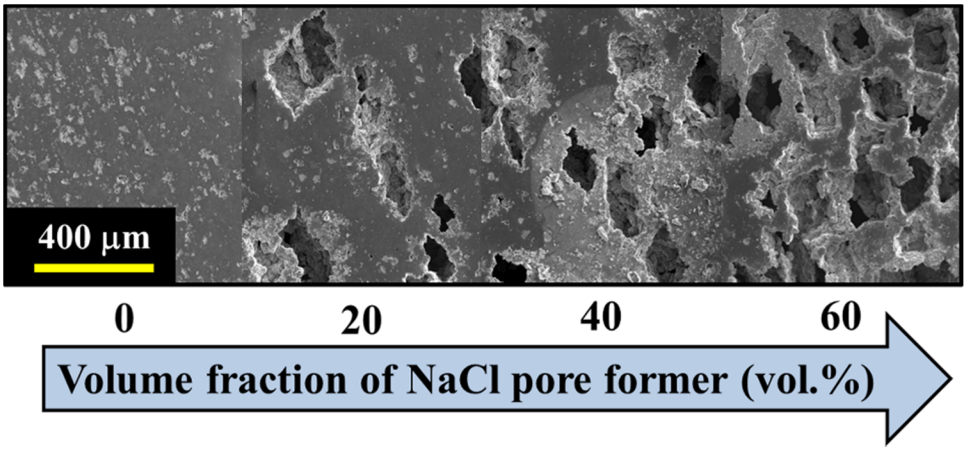

Figure 11. Micrograph of the Ti_2AlC foams with graded porosity. The particle size of the NaCl pore former: 180–250 µm. The overall porosity: 33.2 vol.%.

4.3.4. Ti_2AlC Foams with Graded Porosity

The simple and inexpensive fabrication method described above was also applied to fabricate a sample with graded porosities as shown in Figure 11. This sample was made by cold pressing and sintering of 4 layers with different volume percent of NaCl pore former (*i.e.* 0 vol.%, 20 vol.%, 40 vol.% and 60 vol.%) in one sample. The importance of having a simple method for preparing Ti_2AlC foams with graded porosity cannot be overestimated, because it enables the design of functionally graded properties of the MAX phases and their composites.

4.3.5. Mechanical Properties

The elastic moduli of Ti_2AlC foams are listed in Table 5. Fully dense Ti_2AlC was also prepared and tested for comparison. The highest porosity of all tested samples is approximately 35 vol.%. Samples with higher porosity than 35 vol.% were not tested, because they were too fragile to maintain sharp edges and regular shapes during machining. The sharp edges and regular shapes are crucial for reliable measurement of elastic moduli. The measured values of Young's and shear moduli were plotted as functions of porosity in Figure 12. Relative Young's and shear moduli values were determined by dividing the measured values to those of the fully dense material [102]. Both Young's and shear moduli versus porosity data were fitted using three different empirical models—exponential model, Hasselman model, and composite spheres model (CSM):

Exponential model [103, 104]: $\frac{E}{E_0} = \frac{G}{G_0} = e^{-b \cdot P}$ (6)

Hasselman model [105]: $\frac{E}{E_0} = \frac{G}{G_0} = 1 - \frac{b \cdot P}{1 + (b-1) \cdot P}$ (7)

CSM [106-108]: $\frac{E}{E_0} = \frac{G}{G_0} = \frac{(1-P)^2}{1 + b \cdot P}$ (8)

where E_0 and G_0 are the Young's and shear moduli of fully dense Ti_2AlC. P is the porosity, and b is an empirical constant. E and G are the Young's and shear moduli of porous Ti_2AlC with a porosity of P. The results of the regression analysis of the experimental data in Figure 12 using all three models, as well the coefficient of correlation (R^2) are listed in Table 6. Note that the R^2 values for all three models (exponential model, Hasselman model, and CSM) are high and identical, suggesting that all three models can be used equally well to describe the variations of the elastic moduli with porosity.

Table 5. Particle size of starting Ti_2AlC powder, pore former size and volume percent, sintering method, dimensions of testing samples, density ρ, porosity P, shear modulus G, Young's modulus E, Poisson's ratio v, and bulk modulus B of all tested samples for elastic moduli.

Sample	Ti_2AlC particle size	Pore former size/volume percent	Method	Dimensions (mm)	ρ (g/cm^3)	P (vol.%)	G (GPa)	E (GPa)	v	B (GPa)	Reference
A	~25 μm of grain size	None	HIP	Φ 20.20 × 3.00	4	2.7	118.8	277.6	0.169	139.6	[96]
B	45–90 μm	None	SPS	Φ 19.68 × 5.17	3.76	8.5	95.2	221.9	0.165	110.5	This work
C	45–90 μm	None	SPS	Φ 19.68 × 7.10	3.55	13.6	67.9	158.5	0.167	79.3	
D	45–90 μm	None	SPS	Φ 19.67 × 5.94	3.45	16	66	153.1	0.16	75.1	
E	45–90 μm	None	SPS	Φ 19.63 × 7.51	3.41	17	57.6	134.2	0.165	66.8	
F	<20 μm and 45–90 μm	None	PS	Φ 23.99 × 3.45	3.54	13.8	88.3	206.9	0.172	105.2	
G	45–90 μm	None	PS	Φ 12.55 × 1.81	2.98	27.5	49.1	116.3	0.184	61.4	
H	45–90 μm	180–250 μm, 20 vol.%	PS	15.79 × 15.79 × 7.55	2.69	34.6	40.9	93.8	0.148	44.4	

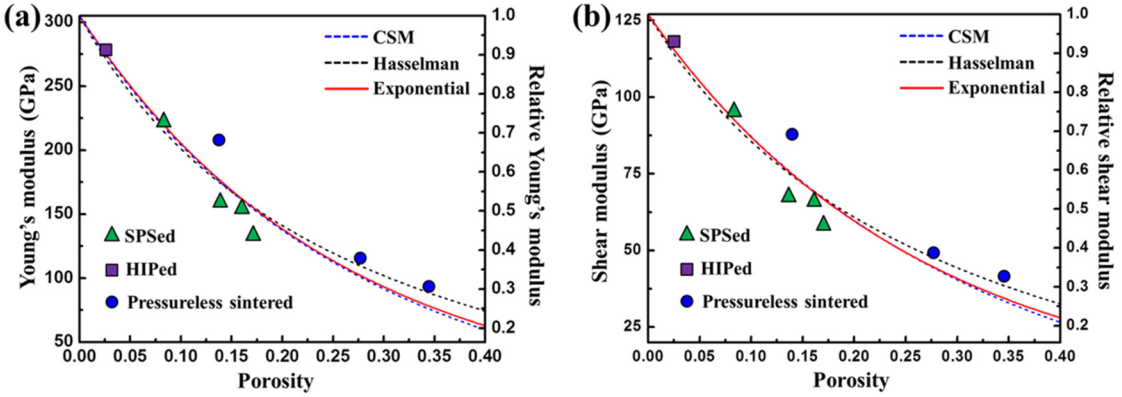

Figure 12. (a)Young's and (b) shear moduli of Ti_2AlC as functions of porosity. Dots are experimental data determined from the SPS samples (triangle, green), HIP samples (square, purple) [96], and PS samples (round, blue). Also included are the predictions from the CSM model (dash, blue line), Hasselman model (dash, black line), and exponential model (solid, red line).

Table 6. Empirical constant (b) and coefficient of correlation (R^2) from the regression analysis of the experimental data and the model values.

Model name	Young's modulus		Shear modulus	
	b	R^2	b	R^2
CSM	2.10	0.92	1.80	0.92
Hasselman	4.65	0.92	4.35	0.92
Exponential	3.95	0.92	3.78	0.92

Another observation is that increasing porosity within the range of 3–35 vol.% causes a sharp drop in elastic moduli. The trend is independent of the different pore structures, which resulted from different processing methods, *i.e.* HIP [96], SPS, and pressureless sintering (PS). The pore structures in SPS samples are different from those in PS samples. Even for samples processed by the same method (PS), the pore structures in PS samples processed with NaCl pore former are different from those in PS samples processed without NaCl pore former. In spite of these differences, the experiment data from different cases did not significantly scatter, but agreed well with the models.

Therefore, the decrease of elastic moduli predominately stems from the increasing porosity, regardless of the processing method and pore structures.

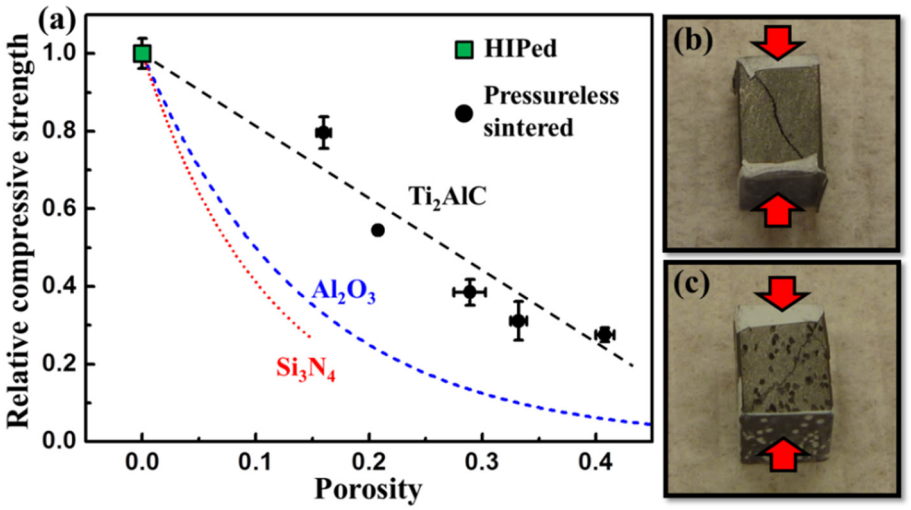

Figure 13. (a) Relative compressive strength of Ti_2AlC as a function of porosity. The loading direction is normal to aligned pore axis. Dots are experimental data of a HIP sample (square, red) [96] and PS samples (round, black). Also included are the corresponding data for Al_2O_3 (dash, blue line) [101] and Si_3N_4 (dash, red line) [103]. Compression samples after testing: (b) a Ti_2AlC sample processed without using NaCl pore former, porosity = 21%; (c) a Ti_2AlC sample processed using 20 vol.% NaCl pore former (355–500 μm), porosity = 33%. Teflon tape was applied between sample and fixture to reduce the effects of friction.

Results of compressive strength measurements are shown in Figure 13. The compressive strength of fully dense Ti_2AlC prepared by HIP [96] was used for comparison, and the "relative compressive strength" of the fully dense Ti_2AlC is 1. All samples failed by cracking in the direction of approximately 45° relative to the loading direction, as it is illustrated in Figure 13. Typical highly porous ceramics crush under compression. In contrast, highly porous Ti_2AlC in the present study shows graceful failures and does not crush. The relative compressive strength of Ti_2AlC decreases to 0.3

as the porosity increases to 42 vol.%. The compressive strength of typical ceramics, *i.e.* Al_2O_3, yttria stabilized zirconia (YSZ), and Si_3N_4 [109-111] drops dramatically with increasing porosity. In contrast, the compressive strength of Ti_2AlC decreases less rapidly and almost linearly with increasing porosity. The reason for this observation must lie in the kinking and kink band formation that are typical for Ti_2AlC, and to the further extend to all MAX phases. In fact, SEM images of fracture surfaces shown in Figure 14(a)–(c) reveal intensive kinking and delamination that dissipated a large amount of mechanical energy during crack propagation. An additional evidence of the exceptional damage tolerance of Ti_2AlC is that standard deviation (3.9–16.0 %) is low.

The compressive strength was also investigated as a function of pore size and loading direction (Figure 14(d)–(f)). Three samples with comparable porosities, *i.e.* 29 %, 33 % and 33%, were tested and the results are shown in Figure 14(d). These samples were processed using NaCl powders with different particle sizes, *i.e.* 45–90 μm, 180–250 μm, and 355–500 μm. Figure 14 shows that the compressive strength decreases with increasing pore sizes. However, this decrease is moderate, approximately 38% for the increase in average pore size of over 6 times, which is also a less rapid drop than what Griffith criterion [112] predicts, *i.e.* the strength of brittle materials containing pores:

$$\sigma = (E\gamma / \pi c)^{0.5} \tag{9}$$

where E is Young's modulus, γ is surface energy, and c is pore size. This observation is additional evidence suggesting high damage tolerance of porous Ti_2AlC.

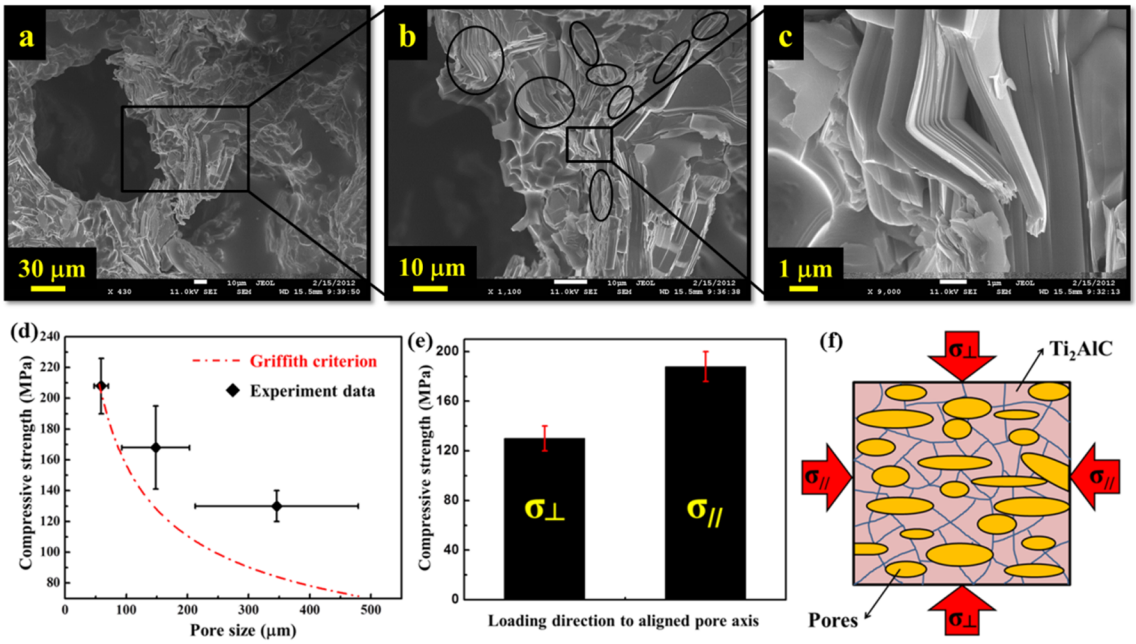

Figure 14. FE-SEM images of fracture surface of a post-compression sample processed with 40 vol.% NaCl pore former (180–250 μm). The porosity is 41%, and the magnification is: (a) × 430, (b) × 1100, and (c) × 9000. Compressive strength as a function of (d) the particle size of NaCl pore former (the loading direction is normal to aligned pore axis) and (e) loading direction, *i.e.* normal ($\sigma_{\perp}$) and parallel ($\sigma_{//}$) to aligned pore axis. The samples were processed with 20 vol.% NaCl pore former (355–500 μm). (f) Schematic of the loading direction versus the aligned pore axis.

To investigate the effect of pore axis orientation with respect to loading direction on compressive strength, specimens from a sample processed with 20 vol.% NaCl pore former (355–500 μm) were machined and tested along two loading directions, *i.e.* normal ($\sigma_{\perp}$) and parallel ($\sigma_{//}$) to aligned pore axis. The results of testing in compression and a schematic of loading direction versus aligned pore axis are shown in Figure 14(e) and (f). The average value of $\sigma_{//}$ was 45% higher than that of $\sigma_{\perp}$, which is consistent with the results reported in literature [113] for the samples with the similar pore structures, *i.e.* unidirectional pore alignment. As illustrated in Figure 14(f), the

effective solid area parallel to aligned pore axis is larger than that normal to aligned pore axis, which most likely explains why the value of $\sigma_{//}$ is higher than that of $\sigma_{\perp}$. This indicates that loading direction is an additional factor which should be taken into account for the evaluation of compressive strength of the Ti_2AlC foams with elliptical pores.

4.3.6. Thermal Properties

Figure 15 shows room temperature thermal conductivity of the Ti_2AlC foams as a function of porosity and pore size. The thermal conductivity decreases significantly with increasing porosity from 34 to 60 vol.%, while it hardly changes as the particle size of the NaCl pore former changes from 45–90 μm to 180–250 μm to 355–500 μm. This suggests that porosity is an effective parameter for tailoring thermal conductivity, but pore size hardly affects thermal conductivity. Figure 15(a) shows that the experimental data agreed well with Bruggeman's model as specified in reference [114]:

$$\lambda_{Eff} = \lambda_{MAX} (1 - P)^{1.5} \quad (10)$$

where λ_{Eff} and λ_{MAX} respectively represent thermal conductivities of the Ti_2AlC foams and fully dense Ti_2AlC. P is the volume fraction of pores.

The experimental results were also compared with theoretical bounds in Figure 15(b). Hashin and Shtrikman [115] derived bounds for effective thermal conductivity that were the narrowest bounds for macroscopically homogeneous, two-phase materials. Their upper bound was mathematically equivalent to the well-known Maxwell-Eucken model:

$$\lambda_{Eff} = \lambda_{MAX} \frac{2\lambda_{MAX} + \lambda_{Air} - 2(\lambda_{MAX} - \lambda_{Air}) \cdot P}{2\lambda_{MAX} + \lambda_{Air} + (\lambda_{MAX} - \lambda_{Air}) \cdot P} \quad (11)$$

where λ_{Air} represents the thermal conductivity of air. The thermal conductivity of air and fully dense Ti_2AlC of 0.026 W/mK [116-118] and 46 W/mK [119], respectively, were used in this study.

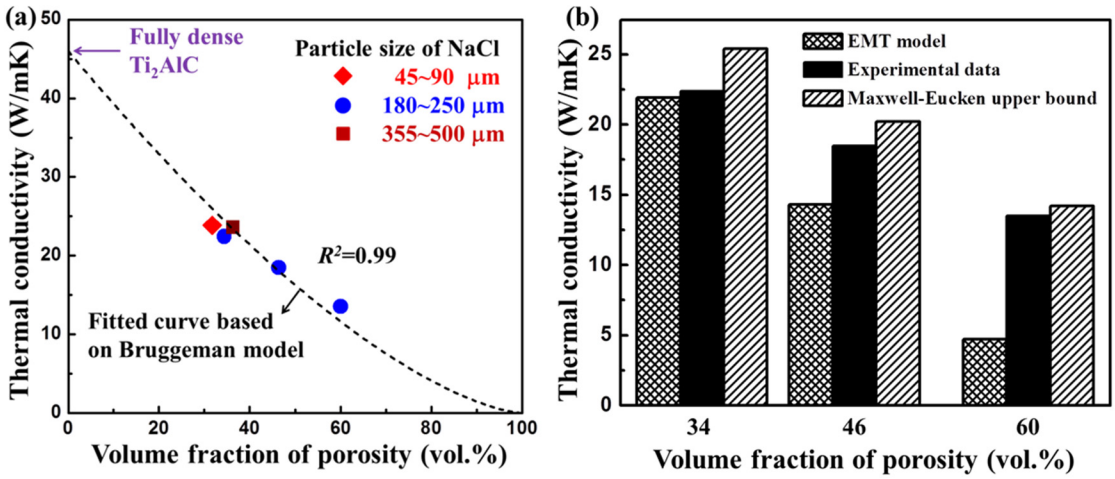

Figure 15. Room temperature thermal conductivity versus porosity and pore size (*i.e.* particle size of NaCl pore former). (b) Comparison of the experimental results with the theoretical models (*i.e.* the EMT model and the Maxwell-Eucken upper bound).

In a heterogeneous material structure in which the two components are distributed connectively, either component may form continuous heat conduction pathways, depending on the relative amounts of the components. Carson [120] developed Landauer's theory [121] and reported that the effective thermal conductivity of this specific structure could be modeled well by the effective media theory (EMT) equation:

$$(1-P)\frac{\lambda_{MAX}-\lambda_{Eff}}{\lambda_{MAX}+2\lambda_{Eff}}+P\frac{\lambda_{Air}-\lambda_{Eff}}{\lambda_{Air}+2\lambda_{Eff}}=0 \quad (12)$$

The experimental results in Figure 15(b) usually lie between the Maxwell-Eucken upper bound and the EMT model. The observed decline of thermal conductivity with increasing porosity could be explained by the microstructure features developed within the Ti_2AlC foam. First, pores trapped air, which is a better thermal insulator (*i.e.* lower thermal conductivity) than the highly conductive Ti_2AlC. Second, these air-filled pores constitute obstacles against the heat transfer along thermal gradient direction. Third, large amounts of interconnected pores made the ceramics grains dispersed or not continuous, blocking the heat conduction pathways and also contributing to the remarkably low thermal conductivity. Fourth, the large number of pores and pore-grain interfaces provided significant phonon and photon scattering, which significantly lower the thermal conductivity.

4.4. Summary and Conclusions

The present work reported a simple and inexpensive method for processing Ti_2AlC foams with controlled porosity and pore size using NaCl as pore former. Ti_2AlC foams with a wide range of porosity from 10 to 71 vol.% were processed using different volume contents of NaCl pore former. The samples with pores that were uniformly distributed in the Ti_2AlC matrix were processed by varying both pore former particle size and pore former volume content. Higher porosities could be achieved by using finer Ti_2AlC powders with the same volume percent of NaCl pore former. The present method

was also used for processing Ti_2AlC with graded porosities, which could lead to graded functional properties. Elastic moduli of the Ti_2AlC foams decreased with increasing porosity, which agrees well with the exponential model, Hasselman model, and composite spheres model. Compressive strength decreased with increasing porosity or pore size. The drop of compressive strength is less rapid than that in common ceramics due to kinking and kink band formation. Room temperature thermal conductivity decreased with increasing porosity, but hardly changed with increasing pore size. The experiment results of thermal conductivity were located between the predictions of the effective media theory model and Maxwell-Eucken upper bound.

CHAPTER V

A RAPID INFILTRATION APPROACH TO HIGH-PERFORMANCE METAL/TERNARY CARBIDE COMPOSITES WITH CONTROLLED MICROSTRUCTURES

Based on the ternary carbide foams prepared in the previous chapter, a rapid infiltration method is developed to fabricate metal/ternary carbide composites with metastable or far-from-equilibrium compositions and customizable structures. The new composites were systematically characterized to determine their composition, microstructure, and mechanical properties. It is clearly shown that customizable structures help realize tailored and sometimes unprecedented properties, *e.g.* light-weight, high strength, and high energy dissipation at both room and elevated temperatures. These properties are vital to improving energy efficiency in aerospace and transportation, power generation, and energy conversion

5.1. Introduction

One way to process metal/MAX phase composites with marginal reactions and active constituents is to infiltrate molten metals into MAX phase foams. In fact, a pressureless infiltration technique has been used to process Ti_2AlC/Mg composites that exhibit higher strength and mechanical energy dissipation than other Mg composites [24]. However, the pressureless infiltration is not an easy task because of the poor wettability of MAX phase foam with molten metals. The poor wettability slows

infiltration and sometimes makes infiltration impossible; it can also yield weak bonding between metals and ceramics, resulting in inferior mechanical properties of the composites [53]. This problem can be overcome by using pressure infiltration to force molten metals into ceramic foams. However, in many cases the ceramic-metal reaction is so fast that even in pressure infiltration new phases would form. The new phases not only cage the pores to prevent further infiltration, but also degrade the constituents of the composites. Thus, reducing reaction is the most challenging issue of fabricating metal/MAX phase composites.

Aluminum is the most attractive metal used in ceramic-metal composite materials for aerospace and transportation applications, where weight of the composite materials is critical. Particularly, development of newer generation aircraft calls for aluminum alloy with high performance in an extended temperature range. An approach to obtain improved high-temperature properties is to combine aluminum alloy and ceramics, such as Al_2O_3 [61-63], B_4C [64-66], and SiC [67-69], in composite materials. However, MAX phases have not been used in aluminum-based composites until two recent studies on Ti_3AlC_2/Al composites [21] and aluminum alloy/Ti_2AlC composites [22].

The introduction of MAX phases in aluminum composites brings several additional advantages, which could not otherwise be obtained using traditional ceramics, *e.g.* Al_2O_3, B_4C, or SiC. First, a typical MAX phase, like Ti_3SiC_2, has higher fracture toughness (~7 MPa·$m^{1/2}$) than Al_2O_3 (~4 MPa·$m^{1/2}$), B_4C (~3.7 MPa·$m^{1/2}$), and SiC (~4.6 MPa·$m^{1/2}$). The high toughness reduces the sensitivity of the composites to brittle

fracture. Second, unlike the traditional ceramics, MAX phases have high transport properties that originate from the atomic bonding with mixed covalent, ionic, and metallic characters. The high transport properties retain the functional properties of aluminum, namely thermal and electrical conductivities. Third, MAX phases can be compressed to stresses as high as 1 GPa and fully recover their original, undeformed shapes upon removal of the stress while dissipating 25% of the mechanical energy. The addition of MAX phases in aluminum introduces mechanical energy dissipation to the composites, which is unique comparing to traditional ceramic/Al composites. Lastly, unlike traditional ceramics, MAX phases are machinable even at room temperature, which reduces the manufacturing cost. Therefore, aluminum/MAX phase composites deserve further investigations.

It was shown in our previous work [22] that a current-activated, pressure-assisted infiltration (CAPAI) is a viable method for producing interpenetrating aluminum alloy/MAX phase composites. One of the consequences of using the new method is that highly-reactive composite systems could be fabricated; these composites could not otherwise be fabricated using conventional methods due to poor wettability and severe reactions [22]. This becomes prominent in expanding the ceramic-metal composite family and exploring additional applications of the composites. In the present work, use is made of a combination of the CAPAI method and MAX phase foams with customizable pore structures to enable manipulating structures of aluminum alloy/MAX phase composites. We characterize the microstructures and micro-tomography of the resulting composites, develop the reaction mechanisms during processing, and tailor the

compressive strength of the composites by controlling their microstructures. We discuss the possibility of adapting this method in designing complex hierarchical structures to mimic natural composites.

5.2. Experimental Details

Ti_2AlC powders (MAXthal 211, Sandvik Heating Technology AB, Sörkvarnsvägen, Sweden) with particle size in the 45–90 μm range, and NaCl powders (Sigma-Aldrich, St. Louis, MO, USA) with a variety of particle sizes, *i.e.* 45–90 μm, 180–250 μm, and 355–500 μm, were used to process Ti_2AlC foams using procedures described elsewhere [77]. The preparation of the foams involves three steps: (i) cold pressing a NaCl-Ti_2AlC powder mixture with 20/80 or 40/60 volume ratio; (ii) dissolving the NaCl in distilled water, and (iii) pressureless sintering of the Ti_2AlC under flowing argon at 1400 ^oC for 4 hours. Pore size of the foams was determined by measuring the size of 50 pores in SEM images using the intercept method, as specified in ASTM E112-13 [78]. Four SEM images from randomly selected locations on each sample were used. Aluminum alloy 6061 (AA6061) discs (McMaster-Carr, GA) with a diameter of 20 mm and a thickness of 4 mm were used for the infiltration process.

A disc (20 mm in diameter and 4 mm in thickness) of Ti_2AlC foam was "sandwiched" in between two AA6061 discs and placed in a graphite die, followed by infiltration at 750 ^oC under 5 MPa uniaxial pressure for 1 minute. The "sandwich" set-up enables more uniform infiltration of molten metal. The infiltration was carried out in a spark plasma sintering system (SPS 25-10, GT Advanced Technologies, CA). A direct

current was applied from 0 to 1250 A in 4 min and stabilized at 860 A for 1 min at 750 ^{o}C; the pulse cycle was 10 ms on and 10 ms off. The chamber was evacuated and held at 10^{-6} torr for 10 minutes before heating. The heating rate was 200 ^{o}C/minute. It takes less than 10 minutes for a complete infiltration process including heating/melting, soaking, and cooling/solidification. Graphite foils were applied between samples and graphite die before infiltration. The temperature was calibrated and measured using procedures described elsewhere [48].

The density and porosity (both open and closed) were determined by alcohol immersion method based on Archimedes' principle, as specified in ASTM C20-00 [122]. The theoretical density values of 4.11 (g/cm^3) [74] and 2.70 (g/cm^3) [73] for Ti_2AlC and aluminum, respectively, were used to calculate the theoretical density of composites using the rule of mixture. It was assumed that the effect of eventual reaction on the theoretical density is negligible. The relative density equals the measured value divided by the rule-of-mixture value, *i.e.* 3.55 g/cm^3.

The phase composition of the starting powders and the as-infiltrated composites was determined using an X-ray diffractometer, XRD (*D8* Discover, Bruker, WI) with Cu *Kα* radiation (wavelength = 1.542 Å) at 40 kV and 30 mA. The two theta range was from 8 ^{o} to 80 ^{o} with a step size of 0.04 ^{o} and a step time of 1.5 s. The XRD results were analyzed utilizing the Inorganic Crystal Structure Database (ICSD). The microstructure, phase composition and distribution were characterized using a Field Emission Scanning Electron Microscopy, FE-SEM (JSM-7500F, JEOL, Tokyo, Japan), equipped with Energy Dispersive Spectroscopy (EDS). Also used was another FE-SEM (Zeiss Ultra

Plus, Carl Zeiss, Oberkochen, Germany) equipped with an Oxford Instrument AZtec EDS and a Nordlys-S Electron Backscatter Diffraction (EBSD) system. The accelerating voltage and emission current were 15 kV and 20 mA, respectively. The duration of spot scan of EDS was 60 seconds per spectrum. The EBSD scans were run with an accelerating voltage of 12 kV, an aperture size of 60 μm or 120 μm depending on the specimen, and a step size of 0.3 μm. The 3D microstructure showing the phase distribution was obtained using an Xradia MicroXCT-400 Micro-Computed Tomography (Zeiss, Germany). The composition of the AA6061 and the Al alloy in the composite was measured using a Cameca SX-100 electron microprobe with a wavelength dispersive spectrometry (WDS) system.

The compressive strength and damping capability of the samples was measured by using a universal testing machine (MTS810, MTS, MN) with a strain rate of 1.4×10^{-4} s^{-1}. All samples for compressive testing were cut by electrical discharge machining to dimensions of 3.5 mm × 3.5 mm × 7 mm.

5.3. Results and Discussion

5.3.1. Microstructural Characterization

Figure 16(a)–(c) show SEM images, respectively, of the Ti_2AlC foams with different pore sizes, *i.e.* 42–83 μm, 77–276 μm, and 167–545 μm. The pores were fabricated using NaCl particles as pore formers. All three foams were fabricated using the same volume percent (40 vol.%) of the NaCl particles and have comparable overall porosities of 40.8, 41.6 and 39.9 vol.%. The infiltration of these three foams with

AA6061 resulted in 40%AA6061/Ti_2AlC composites with different interpenetrating phase sizes, as shown in Figure 16(d)–(f). The interpenetrating phase size is the formerly pore size in the foams before infiltration. To illustrate and compare the macroscopic structures, the insets in Figure 16 are photographs of both the foams and the composites. Despite the short processing time, the porosity data (not shown here) show that more than 97% of the open porosity in the foams was infiltrated with molten metal.

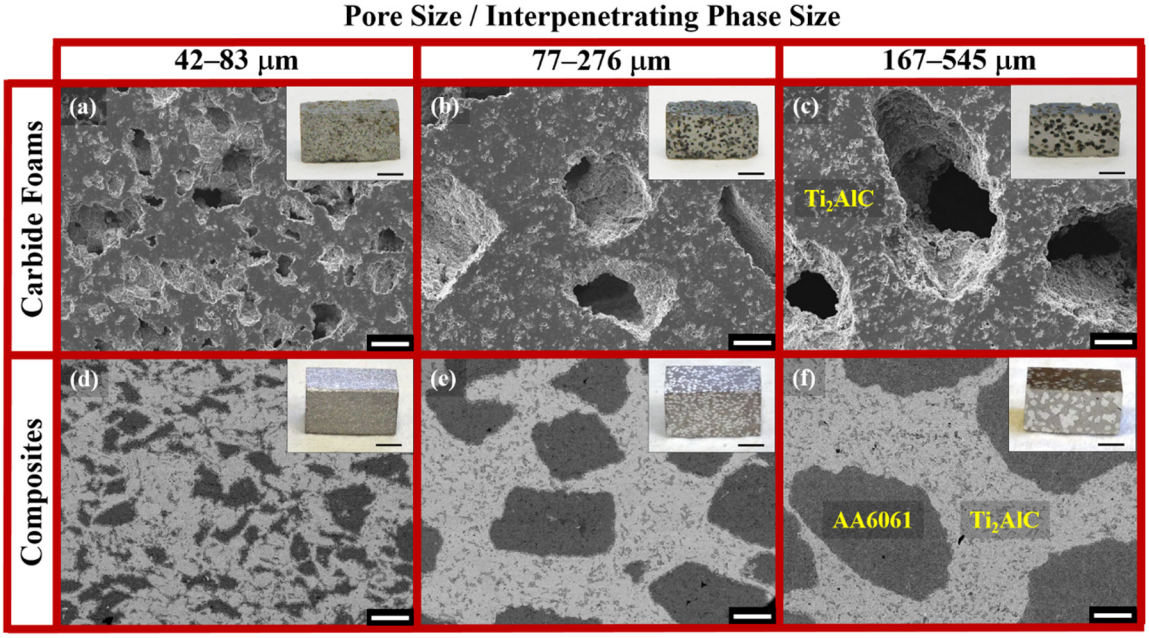

Figure 16. SEM images of Ti_2AlC foams with different pore sizes fabricated using NaCl particles as pore formers; the ranges of the pore size are (a) 42–83 μm, (b) 77–276 μm, and (c) 167–545 μm. All three foams were fabricated using the same volume fraction (40 vol.%) of the NaCl particles. The infiltration of these three foams with AA6061 resulted in AA6061/Ti_2AlC composites with different interpenetrating phase sizes: (d) 42–83 μm, (e) 77–276 μm, and (f) 167–545 μm; the interpenetrating phase size are formerly pore size in the foams before infiltration. Insets show photographs of both the foams and the composites after electrical discharge machining to dimensions of 3.5 mm × 3.5 mm × 7 mm. Scale bars in optical photograph: 2mm. Scale bars in the SEM images: 100 μm. Scale bars in the photographs: 2 mm.

Another observation is that marginal reactions were observed at interfaces between the two phases (Figure 16(d)–(f)). With negligible reactions, it is the pore shape and size that determine the interpenetrating phase shape and size. It follows from the above that the CAPAI method has two advantages in comparison with the conventional methods. The two advantages are as follows:

1. The results indicate that the CAPAI allows processing of new, highly reactive composites, which could not otherwise be obtained using conventional methods.
2. The CAPAI offers an efficient route to manipulate the composite structures by controlling the porosity and pore size of the ceramic foams. The ability to manipulate structures cannot be overemphasized, because it could enable complex hierarchical designs to mimic natural composites, which has generated enormous interest but has yielded few practical advances [123].

An additional observation is that the fracture surface of the Ti_2AlC foams (not shown here) illustrates the connectivity of Ti_2AlC grains and formation of the sintering necks. The network of grains with well-developed sintering necks is critical to obtain high-strength composites, and further examples are considered below.

It is interesting to see how the two-dimensional (2-D) microstructure described above develops in 3-D space. Figure 17 shows micro-CT images of the constituents of the 40%AA6061/Ti_2AlC composites with interpenetrating phase sizes of 167–545 μm. Unlike the 2-D morphology shown in Figure 17(f), where AA6061 is mostly scattered, the 3-D tomography image shows connectivity of AA6061 (Figure 17(a)). In fact, both AA6061 and Ti_2AlC have 3-D networks that penetrate each other; the volume percent of

AA6061 and Ti_2AlC in the composites is about 40 vol.% and 60 vol.%, respectively. A comparison between the Ti_2AlC constituent in the composite (Figure 17(b)) and the Ti_2AlC foam (not shown here) shows that the Ti_2AlC structure is preserved. Again, it suggests that it is the pore shape and size in the MAX phase foams that determine the interpenetrating phase shape and size in the composites.

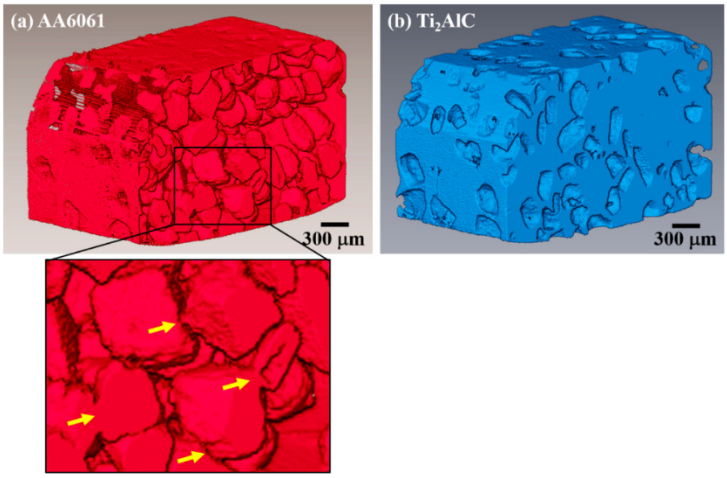

Figure 17. Micro-CT images of the constituents of a cuboid specimen: (a) AA6061, and (b) Ti_2AlC. The dimensions of the cuboid specimen are 1.8 mm × 1.8 mm × 2.3 mm, and the interpenetrating phase size is 167–545 μm. Scale bars: 300 μm. Arrows in an enlarged view of (a) show the connectivity of the Al alloy.

The structure obeserved here is radically different from that previously reported by Wang *et al.* [21] in the Ti_3AlC_2/Al composites. The Ti_3AlC_2 particles in the Ti_3AlC_2/Al composites were hardly sintered due to low processing temperatures, *i.e.* 550 ^oC. On the contrary, the Ti_2AlC in the composites presented here was sintered separately at 1400 ^oC prior to the infiltration process. For the Ti_3AlC_2/Al composites, the temperature choice is dictated by the melting point of Al, *i.e.* 660 ^oC; higher temperatures than the melting point of Al would trigger substantial and harmful

reactions. However, typical sintering temperatures of Ti_3AlC_2 or Ti_2AlC are around 1400 ^oC [77]. Low temperatures, such as 550 ^oC, are not enough for the sintering of either phase. A solution to the problem of weak ceramic networks in composites processed by the powder co-sintering method is to use pre-sintered ceramic foams as preforms for infiltration of molten metals, as demonstrated in the present work. Note that the temperature used in the present work, *i.e.* 750 ^oC, is significant higher than that used by Wang *et al.*, *i.e.* 550 ^oC. However, marginal reactions were observed, and constituents were preserved in the composites. How this happens is considered next.

5.3.2. Compositional, Phase, and Texture Analyses

Figure 18(a) shows XRD results of the composites and the starting materials, namely, AA6061 and Ti_2AlC. In addition to the major phase, Ti_2AlC, the Ti_2AlC powder contains some Ti_3AlC_2 and a small amount of Al_2O_3. These two impurities come with the commercial powder. For the composites, Ti_2AlC, Ti_3AlC_2 and Al are three major phases in the presence of a small amount of Al_2O_3. All phases identified in the composites were also found in the starting materials, and no new phases were detected. Although a new phase, titanium aluminide, was identified in the composites by both EDS and EBSD, its amount is so small that it is not detectable in the XRD.

Figure 18(b) shows backscattered SEM images of the composite at different magnifications. Table 7 lists the EDS results of spot analysis in Figure 18(b). The results include atomic percent, Ti / Al ratio, and Al / O ratio of spots 1, 2, 3, and 4 indicated in Figure 18. EBSD results from Figure 19 are also listed for comparison. Note that carbon

is not shown in the EDS results because of significant quantifying errors for this specific element. The Ti / Al ratios of spots 2 and 3 are 0.35 and 1.96, respectively, which agree with the EBSD phase identifications of $TiAl_3$ and Ti_2AlC (Figure 19). Similarly, the Al / O ratio of 0.69 suggests a phase of Al_2O_3, which is confirmed by the EBSD results (Figure 19). Although $TiAl_3$ most likely comes from Al-Ti_2AlC reactions, Al_2O_3 has two possible sources. These sources include raw material impurity (Figure 18(a)) and surface oxidation of Al. How $TiAl_3$ occurs is considered in Section 3.1.3.

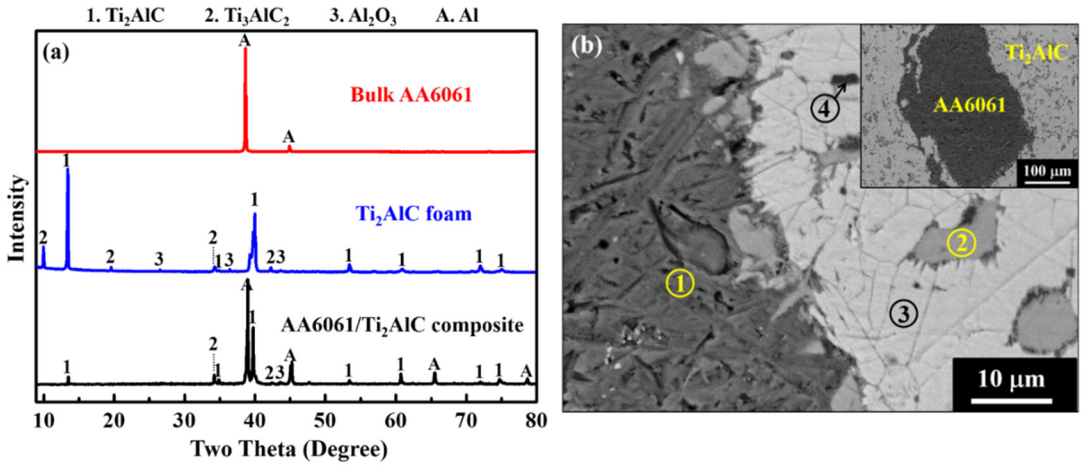

Figure 18. (a) XRD results of the AA6061/Ti_2AlC composite and its pure constituents, namely AA6061 and Ti_2AlC. The identification of phases was done according to the Inorganic Crystal Structure Database (ICSD) collection code 165460 for Ti_2AlC, 153266 for Ti_3AlC_2, 10425 for Al_2O_3, and 43423 for Al. (b) Backscattered SEM image of the composite showing AA6061 (1, dark grey), titanium aluminide (2, light grey), Ti_2AlC (3, light), and Al_2O_3 (4, dark). Inset shows a backscattered SEM image at low magnification. The composition of phases 1, 2, 3, and 4 are determined according to the EDS results (Table 7) and EBSD results (Figure 19).

To illustrate further the reaction phases, Figure 19 shows a phase map and four element maps, namely Ti, Al, C, and O, of the composite with interpenetrating phase sizes of 167–545 µm. Both identified and unidentified phases are color coded in the

phase map. As listed in Table 8, 82.0 % of all phases were identified, and 18.0 % were not identified. The identified phases include Ti_2AlC, Ti_3AlC_2, Al, $TiAl_3$, and Al_2O_3. The percent of each phase is listed in Table 8. Al_2O_3 is present in both ceramic and metallic phase regions. The Al_2O_3 in the ceramic phase region most likely comes from the raw materials (Figure 18(a)), whereas the Al_2O_3 in the metallic phase region most likely results from surface oxidation.

Table 7. EDS results of spot analysis in Figure 18(b). EBSD results from Figure 19 are also listed for comparison.

Location	EDS results					EBSD results
	Atomic percent[(a)], at.%			Ti / Al ratio	Al / O ratio	Phase
	Ti	Al	O			
1	0	92	0	⋯	⋯	Al
2	24	68	0	0.35	⋯	$TiAl_3$
3	47	24	0	1.96	⋯	Ti_2AlC
4	0	37	54	⋯	0.69	Al_2O_3

[(a)]Carbon is not shown in the EDS results because of significant quantifying errors for this specific element.

The unindexed, black regions have three possible sources. First, the black dots with sizes of approximately 10 μm in the Ti_2AlC region are pores. Second, the black dots with sizes less than 1 μm at interfacial area are unindexed because of the height difference between Al and Ti_2AlC. The height difference was generated during polishing, because Al and Ti_2AlC have different wear rates, and some shadow areas prevented the scattering of the electrons in these areas. Third, the black, straight lines with lengths of 50–150 μm are scratches, which were introduced during polishing. A

significant amount of $TiAl_3$, *i.e.* 7.3 % (Table 8), was identified at either the interfacial region or the ceramic phase regions. The $TiAl_3$ in the interfacial region forms a "ring", surrounding the Al phase and separating it from the ceramic phases. A comparison between the phase map and a SEM image of the Ti_2AlC foam suggests that the locations of the $TiAl_3$ at the ceramic phase region are formerly the pores on the ceramic walls where molten Al could reach and react with Ti_2AlC during the infiltration process.

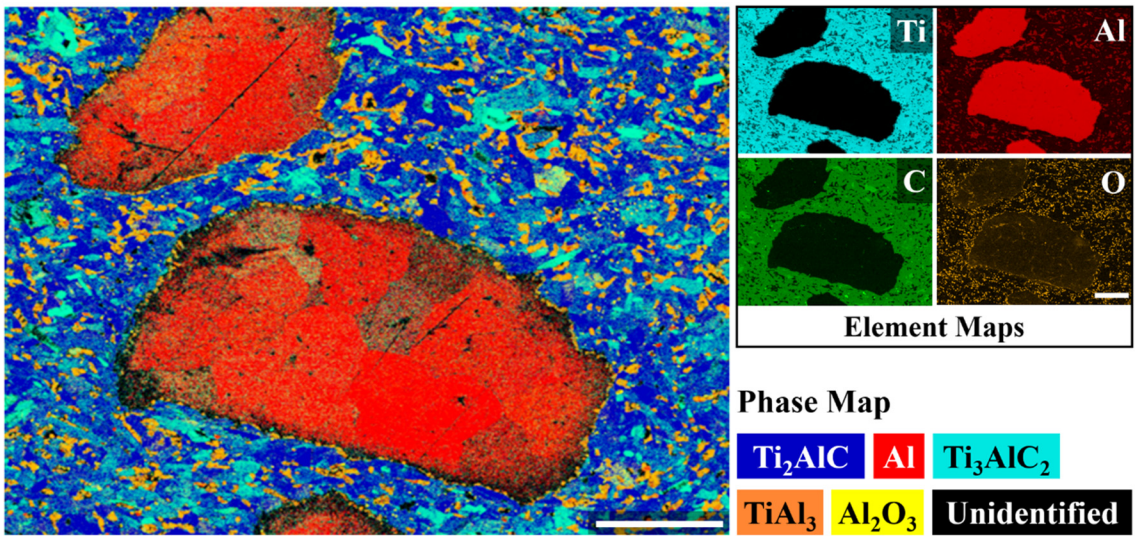

Figure 19. A phase map and four element maps, namely Ti, Al, C, and O, of the AA6061/Ti_2AlC composite with interpenetrating phase sizes of 167–545 μm. Both identified and unidentified phases are color coded in the phase map. 82.0 % of all phases were identified, and 18.0 % were not identified. The identified phases include Ti_2AlC, Ti_3AlC_2, Al, $TiAl_3$, and Al_2O_3. The percent of each phase is listed in Table 8. Scale bars: 100 μm.

A common reaction phase, titanium aluminide, was found in both the composites presented here and the previously reported Ti_3AlC_2/Al composites [21]. Indeed, the Ti-Al-C phase diagram [54] clearly shows that Al reacts with Ti_3AlC_2 at 727 °C to form titanium aluminide. However, the composites presented here have less titanium

aluminide than the Ti_3AlC_2/Al composites. The Ti_3AlC_2/Al composites were processed at a lower temperature but with a longer time than the AA6061/Ti_2AlC composites presented here. Thus, the processing time plays an important role in reducing reactions, and the short time associated with the CAPAI method presented here becomes particularly prominent in the case of reactive ceramic-metal systems.

Table 8. Color and percent of phases in the phase map of Figure 4.

Phase	Ti_2AlC	Al	Ti_3AlC_2	$TiAl_3$	Al_2O_3	Unidentified
Color	Blue	Red	Cyan	Orange	Yellow	Black
Percent (%)	39.9	17.9	15.1	7.3	1.8	18.0

The results presented up to this point along with related advances shown in the literature indicate that reactions between Al alloy and the ternary carbide are marginal in the CAPAI method, but could be considerable and become a limiting factor in conventional methods. Therefore, it is important to know how Al alloy reacts with the ternary carbide during the processing. In the present study, two possible mechanisms could explain the formation of $TiAl_3$. First, $TiAl_2$ reacts with Al to form $TiAl_3$:

$$TiAl_2 + Al = TiAl_3 \quad (13)$$

where $TiAl_2$ is an impurity phase that comes with the Ti_2AlC commercial powder. Although the $TiAl_2$ is not shown on the XRD pattern of the Ti_2AlC foam, it is present and identified by EDS in the back scattered SEM images of both Ti_2AlC powder and foams (results not shown). More importantly, the content of the $TiAl_2$ in the Ti_2AlC foam approximately equals to that of the $TiAl_3$ in the composites. This is a compelling evidence that enhances the plausibility of the reaction given in the above reaction (13).

The other possible mechanism for the formation of $TiAl_3$ lies in the reaction between Al and Ti_3AlC_2, a common companion phase that comes with the Ti_2AlC powder. In the process of fabricating Ti_3AlC_2/Al composites, Wang *et al.* [21] found that the reaction between Al and Ti_3AlC_2 depends on temperature. For temperatures below 900 ^oC, the Ti-Al-C ternary phase diagram [124] suggests a reaction path as follows:

$$32\ Al + 3\ Ti_3AlC_2 = 2\ Al_4C_3 + 9\ TiAl_3 \quad (14)$$

The composition and distribution of the phases in the AA6061/Ti_2AlC composite shown in the present work agree with the reaction given in the above reaction (14). Although the presence of $TiAl_3$ was confirmed by both EDS (Figure 18(b)) and EBSD (Figure 19), the Al_4C_3 was absent in both cases. The absence of Al_4C_3 on the surface of specimens prepared for EDS and EBSD could be due to its dissolution by contact with water during polishing; the dissolution is as follows [125]:

$$Al_4C_3 + 12\ H_2O \rightarrow 4\ Al(OH)_3 + 3\ CH_4 \quad (15)$$

Indeed, both $TiAl_3$ and Al_4C_3 were also observed in reactivity studies of the Al-Ti_3SiC_2 system [126, 127]. Two observations from the phase map in Figure 19 enhance the plausibility of reaction (15). First, $TiAl_3$ in the ceramic phase region is located close to black dots (unidentified phase) or contains black dots itself. The unidentified, black phases most likely are pores that resulted from the dissolution of Al_4C_3. Second, the $TiAl_3$ "ring" that surrounds the Al phase and separates it from the ceramic phases is non-continuous and consists of micron-sized orange dots ($TiAl_3$). These non-continuous, orange dots are connected by black dots, which are probably pores that resulted from the dissolution of Al_4C_3.

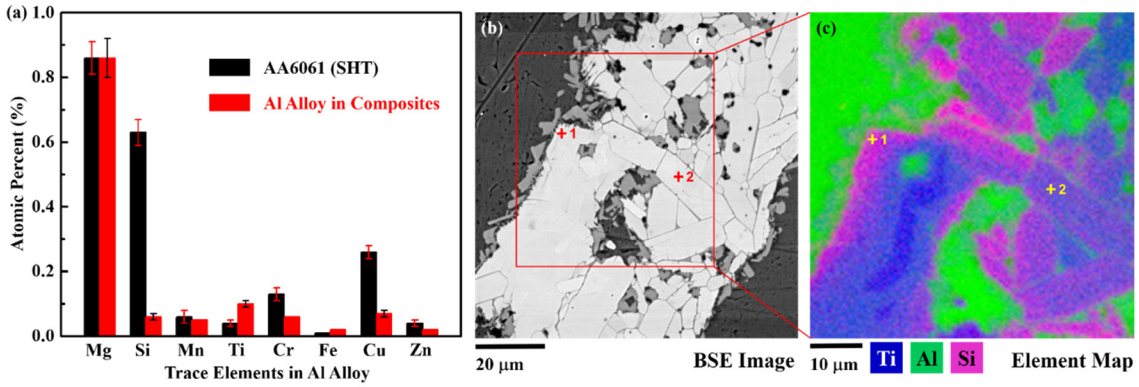

Figure 20. (a) Atomic percent of the trace elements in solution heat treated (SHT) AA6061 and Al alloy in the composites. (b) A back scattered SEM image showing phase distribution (dark grey: Al alloy, grey: $TiAl_3$, and light: Ti_2AlC) around the Al alloy-Ti_2AlC interfaces inside the composites. (c) An X-ray map showing Si diffusion from Al alloy to the Ti_2AlC. Red crosses annotate locations where microprobe quantitative analyses were carried out. The quantitative analyses results are shown in Table 9.

AA6061 is a heat-treatable alloy, and its composition and local misorientation within grains influence strengthening of the composites. The local misorientation within grains of the Al alloy in the composites are investigated in the following two sections. Figure 20(a) displays a comparison of atomic percent of trace elements in Al alloy in the composites against those in a solution heat treated (SHT) AA6061. The atomic percent of silicon (Si) and copper (Cu) in the Al alloy significantly decreased after the infiltration process, indicating out-diffusion of these two trace elements. The diffusion of Cu is most probably driven by reactions between Cu and the ternary carbide and its companion phases [128]. The evidences of Si diffusion are observed in an X-ray map taken around the interfaces inside the composite (Figure 20(c)), and Figure 20(b) shows a back scattered SEM image on the location where the X-ray map was taken. The amount of Si in the Ti_2AlC grains displays a clear, continuous gradation of

concentration; the concentration is high at regions adjacent to the Al alloy but low at regions towards the center of Ti_2AlC grains.

Table 9. Microprobe quantative analyses results of locations 1 and 2 in Figure 20.

Location	Atomic percent, %				Ti / (Al+Si)	Si / (Al+Si)	Probable phase
	Al	Si	Ti	C			
1	20.0	7.3	54.0	18.7	2.0	0.3	$Ti_2(Al_{0.7},Si_{0.3})C$
2	25.2	3.1	53.6	18.1	1.9	0.1	$Ti_2(Al_{0.9},Si_{0.1})C$

Microprobe quantitative analyses show the composition of two locations marked in the back scattered SEM image and the X-ray map (Table 9). The Si concentration is higher at location 1 than at location 2, because location 1 is closer to the Al alloy – the Si source. The Ti / (Al+Si) ratio approximately equals to 2 at both locations, indicating substitution of Al with Si. The substitution could lead to the formation of $Ti_2(Al_x,Si_{1-x})C$ solid solution or co-existence of two phases, namely Ti_2AlC and Ti_2SiC. A further characterization on nanometer scale is required to identify the crystal structure at these two locations.

A typical orientation or inverse pole figure (IPF) map of grains in the AA6061/Ti_2AlC composites is shown in Figure 21(a). Grains with uniform colors denote ones in which little evidence for plastic deformation was observed. The rainbow colored grains, on the other hand, indicate ones in which plastic deformation occurred. A zoom-in image of the region within the rectangular frame in Figure 21(a) is shown in Figure 21(b); the region is labeled as area A. Figure 21(c) shows the trace of the misorientation angle along line B in Figure 21(b), indicating that significant deformation occurred. The

misorientation angle between two points, C and D, along the line B is approximately 12 degrees. These two points are near the two ends of the line and are approximately 60 μm apart from each other. Some Ti_2AlC grains also showed deformations. Although deformation was observed in only a few Ti_2AlC grains, it is common in most AA6061 grains. The presence of local misorientation and therefore local plastic strains in AA6061 plays an important role in the compressive response of the composites.

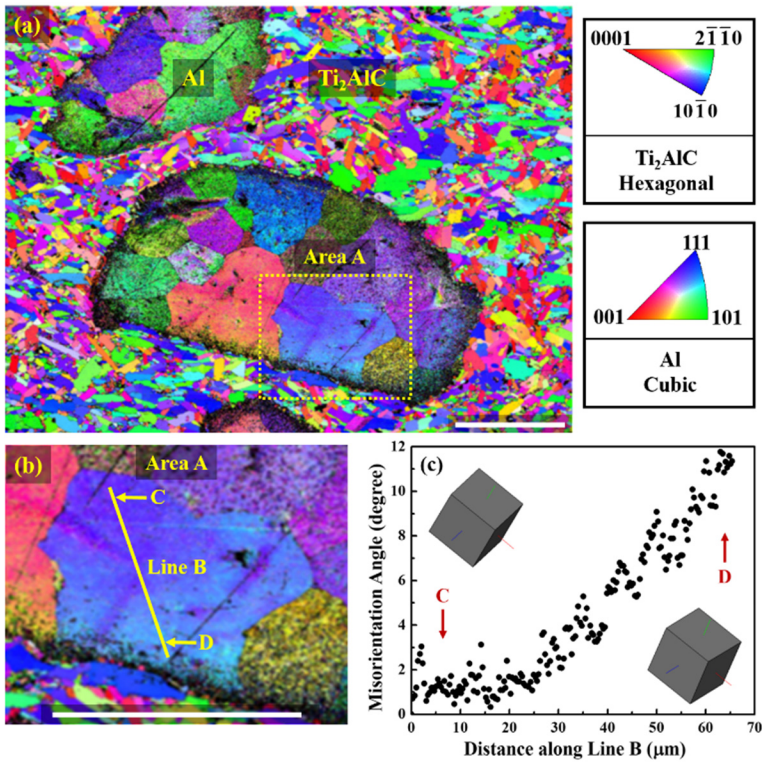

Figure 21. (a) A typical inverse pole figure (IPF) map of grains in the as-processed composites. Grain with uniform colors denote ones in which little evidence for plastic deformation was observed (which is mostly the case for the ceramic grains). The rainbow colored grains (which are almost all the aluminum grains), on the other hand, indicate ones in which plastic deformation occurred and has resulted in local misorientations. (b) A zoom-in image of the region within the rectangular frame in (a); the region is labeled as area A. (c) trace of the misorientation angle along line B in 5(b), indicating that significant deformation occurred in the AA6061 grain. Scale bars: 100 μm.

5.3.3. Compressive Properties

It has been demonstrated up to this point that the CAPAI method allows the processing of new composites with customizable structures. The section below demonstrates that the customized structures could be utilized to tailor compressive properties and that the CAPAI method can also result in superior compressive properties of the composites in comparison with their pure constituents.

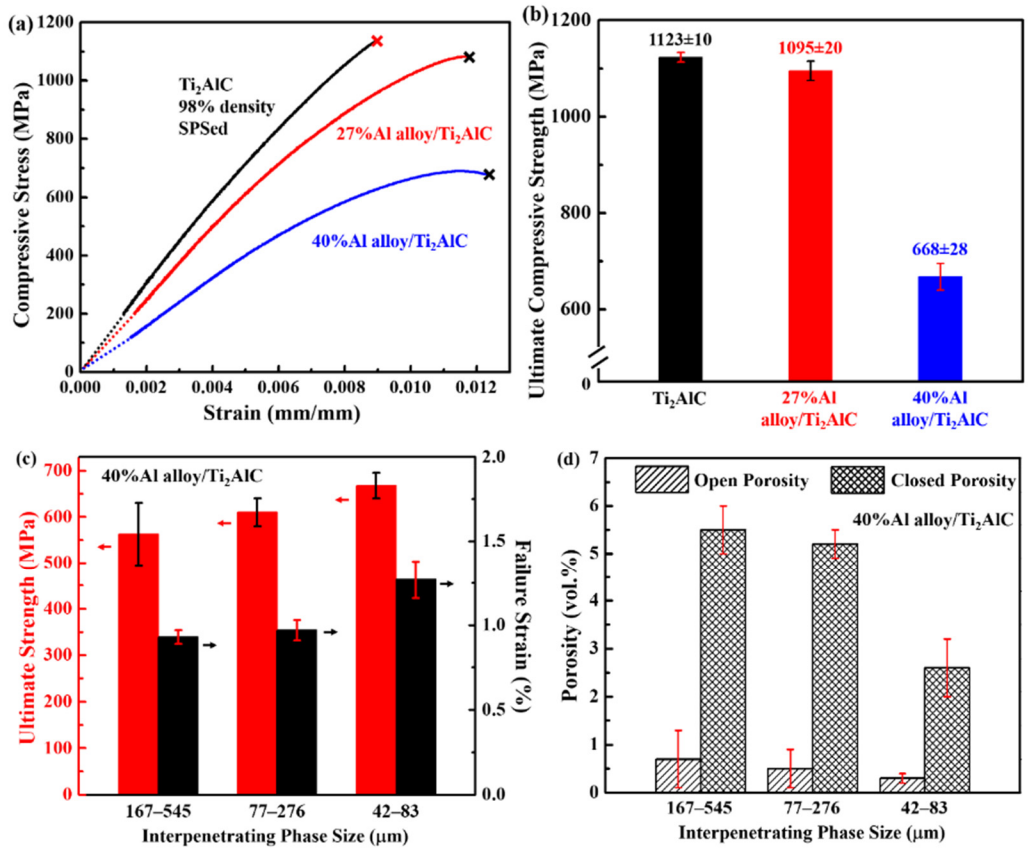

Figure 22. (a) Typical compressive stress-strain curves of Ti2AlC, 27%Al alloy/Ti2AlC, and 40%Al alloy/Ti2AlC. (b) Ultimate strength of Ti2AlC, 27%Al alloy/Ti2AlC, and 40%Al alloy/Ti2AlC. (c) Ultimate strength and failure strain of the composites with different interpenetrating phase sizes. (d) Open and closed porosities of the composites as a function of interpenetrating phase size. The interpenetrating phase size is formerly the pore size of the Ti2AlC foams.

Figure 22(a) shows typical compressive stress-strain curves of Ti_2AlC, 27%AA6061/Ti_2AlC, and 40%AA6061 alloy/Ti_2AlC, and Figure 22(b) shows their ultimate strengths. Figure 22(c) shows both ultimate strength and failure strain of the AA6061/Ti_2AlC composites with interpenetrating phase sizes of 42–83 μm, 77–276 μm, and 167–545 μm. Both strength and failure strain of the composites decrease with the interpenetrating phase size. For example, the compressive strength and failure strain of the composites with interpenetrating phase size of 42–83 μm are approximately 20% and 35%, respectively, higher than those of the composites with interpenetrating phase size of 167–545 μm. The differences in compressive strength and failure strain lie in the differences of porosity and phase boundary area that are responsible for arresting crack propagations, each of which is illustrated or explained below.

To illustrate the difference of porosity in these three composites and to relate the porosity difference to the compressive behavior, Figure 22(d) shows porosity (both open and closed) of the composites shown in Figure 22(c). Note that, whereas the composites with interpenetrating phase sizes of 167–545 μm and 77–276 μm have similar open and closed porosities, the composites with interpenetrating phase sizes of 42–83 μm have significantly lower open and closed porosities than the other two composites. It is well known that porosity of the composites plays an important role in the rupture of the composites and thus affect the compressive strength, and that the compressive strength decreases with increasing porosity [110]. Thus, the composites with interpenetrating phase sizes of 42–83 μm demonstrate the highest compressive strength. It follows from the above that it is possible to fabricate composites with even smaller interpenetrating

phase sizes and thus higher strengths. With the high compressive strength, the composites with interpenetrating phase sizes of 42–83 μm were chosen for further characterization of mechanical properties, as shown in the following two sections.

Phase boundary area is responsible for arresting crack propagations (Figure 25), and the difference in the phase boundary area relates to the differences in compressive strength and failure strain. Given a fixed volume percent of interpenetrating phase, the phase boundary area increases with decreasing interpenetrating phase size. With the most phase boundary area, the composite with the finest interpenetrating phase size has the most effective crack arrests and thus exhibits the highest compressive strength and failure strain.

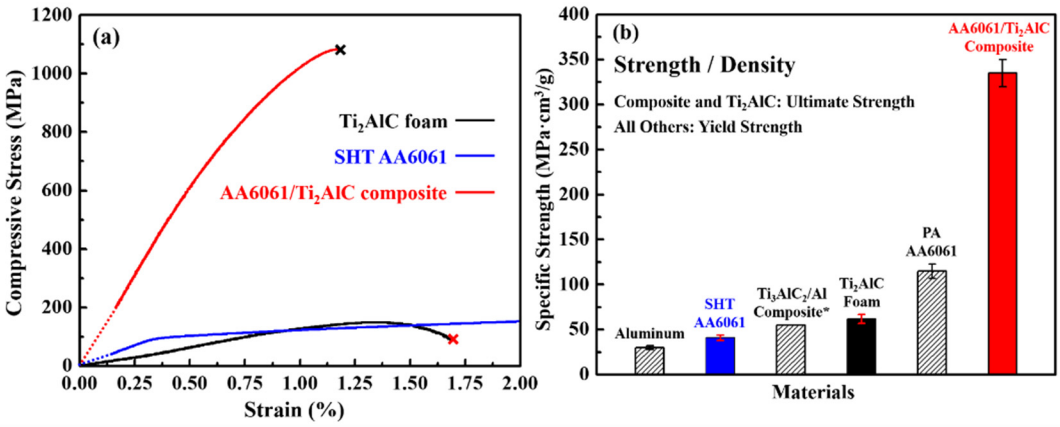

Figure 23. (a) Typical compressive stress-strain curves of the 27%AA6061/Ti_2AlC composites, solution heat treated (SHT) AA6061, and Ti_2AlC foam. (b) Specific strength of the AA6061/Ti_2AlC composites, peak aged (PA) AA6061, and Ti_2AlC foam, the Ti_3AlC_2/Al composites [21], solution heat treated AA6061, and pure aluminum.

Figure 23(a) shows typical compressive stress-strain curves of the 27%AA6061/Ti_2AlC composites, solution heat treated (SHT) AA6061, and Ti_2AlC

foam. SHT AA6061 is more comparable with the condition of aluminum alloy in the composite. The ultimate strength of the composite is 1095 MPa, which is about 7 times that of the Ti_2AlC foams (150 MPa) and about 10 times the yield strength of the SHT AA6061 (110 MPa [21]). Figure 23(b) shows that the specific strength, *i.e.* compressive/yield strength divided by density, of the composite is 335 MPa·cm^3/g, which is about 5 times that of the Ti_2AlC foam (62 MPa·cm^3/g), 3 times that of the peak aged (PA) AA6061 (115 MPa·cm^3/g [22]), 6 times that of previously reported value of the Ti_3AlC_2/Al composite (55 MPa·cm^3/g [21]), and 5 times the yield strength of the SHT AA6061 (41 MPa·cm^3/g). Post-testing analysis of fracture surfaces (Figure 25) shows evidences of the crack propagation resistance in the composite.

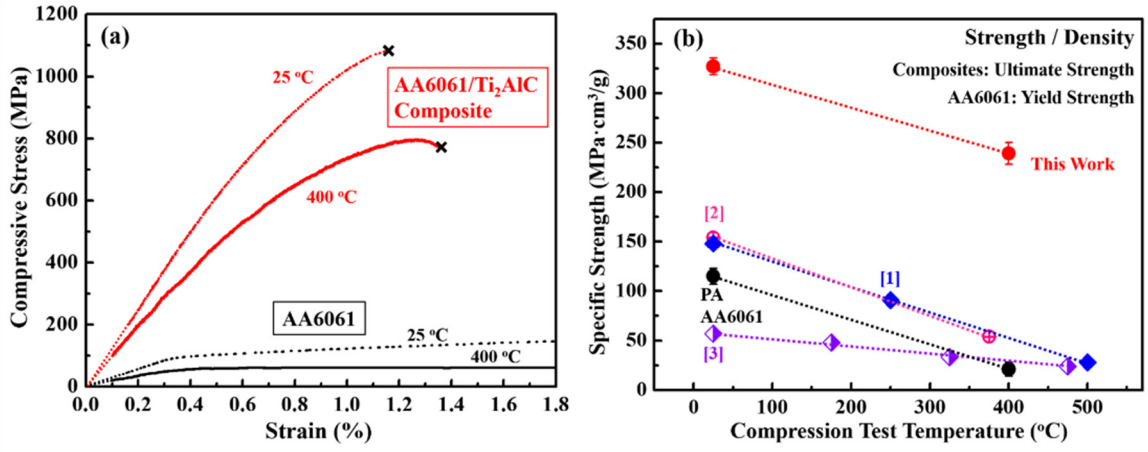

Figure 24. (a) Compressive stress-strain curves of the 27%AA6061/Ti_2AlC composites and AA6061 at 25 °C and 400 °C. (b) Specific strength as a function of compression test temperature for the 27%AA6061/Ti_2AlC composites from the present study (red curve), Ti_3AlC_2/Al composites [21] (blue curve [1]), B_4C/Al composites [64] (pink curve [2]), Al_2O_3/Al composites [62] (purple curve [3]), and PA AA6061 (black curve).

Figure 24(a) shows typical compressive stress-strain curves of the composites and PA AA6061 at 25 ^{o}C and at 400 ^{o}C. Note that AA6061 creeps at 400 ^{o}C, which is approximately 0.7 times the melting point of aluminum. The ultimate strength of the composites at 400 ^{o}C (800 MPa) is approximately 14 times the yield strength of AA6061 at 400 ^{o}C (58 MPa) and is even 2.5 times the yield strength of AA6061 at room temperature (300 MPa).

Although the strength of the composites is higher than that of PA AA6061 at both room and elevated temperatures, the failure strain of the composites is smaller than that of PA AA6061. In other words, the introduction of ceramic strengthens aluminum at the expense of ductility. The trade-off between strength and ductility is not unusual. In fact, this trade-off has been observed in other aluminum-ceramic composites. Compressive properties, *i.e.* yield strength, ultimate strength, and failure strain, at both room and elevated temperatures of a number of aluminum-ceramic composites are listed in Table 4.

Table 10. Compressive properties, *i.e.* yield strength, ultimate strength, and failure strain, at both room and elevated temperatures of a number of aluminum-ceramic composites.

Composite systems		Volume percent of ceramic (%)	Properties at room temperature			Properties at elevated temperatures				Reference
Aluminum	Ceramic		Yield strength (MPa)	Ultimate strength (MPa)	Failure strain (%)	Yield strength (MPa)	Ultimate strength (MPa)	Failure strain (%)	Test temperature (^{o}C)	
6061	Ti_2AlC	73	1035±20	1095±20	1	755	800	1	400	This work
6061	Ti_2AlC	60	630±30	668±28	1	400±30	426±37	1	400	This work
Al	Ti_3AlC_2	40	174	190	4	145	160	2	175	[21]
						100	110	1	325	
						65	80	1	475	
Al-2wt.%Cu	Al_2O_3	30	400	520	5	…	…	…	…	[61]
Al	B_4C	55	350	400	4	100	140	10	375	[64]
Al-13Si-9Mg	SiC	48	…	405	…	…	…	…	…	[67]
Al	Al_2O_3	34	390	464	3	236	284	3	250	[62]
						85	87	1	500	

These aluminum-ceramic composites include AA6061/Ti_2AlC from the present study, Ti_3AlC_2/Al [21], Al_2O_3/Al-2wt.%Cu [61], B_4C/Al [64], Al_2O_3/Al-13Si-9Mg [64], and Al_2O_3/Al [62]. According to the data in Table 4, the specific strength as a function of compression test temperature for Ti_3AlC_2/Al [21], B_4C/Al [64], and Al_2O_3/Al [62] composites was plotted in Figure 24(b) for comparison with that for the AA6061/Ti_2AlC composites and AA6061. The specific strength of the AA6061/Ti_2AlC composites is the highest among the composites and is about twice and 5 times, respectively, that of the AA6061 at room temperature and at 400 ^oC. Note that the AA6061/Ti_2AlC composites were processed by infiltration of molten aluminum in pre-sintered Ti_2AlC foams, whereas other composites were processed by co-sintering of aluminum-ceramic powder mixtures. The difference in compressive strength between the AA6061/Ti_2AlC composites and other composites could be related to constituent materials and the microstructural differences originated from the different processing methods. The remainder of this section demonstrates these differences and their correlation to compressive properties. The Ti_3AlC_2/Al composites [21] were chosen to represent the aluminum-ceramic composites processed by conventional methods.

Three observations on the differences in both constituent materials and microstructures could account for the fact that the compressive strength of the AA6061/Ti_2AlC composites is much higher than that of the previously reported Ti_3AlC_2/Al composites [21]. These observations are listed below.

(1) The Ti_3AlC_2/Al composites were processed from Al-Ti_3AlC_2 powder mixtures using hot isostatic pressing [21]. However, the AA6061/Ti_2AlC composites were

processed by the SPS-assisted infiltration of AA6061 on Ti_2AlC foams [22]. After processing, their microstructures were composed of a hard continuous skeleton of Ti_3AlC_2 distributed in the Al matrix [21] and two interpenetrating networks of AA6061 and Ti_2AlC [22], respectively, in the Ti_3AlC_2/Al and the AA6061/Ti_2AlC composites. The microstructure differences play a central role in the different mechanical behaviors of the composites.

(2) The Ti_2AlC in the AA6061/Ti_2AlC composites were pressureless-sintered at 1400 ^oC separately prior to the infiltration, resulting in the strong connectivity of Ti_2AlC grains [22]. In contrast, the Ti_3AlC_2 particles were barely sintered in the Ti_3AlC_2/Al composites, which were processed at low temperature (550 ^oC) to avoid substantial two-phase reactions [21]. Therefore, the strong network is critical to obtain high mechanical strength of the Ti_2AlC, and the strong Ti_2AlC networks contribute significantly to the high compressive strength of the AA6061/Ti_2AlC composites.

(3) In addition to the Ti_2AlC networks, the yield strength of AA6061 is higher than that of Al, *i.e.* 300 MPa for AA6061 vs. 80 MPa for Al, which also contribute to the difference of the compressive strength of the composites.

Therefore, it is clear that the challenge of processing is to control the reaction between aluminum and ceramic, which is the key to control the microstructure and properties of the aluminum-ceramic composites.

The limitation of the powder metallurgy method is that the processing temperature is dictated by the melting point of Al, *i.e.* 660 ^oC, to avoid substantial two-phase

reactions. For Ti_3AlC_2 or Ti_2AlC, however, the typical sintering temperature is around 1400 ^oC. At temperatures below 660 ^oC, the Ti_3AlC_2 or Ti_2AlC particles can barely be sintered to form strong networks. A solution to the problem of weak ceramic networks produced during sintering of metal-ceramic powder mixtures is to use well-sintered ceramic foams as preforms for infiltration of metals: this was demonstrated with the infiltration of AA6061 in a Ti_2AlC foam which was separately sintered to form strong network prior to the infiltration.

Figure 25 shows SEM images of the post-compression composites presenting crack deflection before the metallic phase and crack bridging by the metallic phase. As shown by the photograph in Figure 25(a), all tested samples failed by cracking in the direction of approximately 45 ^{o} relative to the loading direction with a tortuous crack path. This observation suggests that the composite shows a graceful failure and does not crush and fragment under compression. Higher magnification SEM images in Figure 25 of the fracture surface area clearly show that cracks in the ceramic phase were effectively stopped (Figure 25(c–e)), deflected (Figure 25(b, c)), or bridged (Figure 25(b, d, and f)) by the metallic phase. More importantly, no crack between Ti_2AlC and AA6061 has been observed after compression testing, indicating exceptionally strong bonding between the two phases in the composite.

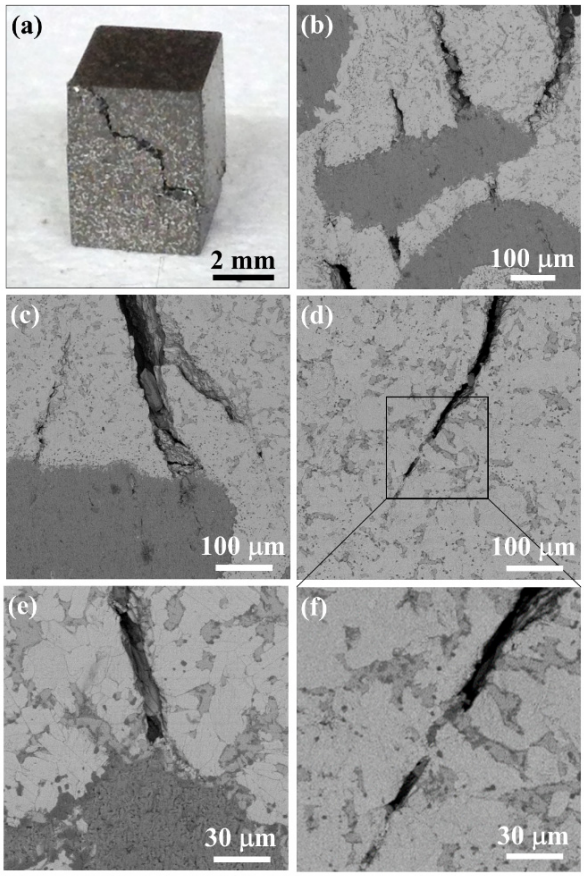

Figure 25. Surface morphology of a post-compression composite. Loading direction was vertical. The inset shows that the sample failed by cracking in the direction of approximately 45 ^{o} relative to the loading direction with a tortuous crack path. Cracks in the ceramic phase were arrested ((b), (c), and (e)), deflected ((b) and (c)), or bridged ((d) and (f)) by the metallic phase.

5.4. Summary and Conclusions

The CAPAI method is used for producing interpenetrating AA6061/Ti_2AlC composites with controlled interpenetrating phase sizes and contents, which were utilized to tailor the compressive properties of the composites. The major findings are summarized as follows.

1. More than 97% of the open porosity in the ceramic preform was infiltrated with molten metal even after a very short processing time. The results suggest that this method offers an efficient route for producing interpenetrating ceramic-metal composites with customizable structures by controlling the structure of the ceramic preform.

2. Little reaction is observed in the AA6061-Ti_2AlC system, which suggests that the CAPAI method can be used to process new, reactive ceramic-metal composite systems, which could not otherwise be obtained using conventional methods.

3. This method can result in composites with superior properties in comparison with those of the constituents. The specific compressive strength of the AA6061/Ti_2AlC composites is about 10 times and 14 times higher than, respectively, the specific yield strength of peak-aged AA6061 at room temperature and at 400 ^oC.

CHAPTER VI

ON THE ENERGY DISSIPATION OF METAL/TI2ALC COMPOSITES UNDER CYCLIC, COMPRESSIVE LOADING

The previous chapter presented a rapid infiltration method to fabricate metal/ternary carbide composites, *i.e.* aluminum alloy/Ti_2AlC. The energy dissipation of the new aluminum alloy/Ti_2AlC composites were systematically characterized. The results are presented in the following chapters. The present study identifies, for the first time, the contributing role of load partitioning in the energy dissipation of metal/MAX phase composites, which not only expands variables responsible for energy dissipation of KNE solids, but also provides an additional tool to tailor the properties of this kind of materials.

6.1. Introduction

In the last 15 years, a new class of nano-layered ternary carbides and nitrides, commonly referred as MAX phases, has attracted considerable attention as potential multi-functional materials for extreme conditions, as they combine some of the best attributes of ceramics and metals [1]. Like binary carbides or nitrides, they are stiff, good thermal and electrical conductors, resistant to chemical attack, and have relatively low thermal expansion coefficients. Unlike their binary counterparts, they are relatively soft and readily machinable, and have good thermal shock resistance and damage tolerance. It is the “semi-metallic” nature of MAX phases that has stimulated the development of

more than a dozen metal/MAX phase composites. In general, the rationale for using the MAX phases in ceramic metal composites is to utilize their unusual properties for (i) light-weight structural composites with exceptional mechanical damping, high specific strength, and/or good oxidation resistance, (ii) low friction, low wear resistant composites for high temperature tribological applications, and (iii) electrically conductive composites with improved mechanical properties in comparison with conductive metals.

A particularly interesting composite class that dissipates remarkably higher mechanical energy than the pure constituents alone is represented by Mg/MAX phase [23, 24] and shape memory alloy (SMA)/MAX phase composites [48, 49]. However, one of the fundamental challenges related to the use of such novel composites is to identify the role of known and possibly new mechanisms in the energy dissipation of this kind of composites. Therefore, important issues related to the "microstructure-property" space of this kind of composites need to be addressed through existing and new composite systems. An example of such new composite system is Al alloy/Ti_2AlC [22], which could assist in understanding the mechanisms responsible for the energy dissipation of metal/MAX phase composites.

Al is the most attractive metal used in ceramic metal composites for energy efficient technologies in aerospace, transportation, power generation, and energy conversion, where lightweight of the composites is critical. Particularly, development of newer generation aircraft calls for Al alloy with high performance in an extended temperature range. An approach to obtain improved high-temperature properties is to

combine Al alloy with ceramics, such as Al_2O_3 [61-63], B_4C [64-66], and SiC [67-69], in composite materials. However, MAX phases have not been used in the Al-based composites until recent studies on Ti_3AlC_2/Al [21] and Al alloy/Ti_2AlC [22]. The introduction of MAX phases in Al-based composites brings additional advantages, which could not otherwise be obtained using traditional ceramics, *e.g.* Al_2O_3, B_4C, or SiC. These advantages are summarized below.

1. A typical MAX phase, like Ti_3SiC_2, has higher fracture toughness (7 $MPa \cdot m^{1/2}$) than Al_2O_3 (4 $MPa \cdot m^{1/2}$) [61-63], B_4C (3.7 $MPa \cdot m^{1/2}$) [64-66], and SiC (4.6 $MPa \cdot m^{1/2}$) [67-69]. The high toughness reduces the sensitivity of the composites to brittle fractures.
2. Unlike common ceramics, MAX phases have high transport properties that originate from atomic bonding with mixed covalent, ionic, and metallic characters [16]. The high transport properties retain the functionalities of the metals.
3. The addition of MAX phases introduces energy dissipation upon mechanical loading. For example, MAX phases can be compressed to stresses up to 1 GPa and fully recover their original shapes upon removal of the stress while dissipating 25% of the mechanical energy [19].
4. Unlike common ceramics, MAX phases are machinable at room temperature [16], which reduces the manufacturing cost of the Al alloy/MAX phase composites.

5. MAX phases are lightweight and the Al alloy/MAX phase composites could achieve unprecedented specific strength (strength divided by density) [22], which is critical for energy efficient technologies in aerospace, transportation, power generation, and energy conversion.

Therefore, Al alloy/MAX phase composites deserve further investigations.

For the metal/MAX phase systems that dissipate more energy than their pure constituents alone, the addition of Al alloy/Ti_2AlC composite in this kind of materials gains insights in the role of known and possibly new mechanisms in the energy dissipation for two reasons. First, in previously reported metal/MAX phase composites, *e.g.* Mg/Ti_2AlC [23], Mg/Ti_3SiC_2 [24], and NiTi/Ti_3SiC_2 [48, 49], both the metal and the MAX phase are hysteresis materials and contribute to the energy dissipation. This complexes the mechanisms that are responsible for the energy dissipation and could be simplified by replacing Mg and NiTi with a non-hysteresis material—Al alloy in the present study. Second, similar to the other metal/MAX phase composites, the Al alloy/Ti_2AlC composites dissipate significantly higher energy than monolithic Ti_2AlC alone. However, the Al alloy/Ti_2AlC composites is unique, because only Ti_2AlC is a hysteresis material and is the sole source for energy dissipation.

The objective of this work is twofold. First, to report on the stress-strain response and energy dissipation of Al alloy/Ti_2AlC composites under cyclic loading of uniaxial compression tests. Second, to understand important variables that lead to enhanced energy dissipation in the metal/Ti_2AlC composites. To achieve the second objective the results are compared to the predictions calculated using a “two-bar” model with isostrain

and isostress assumptions. We also apply the "two-bar" model to the previously reported Mg/Ti_2AlC composites in an attempt to validate the model.

6.2. Experimental Details

6.2.1. Materials and Sample Preparation

Ti_2AlC powders (MAXthal 211, Sandvik Heating Technology AB, Sörkvarnsvägen, Sweden) with particle size in the 45–90 μm range, and NaCl powders (Sigma-Aldrich, St. Louis, MO, USA) with a variety of particle sizes (*i.e.* 45–90 μm, 180–250 μm, and 355–500 μm) were used to process Ti_2AlC foams using procedures as described in another study [77]. The preparation of the foams involves three steps: (i) making tablets by cold pressing from NaCl-Ti_2AlC powder mixtures with 20/80 or 40/60 volume ratios; (ii) dissolving and removing the NaCl (pore former) from the tablets using distilled water, and (iii) pressureless sintering of the porous tablets under flowing argon at 1400 ^oC for 4 hours. Pore size of the foams was determined by measuring the size of 50 pores in SEM images using the intercept method, as specified in ASTM E112-13 [78]. Four SEM images from randomly selected locations on each sample were used. AA6061 discs (McMaster-Carr, GA) with a diameter of 20 mm and a thickness of 4 mm were used for the infiltration process, which is described in another study [22] with more details.

6.2.2. Characterization

The density was determined by alcohol immersion method based on the Archimedes' principle, as specified in ASTM C20-00 [122]. The theoretical density values of 4.11 (g/cm^3) [74] and 2.70 (g/cm^3) [73] for Ti_2AlC and AA6061, respectively, were used to calculate the theoretical density of composites using rule of mixture (ROM). It was assumed that the effect of eventual reactions on the theoretical density is negligible. The relative density equals the measured value divided by the ROM value (*i.e.* 3.55 g/cm^3). The compressive stress-strain curves of the specimens under cyclic loading was measured using a MTS insight electromechanical test frame with a strain rate of 7×10^{-4} s^{-1}. The strain was measured using an MTS extensometer with a gage length of 3 mm, and the extensometer was attached directly on the specimens. All specimens for compressive testing were cut by electrical discharge machining to dimensions of 3.5 mm × 3.5 mm × 7 mm.

Elastic moduli were measured by resonant ultrasound spectroscopy (RUS; Magnaflux Quasar Systems, NM). RUS is based on measuring the spectrum of the resonant mechanical vibrations from a specimen with known geometry, dimensions, and mass [96-98]. All samples for RUS were machined until sharp edges and a parallelism with less than 1% error of thickness were achieved. Specimens (3.5 mm × 3.5 mm × 7 mm) were placed on top of three piezoelectric transducers. One of the transducers (the transmitting transducer) generates an elastic wave at a constant amplitude but varying frequencies, whereas the other two transducer detects the response from the specimen—resonant spectrum. The multidimensional algorithm Quasar RuSpec (Magnaflux Quasar

Systems, NM) iteratively minimizes error between the measured and calculated resonant peaks by changing the initially "guessed" elastic constants till converging values are achieved. Young's modulus was then determined from the measured resonant spectrum.

6.2.3. Analysis—the "Two-Bar" Model

The bounds of the load carried by each phase in the composites are considered, assuming that the two phases are two parallel bars under loading [129]. For the upper bound, it is assumed that the two-phase interface is coherent, so that the deformation of both phases is the same (an isostrain situation). Under these conditions, the total load sustained by the composite $F_c(N)$ equals the summation of loads carried by the Al alloy $F_1(N)$ and the Ti_2AlC $F_2(N)$, or

$$F_c = F_1 + F_2 \tag{16}$$

For the isostrain situation (*e.g.* upper bound), it is shown [130] that the ratio of the load carried by the Al alloy $F_1(N)$ to that carried by the Ti_2AlC $F_2(N)$ is

$$\frac{F_1}{F_2} = \frac{E_1 V_1}{E_2 V_2} \tag{17}$$

where E_1 (68 GPa [73]) and V_1 are the Young's modulus and volume fraction of the Al alloy, and E_2 (277 GPa [1]) and $V_2 = 1 - V_1$ are the Young's modulus and volume fraction of the Ti_2AlC. The volume fraction of Al alloy is determined as the porosity of the Ti_2AlC foam, assuming that all pores are open and later occupied by the Al alloy. The combination of equations (16) and (17) results in the expressions of loads carried by the

Al alloy $F_1(N)$ and the Ti2AlC $F_2(N)$ in terms of known variables, *i.e.* $F_c(N)$, $E_1(GPa)$, V_1, $E_2(GPa)$, and V_2:

$$F_1 = \frac{E_1 V_1}{E_1 V_1 + E_2 V_2} \cdot F_c \tag{18}$$

$$F_2 = \frac{E_2 V_2}{E_1 V_1 + E_2 V_2} \cdot F_c \tag{19}$$

The area (mm^2) of each phase is $A_1 = V_1 \cdot A$ and $A_2 = (1 - V_1) \cdot A$, where V_1 =0.27 or 0.4 and A is the area (mm^2) of the cross section plane perpendicular to the loading directions. The external applied stress is $\sigma_c = \frac{F_c}{A}$. So the stresses carried by the Al alloy $\sigma_1(MPa)$ and the Ti2AlC $\sigma_2(MPa)$ are

$$\sigma_1 = \frac{F_1}{A_1} = \frac{E_1 V_1}{E_1 V_1 + E_2 V_2} \cdot \frac{F_c}{V_1 \cdot A} = \frac{E_1 \cdot \sigma_c}{E_1 V_1 + E_2 V_2} \tag{20}$$

$$\sigma_2 = \frac{F_2}{A_2} = \frac{E_2 V_2}{E_1 V_1 + E_2 V_2} \cdot \frac{F_c}{(1 - V_1) A} = \frac{E_2 \cdot \sigma_c}{E_1 V_1 + E_2 V_2} \tag{21}$$

For the lower bound (the isostress situation), the stresses carried by the Al alloy $\sigma_1(MPa)$ and the Ti2AlC $\sigma_2(MPa)$ are the same and equal the external applied stress $\sigma_c(MPa)$:

$$\sigma_1 = \sigma_2 = \sigma_c \tag{22}$$

The $W_d(\sigma_c)$ value of the composites at a stress of σ_c has two sources:

$$W_d(\sigma_c) = W_d^1(\sigma_1) \cdot V_1 + W_d^2(\sigma_2) \cdot V_2 \tag{23}$$

where $W_d^1(\sigma_1)$ is the dissipated energy obtained when Al alloy is cycled to a peak stress of σ_1, and $W_d^2(\sigma_2)$ is the dissipated energy obtained when Ti_2AlC is cycled to a peak stress of σ_2. To determine the $W_d(\sigma_c)$ values for the upper bound (the isostrain situation), the σ_1 and σ_2 values are from equations (20) and (21), respectively. To determine the W_d values for the lower bound (the isostress situation), the σ_1 and σ_2 values are from equation (22).

6.3. Results and Discussion

6.3.1. Compressive Stress-Strain Curves

Figure 26(a) shows typical stress-strain curves obtained when Ti_2AlC, Al alloy/Ti_2AlC, and solution heat treated (SHT) Al alloy were cycled under compression. The SHT Al alloy was cycled to a peak stress that is slightly lower than its yield strength (110 MPa [22]). The stress-strain curves of the SHT Al alloy are linear and closed, as it is a linear elastic solid. In contrast, the stress-strain curves of both Ti_2AlC and Al alloy/Ti_2AlC describe closed loops after the first loading-unloading cycle—a characteristic feature of kinking nonlinear elastic (KNE) solids. The width of the closed loops increases with the applied stress. The loops are reversible for a small number of cycles. The nonlinear and hysteretic curves originate from formation and annihilation of incipient kink bands (IKBs) [19]. The first cycle is slightly open and suggests an irrecoverable strain, but all subsequent cycles are closed and fully reversible. The irrecoverable strain in the first cycle is much smaller than the reversible strain (Figure

26(b)–(d)). In the present study, only the closed, fully reversible loops are considered and measured as the dissipated energy per unit volume per cycle—$W_d\,(MJ\,/\,m^3)$.

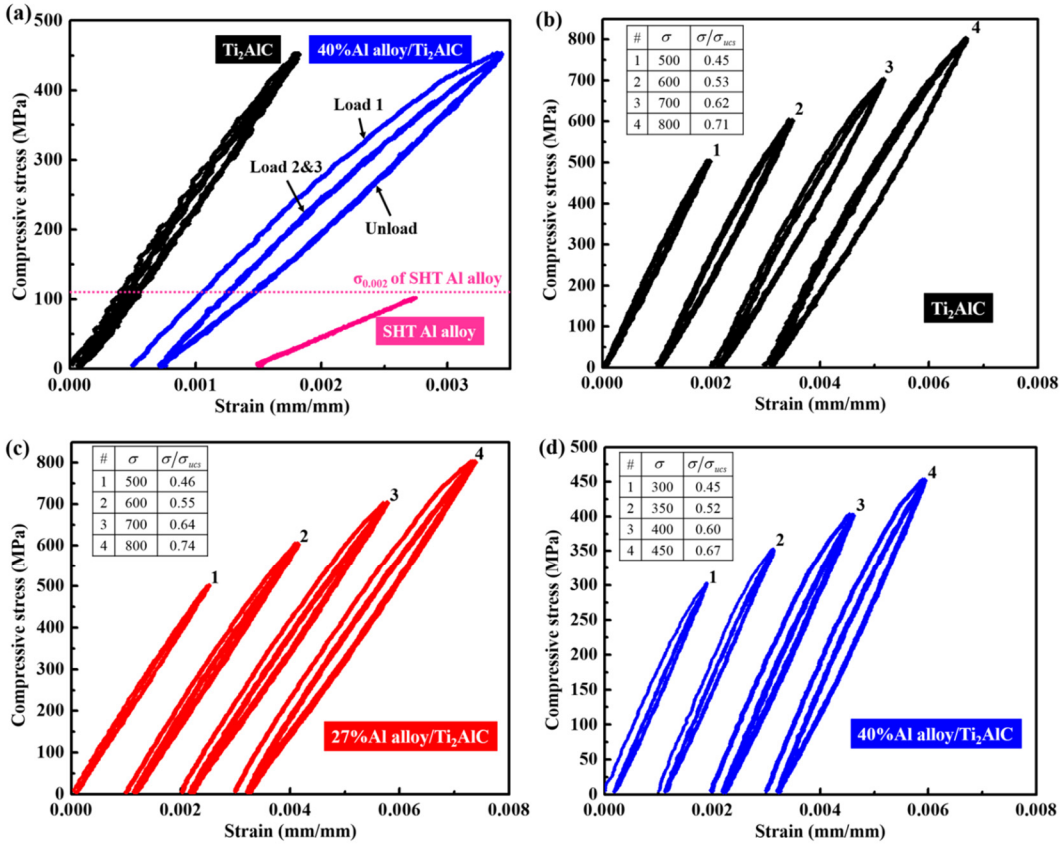

Figure 26. (a) Typical compressive stress-strain curves obtained when Ti_2AlC, 40% Al alloy/Ti_2AlC, and solution heat treated (SHT) Al alloy were cycled three times to a peak stress of 450 MPa, 450 MPa, and 100 MPa, respectively. The pink, dash line represents the yield strength $\sigma_{0.002} = 110(MPa)$ of the SHT Al alloy. The other three plots show compressive stress-strain curves obtained when (b) Ti_2AlC was cycled three times to a peak stress of $\sigma(MPa)$, where $\sigma = 500$, 600, 700, and 800, (c) 27%Al alloy/Ti_2AlC composite was cycled three times up to a peak stress of $\sigma(MPa)$, where $\sigma = 500$, 600, 700, and 800, and (d) 40%Al alloy/Ti_2AlC composite was cycled three times up to a peak stress of $\sigma(MPa)$, where $\sigma = 300$, 350, 400, and 450. The highest peak stress value $\sigma_{\max}\,(MPa)$ is determined such that $\sigma_{\max}/\sigma_{ucs} \approx 0.7$, where $\sigma_{ucs}(MPa)$ is the ultimate compressive strength.

Figure 26(b)–(d) show that the Al alloy/Ti_2AlC composites exhibit larger W_d than Ti_2AlC at a comparable ratio σ/σ_{ucs}, and the W_d increases with increasing volume percent of Al alloy in the composites. The comparison is based on the ratio of the peak stress $\sigma(MPa)$ to the ultimate compressive strength $\sigma_{ucs}(MPa)$ — σ/σ_{ucs}. For example, Figure 26(b) shows compressive stress-strain curves obtained when Ti_2AlC was cycled three times to a peak stress of $\sigma(MPa)$, where σ = 400, 500, 600, and 700. The highest peak stress value $\sigma_{\max}$ is determined such that $\sigma_{\max}/\sigma_{ucs} \approx 0.7$ to avoid significant damages, because previous studies suggest that MAX phases can be cycled up to 0.7 of their $\sigma_{ucs}(MPa)$ with little degradation or change in the loop sizes and shapes [19]. To that end, internal damages are monitored by measuring the Young's modulus, *E(GPa)*, of the specimens after each cyclic compression. Significant drop of *E* would indicate damages inside the specimen. For example, the full characterization of Ti_2AlC as shown in Figure 26(b) involves 1) measuring *E* of the as-processed specimen, 2) cyclic compression to a peak stress of 500 MPa, 3) measuring *E*, 4) cyclic compression to a peak stress of 600 MPa, 5) measuring *E*, 6) cyclic compression to a peak stress of 700 MPa, 7) measuring *E*, 8) cyclic compression to a peak stress of 800 MPa, and 9) measuring *E*. From the measured values of Young's modulus, relative Young's modulus (E/E_0) as a function of applied stress is determined, where *E* is the measured value of Young's modulus of the post-compression specimen after each cyclic loading and E_0 is the measured value of Young's modulus of the as-processed specimen.

Figure 27(a) shows relative Young's modulus (E/E_0) as a function of applied stress for both the composites and Ti_2AlC. The relative Young's modulus decreases as the applied stress increases, even though the overall change is small, *i.e.* 0.003 for Ti_2AlC, 0.013 for 27%Al alloy/Ti_2AlC, and 0.008 for 40%Al alloy/Ti_2AlC. The overall change of the relative Young's modulus of the composites is larger than that of the Ti_2AlC over a comparable range of the ratio σ/σ_{ucs}. This indicates more internal damage of the composites in comparison with Ti_2AlC. The same indication follows the observation that the irrecoverable strain of the composites is larger than that of Ti_2AlC over a comparable range of the ratio σ/σ_{ucs} (Figure 27(b)). The irrecoverable strain was measured from the compressive stress-strain curves, and a statistical analysis was carried out on three specimens in each case to calculate the average values and standard deviation as shown in Figure 27(b).

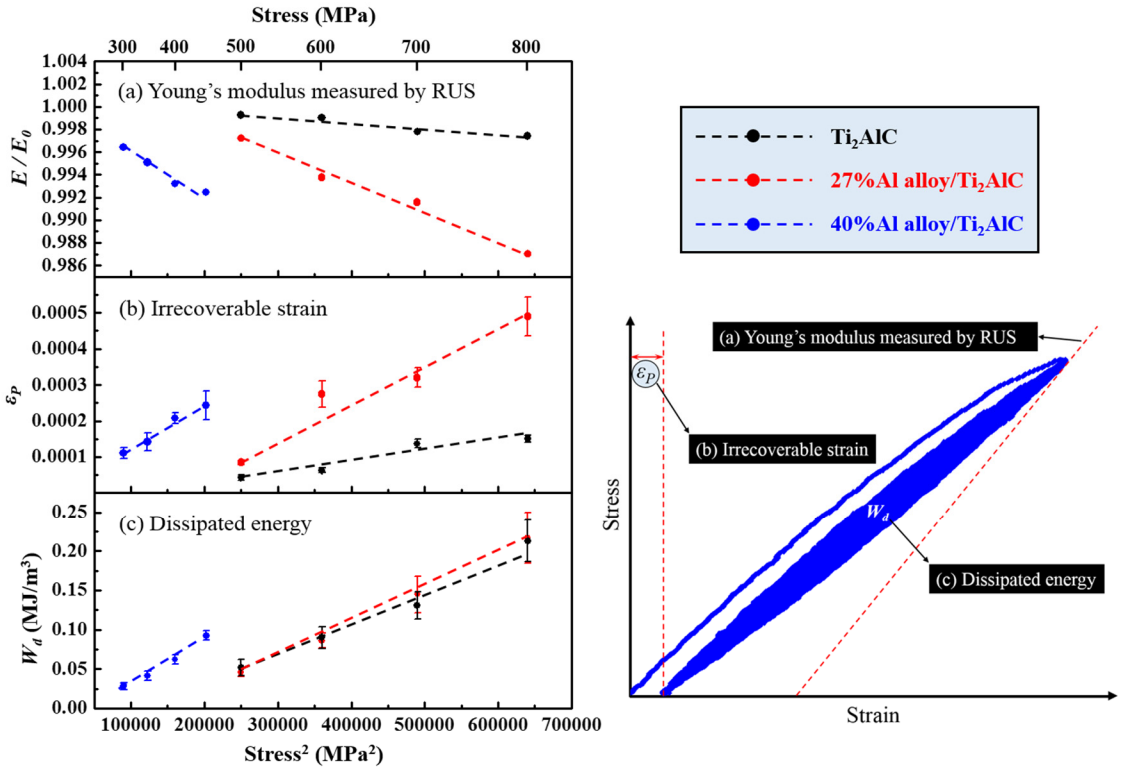

Figure 27. Characteristics of stress-strain curves of Ti_2AlC, 27%Al alloy/Ti_2AlC, and 40%Al alloy/Ti_2AlC: (a) relative Young's modulus E/E_0, (b) irrecoverable strain ε_P, and (c) dissipated energy W_d. All characteristics are illustrated in the inserted schematic. The relative Young's modulus at a stress of σ_c was determined by dividing the Young's modulus of the material after a cyclic loading at the stress of σ_c with the value of the Young's modulus of the as-processed material.

A couple of factors could account for the more internal damages developed in the composites than those in the Ti_2AlC. Previous studies have shown that the "soft" metallic phase in Mg/Ti_2AlC [23] and Mg/Ti_3SiC_2 [24] composites eases the Ti_2AlC grains and the Ti_3SiC_2 grains to kink. Similarly, the presence of a metallic phase (Al alloy) in the Al alloy/Ti_2AlC composites eases the formation of damages (*e.g.* microcracks, permanent kinking bands, and delamination). Second, unlike pure, fully dense Ti_2AlC, the Ti_2AlC in the Al alloy/Ti_2AlC composites carries a higher load than

the external applied load, as shown in Figure 28. The higher load also contributes to more damages inside Ti_2AlC in metal/Ti_2AlC composites than in fully dense Ti_2AlC.

Figure 27(c) shows that dissipated energy (W_d) increases with applied stress, and the W_d in the composites is higher than that in fully dense Ti_2AlC. Note that although the W_d of the 27%Al alloy/Ti_2AlC is slightly larger than that of the Ti_2AlC at a given stress, the absolute value of energy dissipate by the Ti_2AlC constituent in the composites is approximately 1.5 times that of the pure, fully dense Ti_2AlC at a given volume. This is because only 73% volume of the composite is Ti_2AlC and dissipates energy, whereas all volume in pure, fully dense Ti_2AlC is active in energy dissipation. The W_d is a liner function of the square of stress (σ^2), which agrees with the model proposed by Barsoum *et al.* [19] The reason for the higher dissipated energy in the composites than in fully dense Ti_2AlC alone is twofold. First, the presence of a metallic phase (Al alloy) in the Al alloy/Ti_2AlC composites eases the Ti_2AlC to kink, which makes incipient kinking easier to form and annihilate upon loading-unloading cycles in the composites than in the fully dense Ti_2AlC. This leads to a larger, closed, hysteresis loop (*i.e.* larger W_d) of the composites than the fully dense Ti_2AlC upon cyclic loading. Second, unlike fully dense Ti_2AlC, the Ti_2AlC in the Al alloy/Ti_2AlC composites carries a higher load than the external applied load (Figure 28). The higher load also contributes to the higher W_d of Ti_2AlC in the Al alloy/Ti_2AlC composites than in fully dense Ti_2AlC.

It is invaluable to further prove and quantitatively analyze the load partitioning in the Al alloy/Ti_2AlC composites, because the fact that the Ti_2AlC carries a higher load than the external applied load could be a new mechanism responsible for the higher

energy dissipation in metal/MAX phase composites than the MAX phase alone under cyclic loading. To that end, the rest of the paper develops a quantitative analysis not only to predict the load partitioning in the Al alloy/Ti_2AlC composites, but also to use the calculated load partitioning to predict the W_d. A comparison between the experimental results and prediction is presented and discussed.

6.3.2. Load Partitioning According to the Isostrain Calculation

For the isostrain situation (upper bound for the W_d), the calculated stress for the individual constituents of the composites (*i.e.* the Al alloy and the Ti_2AlC) are plotted a function of the external applied stress σ_c in Figure 28. The stress carried by the Ti_2AlC is higher than the external applied stress σ_c, whereas the stress carried by the Al alloy is lower than the σ_c. This is explained by the fact that the Ti_2AlC is stiffer than the Al alloy, and the stiff phase (Ti_2AlC) carries most of the load according the equation (19). Since the dissipated energy per unit volume per cycle, W_d , is a liner function of the square of stress (σ^2) [19], the calculation suggests that Ti_2AlC carries a higher stress than the σ_c and thus dissipates more energy than at the stress of σ_c. It follows that the load partitioning leads to enhanced energy dissipation of metal/Ti_2AlC composites.

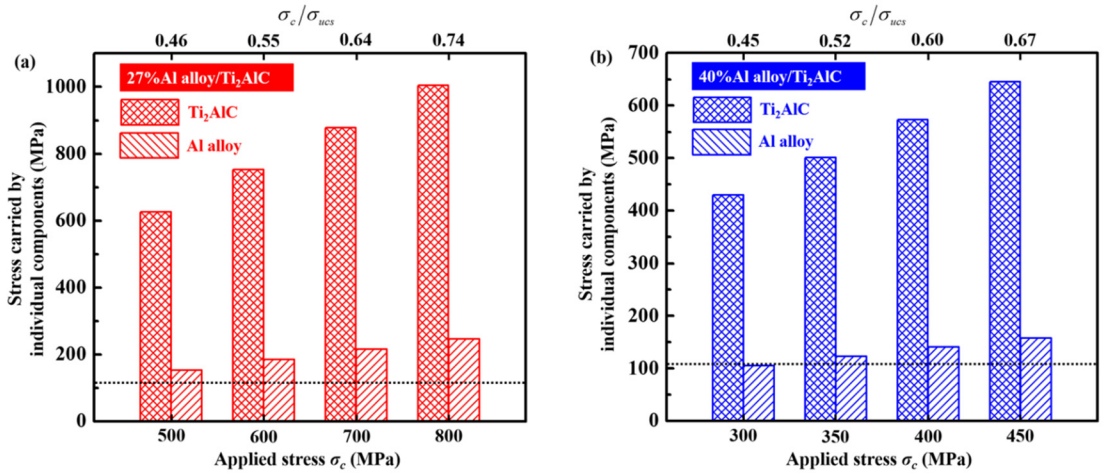

Figure 28. Calculated stresses carried by the individual constituents in (a) 27% Al alloy/Ti_2AlC composites and (b) 40% Al alloy/Ti_2AlC composites as functions of the external applied stress $\sigma_c(MPa)$ and the ratio of σ_c/σ_{ucs}, where $\sigma_{ucs}(MPa)$ is the ultimate compressive strength of the composites. The black, dash lines represent the yield strength $\sigma_{0.002}=110(MPa)$ of the SHT Al alloy.

The present study identifies, for the first time, the contributing role of load partitioning in the energy dissipation of metal/Ti_2AlC composites. This not only expands variables responsible for energy dissipation of KNE solids, but also provides an additional tool to tailor the properties of this kind of materials. Although previous studies have shown enhanced energy dissipation in Mg/Ti_2AlC [23] and Mg/Ti_3SiC_2 [24] composites, load partitioning was not considered as a contributing variable. Before the present work, the enhanced energy dissipation was attributed to either the porosity or the "soft" metallic phase, both of which ease the Ti_2AlC grains to kink. Knowing that load partitioning also enhances energy dissipation, one can tailor the energy dissipation capabilities of the composite material by adjusting the E and volume percent the metallic phase—variables in the equation (21).

6.3.3. Energy Dissipation: Experiments and Calculation

As a quantitatively analysis, W_d is plotted as functions of the square of the external applied stress σ_c^2 and the external applied stress σ_c for both composites: 27%Al alloy/Ti_2AlC (Figure 29(a)) and 40%Al alloy/Ti_2AlC (Figure 29(b)). According to equation (23), the $W_d(\sigma_c)$ value for the upper bound (the isostrain situation) at a stress of σ_c is determined as $W_d^2(\sigma_2)\cdot V_2$ —dissipated energy obtained when Ti_2AlC is cycled to a peak stress of σ_2, where σ_2 is determined according to equation (21) (the isostrain situation) and V_2 is the volume fraction of the Ti_2AlC. The contribution from the Al alloy ($W_d^2(\sigma_1)\cdot V_1$) is neglected, because Al alloy is a linear elastic solid and its stress-strain curves have no hysteresis loops. Similarly, the $W_d(\sigma_c)$ value for the lower bound (the isostress situation) at a stress of σ_c is determined as $W_d^2(\sigma_2)\cdot V_2$ — dissipated energy obtained when Ti_2AlC is cycled to a peak stress of σ_2, where σ_2 is determined according to equation (22) (the isostress situation) and V_2 is the volume fraction of the Ti_2AlC. The experimental W_d values fall between the calculated bounds. This agreement between experimental data and model prediction is another evidence to support that the load partitioning is also a contributing factor to the energy dissipation of metal/Ti_2AlC composites.

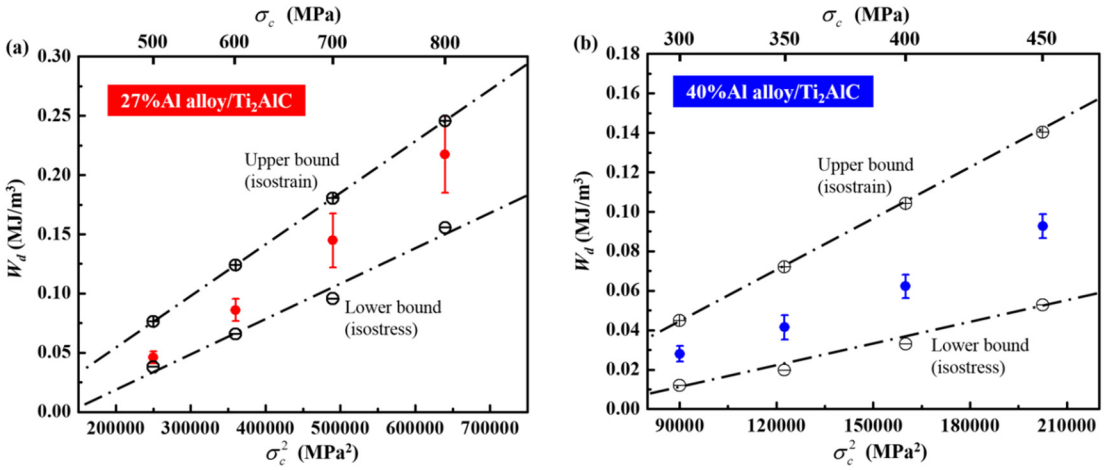

Figure 29. Dissipated energy per unit volume per cycle, W_d, as functions of the square of the external applied stress σ_c^2 and the external applied stress σ_c of (a) 27%Al alloy/Ti2AlC composites and (b) 40%Al alloy/Ti2AlC composites. The bounds calculated according to equation (23) are also plotted in comparison with the experimental results. For the 27%Al alloy/Ti2AlC composites, the $W_d^2(\sigma_2)\cdot V_2$ in equation (23) is from fully dense Ti2AlC, because the density measurements show that the density of the 27%Al alloy/Ti2AlC composites is close to its theoretical density. For the 40%Al alloy/Ti2AlC composites, the $W_d^2(\sigma_2)\cdot V_2$ in equation (23) is from 7% porous Ti2AlC, because the density measurements show that the porosity of the 40%Al alloy/Ti2AlC composites is 7%.

6.3.4. Application of the "Two-Bar" Model

In order to verify the "two-bar" model, the model was applied to literature data of previously reported 50%Mg/Ti2AlC composites [23], and the stresses carried by their individual constituents (*i.e.* σ_1 for Mg and σ_2 for Ti2AlC) were calculated according to the equations (20) and (21). The calculated stresses are plotted in Figure 30(a) as functions of the external applied stress $\sigma_c(MPa)$ and the ratio of σ_c/σ_{ucs}, where $\sigma_{ucs} = 700(MPa)$ [23] is the ultimate compressive strength of the 50%Mg/Ti2AlC composites. Figures 5(b)–(c) show the W_d as a function of the square of the external

applied stress σ_c^2 for the 50%Mg/Ti2AlC composites. The calculated bounds are also plotted in comparison with the experimental data.

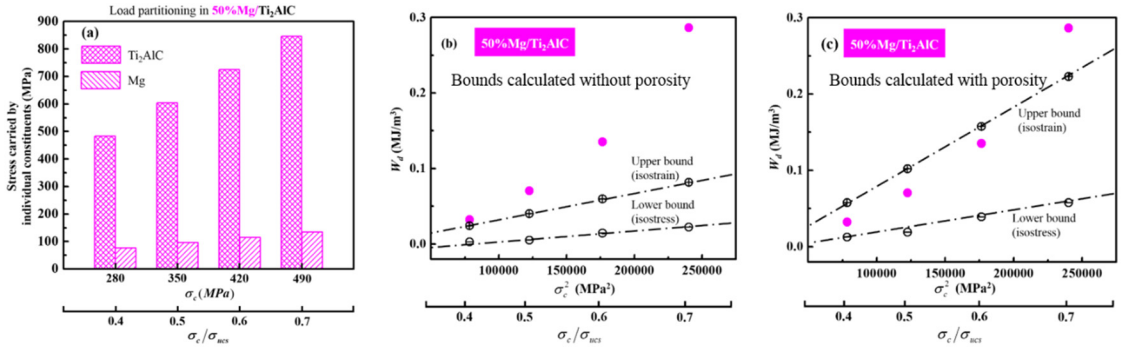

Figure 30. (a) Calculated stresses carried by the individual constituents (*i.e.* Mg and Ti2AlC) of previously reported 50%Mg/Ti2AlC composites [23] as functions of the external applied stress $\sigma_c(MPa)$ and the σ_c/σ_{ucs}, where $\sigma_{ucs} = 700(MPa)$ [23] is the ultimate compressive strength of the composites. (b) and (c) The W_d as a function of the square of the external applied stress σ_c^2 and the σ_c/σ_{ucs} [23]. The bounds were calculated according to equation (23), where $W_d^2(\sigma_2)\cdot V_2$ is the contribution from a fully dense Ti2AlC in (b). The bounds were calculated according to equation (23), where $W_d^2(\sigma_2)\cdot V_2$ is the contribution from a 7% porous Ti2AlC in (c).

Unlike the Al alloy/Ti2AlC composites, the experimental W_d values of the 50%Mg/Ti2AlC composites are higher than the bounds calculated using W_d data from a fully dense Ti2AlC (Figure 30(b)). The discrepancy could be due to the conditions of the individual constituents (Mg and Ti2AlC), because W_d data—the input of calculated bounds—are strong functions of the conditions. Particularly, the $W_d^2(\sigma_2)\cdot V_2$ in equation (23) (the contribution from Ti2AlC) could be larger, if the Ti2AlC were porous rather than fully dense. For example, Figure 30(c) presents the calculated bounds, assuming that the $W_d^2(\sigma_2)\cdot V_2$ in equation (23) is from a 7% porous Ti2AlC instead of a fully

dense Ti_2AlC. Most of the experimental W_d values fall between the new bounds, except for the W_d value at the highest stress. The difference of the calculated bounds between Figure 30(b) and Figure 30(c) suggests that the condition of Ti_2AlC significantly influences the W_d of Ti_2AlC and thus the calculated bounds. Specifically, the higher the porosity of Ti_2AlC, the higher the dissipated energy W_d and the calculated bounds.

When calculating W_d bounds according equation (23), the $W_d^1(\sigma_1)\cdot V_1$ (the contribution from Mg) was neglected and not reflected in Figure 30(b)–(c), because the $W_d^1(\sigma_1)\cdot V_1$ (the contribution from Mg) is less than 5% of the $W_d^2(\sigma_2)\cdot V_2$ (the contribution from Ti_2AlC). This comparison is based on $W_d^1(\sigma_1)$ values of pure Mg from published data by Zhou and Barsoum [23], because the actual $W_d^1(\sigma_1)$ values of the Mg constituent inside the 50%Mg/Ti_2AlC composites are unknown. Note that the Mg constituent in the 50%Mg/Ti_2AlC composites has random crystallography orientations duo to the infiltration process, forming a texture that is similar to the pure Mg in the published work by Zhou and Barsoum [23]. To that end, when comparing to the texture, grain size has a remarkably stronger effect on the $W_d^1(\sigma_1)$ values. The grain size of the pure Mg was 35±20 μm, whereas the grain size of Mg constituent inside the 50%Mg/Ti_2AlC composites is in nanoscale and several orders of magnitude smaller than the values of 35±20 μm. This suggests that the actual $W_d^1(\sigma_1)\cdot V_1$ values should be even smaller and negligible in comparison with $W_d^2(\sigma_2)\cdot V_2$. This is due to the fact that fine-grained Mg dissipate substantially less energy than their coarse-grained counterparts [23].

6.4. Summary and Conclusions

The present study identifies, for the first time, the contributing role of load partitioning in the energy dissipation of metal/MAX phase composites, which not only expands variables responsible for energy dissipation of KNE solids, but also provides an additional tool to tailor the properties of this kind of materials. Before the present work, the enhanced energy dissipation was attributed to either the porosity or the "soft" metallic phase, both of which ease the MAX phase grains to kink. Knowing that load partitioning also enhances energy dissipation, one can design and tailor the energy dissipation capabilities of the metal/MAX phase composite material by adjusting the Young's modulus and volume percent the metallic phase.

CHAPTER VII

FABRICATION AND CHARACTERIZATION OF SHAPE MEMORY ALLOY/TERNARY CARBIDE COMPOSITES *

Previous chapters presented a rapid infiltration method to fabricate metal/ternary carbide composites, *i.e.* aluminum alloy/Ti_2AlC. The other method — powder metallurgy — is presented in the following chapters. Shape memory alloy/ternary carbide composites, *i.e.* NiTi/Ti_2AlC and NiTi/Ti_3SiC_2, are prepared using this method and are systematically characterized. It is clearly shown that SPS is a viable technique to fabricate highly reactive ceramic-metal systems with active components.

7.1. Introduction

Ti_3SiC_2 and Ti_2AlC are the most studied MAX phases [74] and ideal candidate materials for ceramic-metal composites, because they possess an unusual combination of properties typical of either ceramics or metals. They are thermally stable, have high fracture toughness [119], and exhibit low coefficients of thermal expansion and high Young's moduli [96]. These carbides are readily machinable, and they are thermally and electrically conductive [16]. Their nonlinear elasticity allows mechanical energy dissipation during cyclic loading [19]. Although Ti_3SiC_2 has higher compressive, flexural and tensile strengths [15] than Ti_2AlC, the latter has a better oxidation resistance

* Reprinted from Journal of Alloys and Compounds, Vol. 610, Liangfa Hu, Ankush Kothalkar, Gwénaëlle Proust, Ibrahim Karaman, Miladin Radovic, Fabrication and characterization of NiTi/Ti_3SiC_2 and NiTi/Ti_2AlC composites, 635–644, Copyright (2014), with permission from Elsevier.

[19]. MAX phases, including Ti_3SiC_2 and Ti_2AlC, have been used as either reinforcements or matrices in a variety of ceramic-metal composites. Since Cu/Ti_3SiC_2 was proposed as a new electro-friction material [19], a number of MAX phases were used to increase the mechanical strength of Cu without losing thermal and electrical conductivity of the Cu [28-32]. An addition of Ag in Ta_2AlC and Cr_2AlC improved the tribological performances of the carbides, and the resulting composites were proposed as new solid lubricants against Ni-based superalloys and alumina [25, 27]. High-strength MAX phase/magnesium composites with high mechanical damping was fabricated by metal melt infiltration of MAX phase foams [23]. The yield strength of a Ti_3AlC_2/aluminum composite was found to be twice that of aluminum [21]. More recently, the specific strength of an aluminum alloy/Ti_2AlC composite was found to be 3.5 times that of the peak-aged aluminum alloy [22].

SMAs distinguish themselves from other metals by having two characteristics originating from a reversible, martensitic transformation [55]. First, a two-step operation allows recovering the original shape before mechanical deformation; this operation involves deforming the martensite phase of a SMA and then heating that deformed SMA. The behavior is known as the shape memory effect. Second, an isothermal application of mechanical load to the austenite phase of a SMA at sufficiently high temperatures allows it to transform to its martensite phase. Unloading returns it to the original austenite phase, which is known as pseudoelasticity. Nickel-titanium (NiTi), the most studied SMA, has been implemented in various composite materials due to its high ductility, strength, corrosion resistance, and damping capability [56-58].

In the present work, NiTi and MAX phases are combined in interpenetrating composites to obtain higher damage tolerance and mechanical damping than either NiTi or MAX phases alone. We have demonstrated two benefits of combining them in the composites: (i) capability of controlling residual stresses in the composites through their composition, phase morphology, and thermo-mechanical conditioning; (ii) colossal mechanical damping during cyclic loading [49]. Both benefits rely on the percent of transformable NiTi in the composites. To reach optimum damage tolerance and mechanical damping, the fabrication of the composites must preserve as much transformable NiTi as possible.

Reactions between NiTi and MAX phases prohibit application of conventional methods to fabricate the composites. We have shown through a series of inter-diffusion experiments that MAX phases react highly with NiTi at temperatures well below the sintering temperature of MAX phases and form thick and complex reaction layers consisting of multiple phases [48]. A slight variation in the composition of NiTi during fabrication affects its capability to undergo martensitic transformation that is responsible for the mechanical damping. So the challenge for fabricating the composites is to reduce the reactions between NiTi and MAX phases.

Herein, we show that spark plasma sintering (SPS) is a viable technique to fabricate highly reactive SMA/MAX phase composites with active (shape memory) components. We study phase transformation behavior of the composites to evaluate the percent of transformable NiTi. We optimize starting materials and processing conditions

to fabricate fully-dense composites with a maximum percent of transformable NiTi. We also propose reaction mechanisms between NiTi and Ti_3SiC_2 or Ti_2AlC during SPS.

7.2. Experimental Details

Ti_2AlC and Ti_3SiC_2 powders (MAXthal312, Sandvik, Sweden) with particle size in 45–90 μm range and NiTi prealloyed powder (Special Metals, New Hartford, NY; gas atomized from the alloy ingot with the nominal composition of $Ni_{50}Ti_{50}$) with particle size in 88–105 μm range were used. Figure 31 shows Field Emission Scanning Electron Microscopy (FE-SEM) images of these powders. Ti_2AlC and Ti_3SiC_2 particles have irregular shapes and rough surfaces (Figure 31(a) and (b)), while NiTi particles are spherical in shape with smooth surfaces (Figure 31(c)). The insets of Figure 31(a) and (b) illustrate the nanolaminated structure of Ti_2AlC and Ti_3SiC_2.

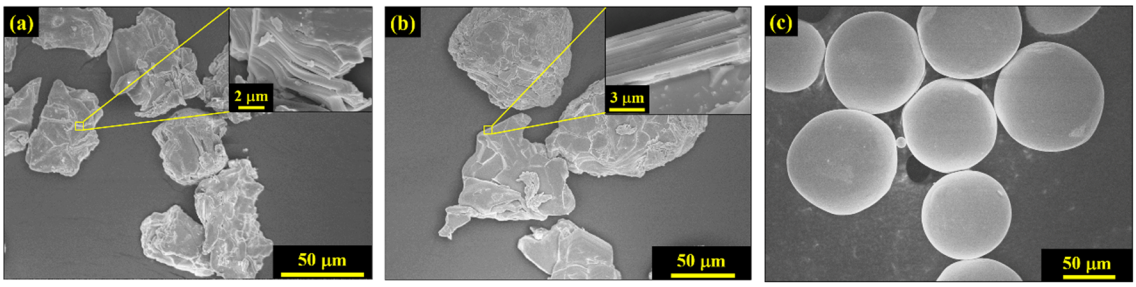

Figure 31. FE-SEM images of (a) the Ti_2AlC powder, (b) the Ti_3SiC_2 powder, and (c) the NiTi powder. The insets in (a) and (b) illustrate the nanolaminated structure of Ti_2AlC and Ti_3SiC_2, respectively.

NiTi/Ti_2AlC and NiTi/Ti_3SiC_2 powder mixtures, each with a 50/50 volume ratio (that corresponds to 61 wt% and 59 wt% of NiTi, respectively, in NiTi/Ti_2AlC and

NiTi/Ti_3SiC_2 powder mixtures), were mixed for 1 hour by ball milling. No balls were used during milling to avoid contamination, and the rotation speed was 300 rmp. The powder mixtures were poured into a graphite die (20 mm in diameter) and processed in SPS (25-10, GT Advanced Technologies, CA) in 1233–1373 K under 100–300 MPa sintering pressure for 3–30 minutes. The processing conditions were selected for two reasons: (i) temperatures lower than 1233 K and soaking time shorter than 3 minutes result in low density and are not preferable; (ii) temperatures higher than 1373 K and soaking time longer than 30 minutes result in total reaction. Fully-dense Ti_2AlC samples were normally obtained at higher temperatures using SPS: 1523 K under 20 MPa for 5 min [131] or 1473 K under 30 MPa for 8 min [72]. However, NiTi melts at such high temperatures, leading to catastrophic reactions [59]. The chamber was evacuated and held at 10^{-4} Pa for 10 minutes before heating. The heating rate was 200 K/min and the whole sintering process was conducted under a flowing, ultra-high-purity argon atmosphere. A high dc current was applied, increasing from 0 to 1450–1620 A in 4 min and then stabilized at 1120–1330 A for soaking. The pulse cycle was 10 ms on and 10 ms off. Graphite foils were applied between the powder mixtures and graphite die. Since the highest pressure for graphite die is 100 MPa, silicon carbide (SiC) die (20 mm in diameter) was used for higher sintering pressures, *i.e.* 200 MPa and 300 MPa. The as-fabricated sample is approximately 19.6 mm in diameter and 6 mm in thickness.

The temperature was measured in a drilled hole of the bottom graphite punch, which was immediately below the surface that was in contact with the sample. The temperature was calibrated by measuring the temperature at which bulk, high-purity

copper melts (results not shown here). The melting point of copper is compared to the temperature at which the position of the upper piston sharply changes from thermal expansion to shrinkage as a result of melting, and the latter is 13 K below the former. The actual temperature is thus calibrated as 13 K above the thermocouple reading.

The density was determined by alcohol immersion method based on Archimedes' principle, as specified in ASTM C20-00 [122]. The theoretical density values of 4.11 g/cm^3 [74], 4.52 g/cm^3 [74], and 6.45 g/cm^3 [75] for fully-dense Ti_2AlC, Ti_3SiC_2, and NiTi were used to calculate the density of composites utilizing the rule of mixture (ROM) and assuming that the effect of the eventual reaction phases on the density is negligible. The relative density is thus the measured density value divided by the ROM values, *i.e.* 5.28 g/cm^3 for the NiTi/Ti_2AlC and 5.48 g/cm^3 for the NiTi/Ti_3SiC_2. Three samples were used to determine the average value and standard deviation of density.

The microstructure, composition, and distribution of phases in the interfacial reaction layers were characterized using a combination of a FE-SEM (JSM-7500F, JEOL, Tokyo, Japan), equipped with Energy Dispersive Spectroscopy (EDS), and another FE-SEM (Zeiss Ultra Plus, Carl Zeiss, Oberkochen, Germany) equipped with an EDS and Electron Backscatter Diffraction (EBSD). Both spot and line scans of EDS were utilized for quantitative analysis of interface chemistry. The accelerating voltage and emission current were 15 kV and 20 mA, respectively. The durations of spot and line scans of EDS were 60 seconds and 15 minutes per spectrum, respectively. Interface thickness, *i.e.* the total thickness of the interfacial reaction layers, was measured and averaged from SEM images at two randomly-selected locations on each sample (five

values per image). The EBSD scans were run with an accelerating voltage of 20 kV and an aperture size of 60 or 120 μm. Large-area scans have a step size of 0.3 μm, while the small-area scans in the interfacial area have a step size of 0.03 μm.

The phase composition of starting powders and composites was determined using an X-ray diffractometer (XRD, D8 Discover, Bruker, WI, USA) with Cu $K\alpha$ radiation (wavelength = 1.542 Å) at 40 kV and 30 mA. The two theta range was 20-80 ^{o} with a step size of 0.04 ^{o} and a step time of 1.5 s. The results were analyzed utilizing both Joint Committee on Powder Diffraction Standards (JCPDS) and Inorganic Crystal Structure Database (ICSD).

Differential scanning calorimetry (DSC, Model Q20, TA Instruments, DE) was carried out on 20–80 mg specimens from the composites or the NiTi powder in a flowing nitrogen atmosphere. The heating and cooling cycles are in 213–423 K temperature range with heating and cooling rates of 10 K/min. Each run continuously tracked 3–10 cycles. Transformation temperatures were determined from the peaks observed in the second cycle using the slope line extension method [76]. The enthalpy of phase transformation was calculated from the area under the transformation peaks. Weight percent of transformable NiTi was calculated according to equation (1).

Table 11 lists starting powder, sintering temperature, soaking time, relative density, interface thickness, percent of transformable NiTi, and phase transformation temperatures of all composites. Each sample is labeled as X-Y-Z where X is A for

Table 11. Starting powder, sintering temperature, soaking time, relative density, interface thickness, percent of transformable NiTi, and phase transformation temperature of all composites.

Group	Sample	Materials				Processing conditions			Properties			
		MAX phase	Particle size (μm)	Shape memory alloy	Particle size (μm)	Sintering temperature (K)		Soaking time (min)	Relative density (%)	Interface thickness (μm)	Percent of transformable phase $W_{trans.}$ (wt. %)*	Phase transformation temperature M_s (K)
						Thermocouple reading	Calibrated					
A	A-1233-8	Ti_2AlC	45–90	NiTi	88–105	1233	1246	8	86.1±2.1	2.9±0.6	46.1	343±1.5
	A-1233-20							20	87.7±2.5	5.3±1.7	34.5	339±1.3
	A-1233-30							30	90.5±0.8	6.9±1.3	24.5	343±1.1
	A-1253-10					1253	1266	10	89.4±0.1	6.1±2.8	32.6	343±1.7
	A-1273-3					1273	1286	3	89.5±0.4	6.9±1.6	41.2	343±1.4
	A-1373-5					1373	1386	5	97.3±0.5	N/A	5.6	343±1.6
B	B-1233-8	Ti_3SiC_2				1233	1246	8	83.3±1.1	< 1	60.4	344±1.9
	B-1233-8†								89.1±0.7		60.4	346±1.1
	B-1233-8‡								96.3±1.3		60.3	346±1.5
	B-1233-20							20	83.5±0.8		60.1	347±0.9
	B-1233-30							30	87.8±0.3		53.3	347±0.8
	B-1253-10					1253	1266	10	83.6±1.1		58.3	347±2.0
	B-1273-3					1273	1286	3	82.8±0.9		50.1	347±2.1

* Defined in the equation (1).
† Processed under a 200 MPa sintering pressure.
‡ Processed under a 300 MPa sintering pressure.

NiTi/Ti_2AlC or B for NiTi/Ti_3SiC_2, Y is the sintering temperature in K, and Z is the soaking time in minutes. For example, NiTi/Ti_2AlC composites processed at 1233 K for 8 minutes are labeled as A-1233-8.

7.3. Results and Discussion

7.3.1. SPS Consolidation of SMA/MAX Phase Powder Mixtures

Figure 32(a) shows typical sintering curves (*i.e.* temperature, pressure, and punch displacement as functions of time) of a NiTi/Ti_2AlC powder mixture. A calibration run was carried out to subtract instrument errors from the punch displacement. Four sequential regions are labeled as I, II, III and IV in Figure 32(a). In region I, the powder mixture was loaded from 5 MPa to 100 MPa at room temperature. The loading resulted in a 10 mm displacement, which eliminated some free space among particles and increased particle-to-particle contact area. The latter is crucial for the powder consolidation in the following heating and soaking stages. In region II, heating from room temperature to 773 K took place. A 2 mm displacement indicates thermal expansion. In region III, heating from 773 K to sintering temperature (*i.e.* 1233 K in this case) followed by soaking took place. A 5 mm displacement indicates sintering shrinkage. The shape of the punch displacement curve in region III suggests three stages: stage 1 with slow shrinkage during heating from 773 K to 1233 K; stage 2 with fast shrinkage around 1233 K; and stage 3 with an additional slow shrinkage. In region IV, cooling from 1233 K to room temperature led to a 2.5 mm displacement, which came from contraction.

To better understand the three-stage behavior in region III, the punch displacement curve is plotted against those of the NiTi and Ti_2AlC powders in Figure 32(b). Although Ti_2AlC continued to thermally expand in stage 1, NiTi already started shrinkage around 773 K, resulting in a slow shrinkage in stage 1. Ti_2AlC started densification and creep, and NiTi shrinkage continued and finished in stage 2. The shrinkage from both phases added up and caused a fast shrinkage. In stage 3, the NiTi shrinkage saturated, and no further shrinkage was observed. However, the densification and creep of Ti_2AlC continued, which resulted in the additional slow shrinkage.

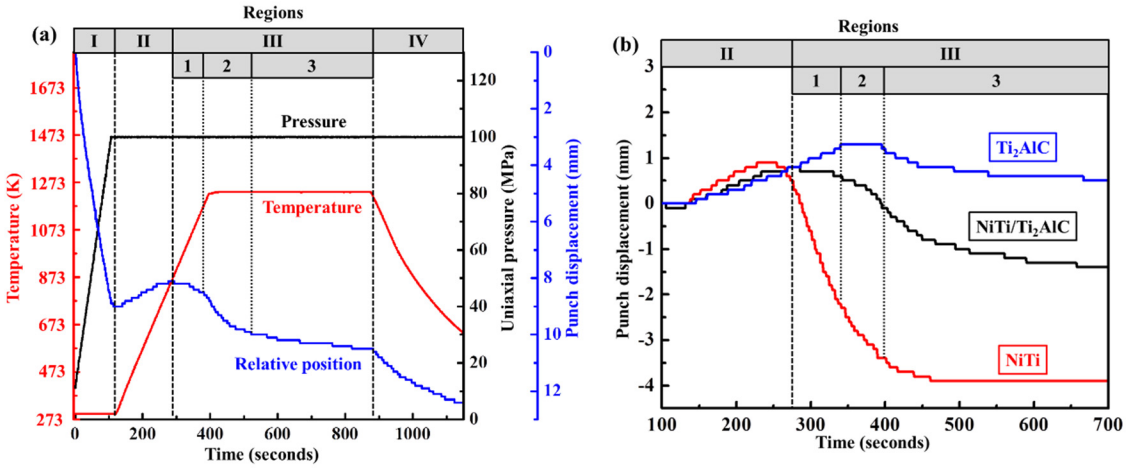

Figure 32. (a) Sintering curves (*i.e.* temperature, sintering pressure, and punch displacement as functions of time) of a NiTi/Ti_2AlC powder mixture. (b) Shrinkage curves (*i.e.* punch displacement as a function of time) of the NiTi powder, the Ti_2AlC powder, and the NiTi/Ti_2AlC powder mixture. All samples were processed at 1233 K under 100 MPa for 8 minutes.

The sintering curves of NiTi/Ti_3SiC_2 powder mixtures were similar to that of NiTi/Ti_2AlC powder mixtures. A comparison of their shrinkage curves (not shown here) indicates that the densification of Ti_3SiC_2 is slower and starts at a higher temperature

than Ti_2AlC. The slower densification suggests that the NiTi/Ti_3SiC_2 composites have lower relative density values than the NiTi/Ti_2AlC composites, which agrees with the measured values (Table 11).

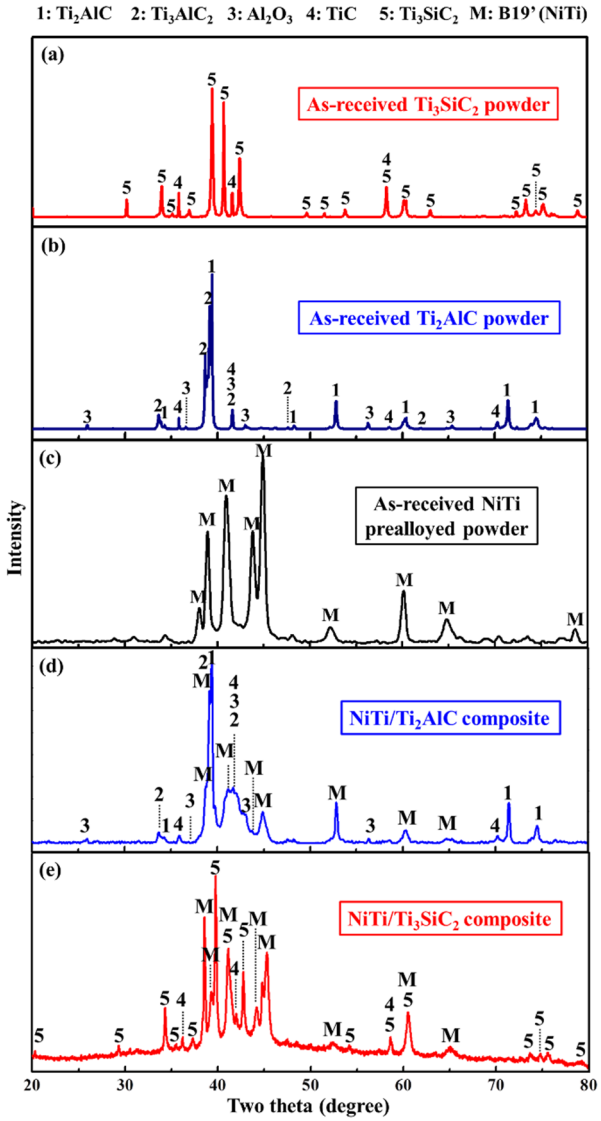

Figure 33. XRD results of (a) the Ti_3SiC_2 powder, (b) the Ti_2AlC powder, (c) the NiTi powder, (d) A-1233-8, and (e) B-1233-8. All data were collected at room temperature. The identification of phases was done according to the JCPDS card number 27-0344 for B19', as well as ICSD collection code 165460 for Ti_2AlC, 153266 for Ti_3AlC_2, 10425 for Al_2O_3, 44494 for TiC, and 86213 for Ti_3SiC_2.

7.3.2. Phase Identification: XRD Results

Figure 33(a) and (b) show that the Ti_3SiC_2 powder has a small amount of TiC as an impurity, while the Ti_2AlC powder has two impurity phases, Al_2O_3 and TiC. TiC is from powder synthesis and a normal impurity phase in both Ti_3SiC_2 and Ti_2AlC. Al_2O_3 most likely comes from oxidation of aluminum during powder synthesis. Figure 33(c) shows that the NiTi powder contains only a martensite (B19') phase.

Typical XRD results of composites are shown in Figure 33(d) and (e) for A-1233-8 and B-1233-8, respectively. Ti_2AlC, Ti_3AlC_2 and B19' (NiTi) are three major phases, and Al_2O_3 and TiC are two impurities in A-1233-8. Ti_3SiC_2, NiTi, and TiC are observed in B-1233-8. All phases identified in the composites were also found in the starting powders, and no new phases were detected. Although some reaction phases were identified by the EDS and EBSD as discussed below, the amounts of them were so small that they were not detectable in XRD due to instrument limitation.

7.3.3. Optimization of Processing Conditions and Starting Materials

Figure 34(a)–(c) show the reaction layers in A-1233-8, A-1233-20, and A-1233-30. The insets show lower magnification micrographs. Light grey regions are NiTi, and dark grey regions are Ti_2AlC. Figure 34(f) shows that the relative density of these three samples increase from 86.1%, to 87.7%, and to 90.5% as the soaking time increases from 8 minutes, to 20 minutes, and to 30 minutes, respectively. It suggests that increasing soaking time at a fixed temperature improves densification. However, longer soaking time causes more reactions. For example, the interface thickness increases from

2.9 μm, to 5.3 μm, and to 6.9 μm as the soaking time increases from 8 minutes, to 20 minutes, and to 30 minutes, respectively. A-1233-8 has two reaction layers, but A-1233-20 and A-1233-30 exhibit three.

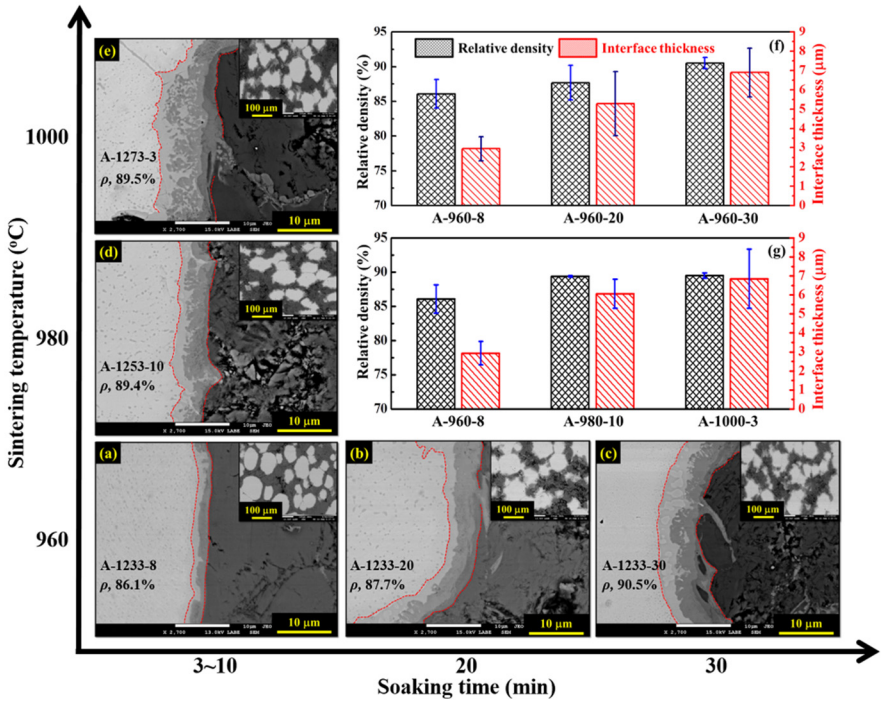

Figure 34. Back scattered SEM images of (a) A-1233-8, (b) A-1233-20, (c) A-1233-30, (d) A-1253-10, and (e) A-1273-3. The insets show lower magnification micrographs. Plots (f) and (g) show the relative density and interface thickness.

Figure 34(a), (d), and (e) show the reaction layers in A-1233-8, A-1253-10, and A-1273-3. Figure 34(g) shows that the relative density of these three samples increases from 86.1%, to 89.4%, and to 89.5%, and the interface thickness increases from 2.9 μm, to 6.1 μm, and to 6.9 μm. Although A-1233-8 and A-1253-10 have two reaction layers, A-1273-3 has three. It suggests that higher sintering temperature improves density at the expense of more reactions.

Although NiTi has various shapes in all five composite samples shown in Figure 34, it has two common features. First, no pores or voids exist in NiTi. Second, no pores or voids exist in the two-phase boundaries. In contrast, Ti_2AlC contains micrometer sized pores and voids at the grain boundaries, which come from the incomplete sintering as discussed above. This suggests that it is the MAX phase that determines the densification of the composites.

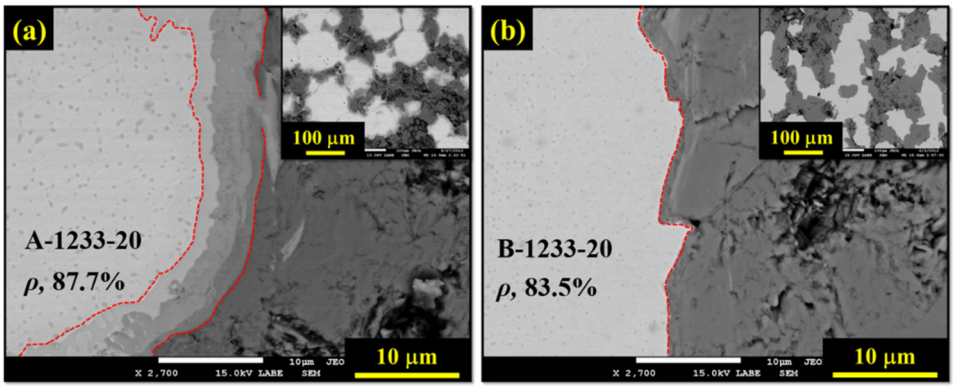

Figure 35. Back scattered SEM images of (a) A-1233-20 and (b) B-1233-20. The insets show low magnification micrographs. Dash lines were added to highlight the interfaces.

To better understand the effect of MAX phases on densification of the composites, control experiments under same conditions with two different powder mixtures, NiTi/Ti_3SiC_2 and NiTi/Ti_2AlC, were carried out. Figure 35 shows back scattered SEM images of A-1233-20 and B-1233-20. The insets show lower magnification micrographs. NiTi (light-grey) in A-1233-20 has round shapes, resembling the shape of initial powder, while NiTi in B-1233-20 has irregular shapes. The relative density of B-1233-20 is lower than that of A-1233-20 because the densification of Ti_3SiC_2 was slower than that of Ti_2AlC as discussed above. B-1233-20

has a thin, sub-micrometer sized interface, but the interface in A-1233-20 is 5.3 μm. The similar conclusions can be drawn when comparing other NiTi/Ti_2AlC and NiTi/Ti_3SiC_2 composites processed at same conditions (Table 11). This suggests that Ti_3SiC_2 is a better choice than Ti_2AlC to reduce the reactions.

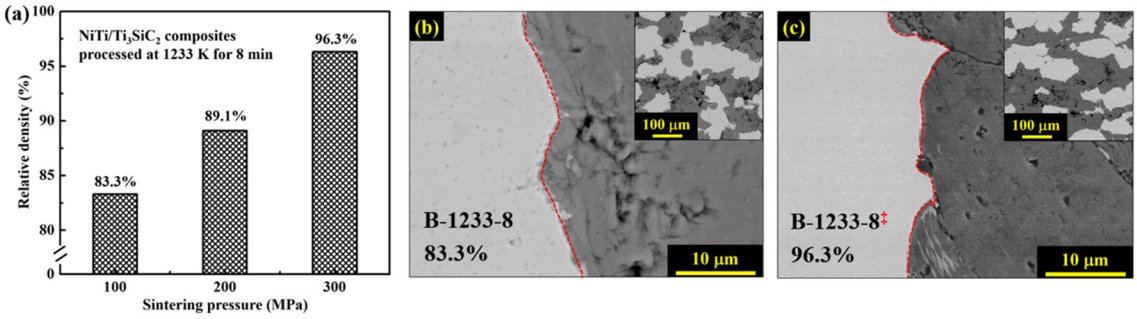

Figure 36. (a) The relative density of NiTi/Ti_3SiC_2 composites as a function of sintering pressure. Back scattered SEM images of (b) A-1233-8 and (c) B-1233-8‡ (sintered at a higher pressure of 300 MPa). The insets show lower magnification micrographs. Dash lines were added to highlight the interfaces.

The comparisons above indicate that B-1233-8 has the least reaction and thus the most transformable NiTi (section 3.5). However, the relative density (83.3%) is low. In order to improve densification, graphite die was replaced with SiC die to reach higher sintering pressures (200 MPa and 300 MPa in this case). Figure 36(a) shows the relative density of NiTi/Ti_3SiC_2 composites as a function of the sintering pressure. The relative density increases from 83.3%, to 89.1%, and to 96.3% as the sintering pressure increases from 100 MPa, to 200 MPa, and to 300 MPa. Figure 36(b) and (c) show that the interfacial layer growth under higher pressure was negligible. It suggests that, unlike sintering temperature and soaking time, sintering pressure is not a sensitive parameter for reactions. In other words, increasing sintering pressure not only improves

densification but also retains transformable NiTi. The latter was confirmed in DSC results (Table 11) where percent of transformable NiTi was calculated in all three cases.

7.3.4. Phase Analysis and Reaction Mechanisms

The results presented up to this point indicate that the reaction between NiTi and Ti_2AlC or Ti_3SiC_2 is a limiting factor in fabricating the composites. Therefore, a combination of FE-SEM, EDS, and EBSD was used to analyze the composition and distribution of phases in the composites and to develop the reaction mechanisms.

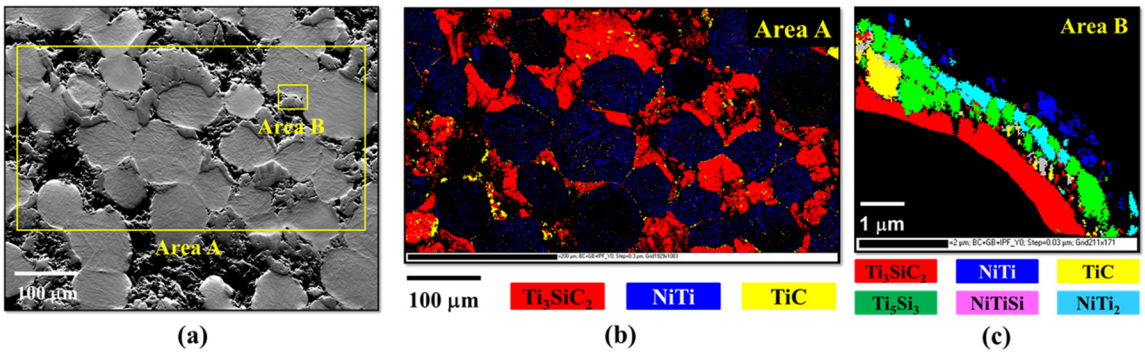

Figure 37. (a) A SEM image of B-1233-8. EBSD phase maps of regions (b) A and (c) B.

Figure 37(a) shows a SEM micrograph of B-1233-8. Two areas, A and B, in this micrograph were selected and analyzed using the EBSD. Figure 37(b) shows a phase map in the larger area A, while Figure 37(c) shows the phase composition and distribution in the interfacial area B. The reaction was mild, resulting in an interfacial layer with a sub-micrometer thickness. In Figure 37(b), Ti_3SiC_2 and NiTi are two major phases in the presence of TiC impurity. Capturing and indexing EBSD patterns in some of NiTi regions were difficult because the martensite phase in NiTi was too small; the

black regions in Figure 37(b) indicate the un-indexed martensite NiTi. The two major phases, Ti_3SiC_2 and NiTi, have interpenetrating networks. The TiC impurity looks like scattered, isolated islands, which could be found mostly in Ti_3SiC_2. The TiC most probaly comes from the Ti_3SiC_2 powder according to the XRD results (Figure 33(a)).

From the NiTi towards the Ti_3SiC_2 over the interfacial layer (from top-right to bottom-left in Figure 37(c)), $NiTi_2$, Ti_5Si_3, TiC, and NiTiSi were identified sequentially. These reaction products have different microstructures: $NiTi_2$ and Ti_5Si_3 are major reaction phases that appear to be more continuous along the interfaces than TiC and NiTiSi. The thickest part of the interface consists of interpenetrating Ti_5Si_3 and $NiTi_2$. TiC has a non-uniform distribution and is again in the shape of isolated, small islands in between Ti_3SiC_2 and Ti_5Si_3. The largest TiC island is surrounded by a Ti_3SiC_2-rich and Ti_5Si_3-rich environment. NiTiSi was detected in a small amount next to Ti_3SiC_2.

The reaction phases and their sequences on the interfacial layer suggest a reaction path between NiTi and Ti_3SiC_2 as follows:

$$2NiTi \rightarrow Ni + NiTi_2 \quad (24)$$

$$Ti_3SiC_2 \rightarrow xSi + Ti_3Si_{1-x}C_2 \quad (25a)$$

$$4Ti_3SiC_2 \rightarrow Si + Ti_5Si_3C_y + 7TiC_{1-x}\ (y=1+7x) \quad (25b)$$

$$5NiTi_2 + 8Si \rightarrow Ti_5Si_3 + 5NiTiSi \quad (26)$$

$$Ti_5Si_3 + 5Ni + 2Si \rightarrow 5NiTiSi \quad (27)$$

According to reaction (24), Ni diffuses out of NiTi towards the interface, leaving behind $NiTi_2$ (Figure 37(c)). The decomposition of Ti_3SiC_2 results in Si (reaction (25)), which agrees with previous results [132] showing that the "A" element (Si in this case) is the

most weakly bonded element and thus diffuses most easily. The composition of $Ti_3Si_{1-x}C_2$ depends on how much Si is lost. An extreme case when Si is totally lost results in titanium carbide; the presence of the latter nearby Ti_3SiC_2 in Figure 37(c) confirms this case. The Si reacts with $NiTi_2$ to form Ti_5Si_3 and NiTiSi (reaction (26)) and further reacts with Ti_5Si_3 and Ni to form NiTiSi (reaction (27)). The NiTiSi is confirmed by the Ni-Ti-Si ternary phase diagram in reference [133]. Depending on how far Si diffuses into the $NiTi_2$ layer and how much the former reacts with latter according to the reaction (28), the amounts of $NiTi_2$ and Ti_5Si_3 are different from location to location.

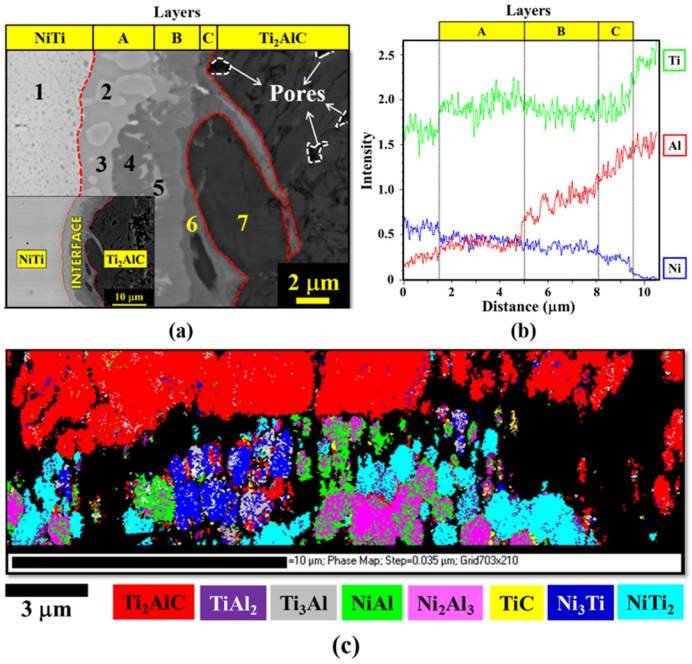

Figure 38. (a) Back scattered SEM images of A-1233-30. The inset shows a lower magnification micrograph. (b) EDS line profiles for Ti, Al, and Ni across the interface. (c) An EBSD phase map at interfacial area.

The reaction mechanisms proposed here are simpler than and different from that proposed earlier by Basu *et al.* [59] for liquid-phase-assited diffusion joining between

bulk Ti_3SiC_2 and NiTi. Unlike that work, such complex intermetallic phases as Ni_3Ti_2, Ni_3Ti_2Si, and Ni_2Ti_3Si were not observed here, most likely because those phases form only at higher temperatures or after longer times. Note that interface thicknesses formed in the composites are smaller than those formed in the joint [59]. The effect of the electrical discharge between Ti_3SiC_2 and NiTi on the reactions cannot be completely excluded at this point.

Figure 38(a) shows SEM micrographs in A-1233-30. Three reaction layers, labeled as A, B and C, could be observed across the interface from the NiTi towards the Ti_2AlC. Although all layers are continuous, both layers A and B are thicker than layer C. The layers A and B consist of a continuous, gray phase, in which an isolated, light phase is embedded. The layer C has only one continuous, gray phase with more homogeneous composition than layers A and B. The layer C grew off the interfacial region at several points along Ti_2AlC grain boundaries. The EDS spot analysis was carried out to determine composition in different phases (Table 12). The EDS line profiles for Ti, Al, and Ni across the interface are shown in Figure 38(b). Note that carbon is not shown in the EDS results because of significant quantifying errors for this specific element. The EDS results are also compared with the EBSD results in Figure 38(c). Phases 1 and 7 are NiTi and Ti_2AlC, respectively. The Ti/Ni ratio in a spot in the NiTi region far away from the interfacial area is 1.0/1.0 (results not shown here), whereas this ratio increases to 1.1/1.0 in the NiTi region close to the interfaces as shown in the spot 1 (Table 12). This

Table 12. EDS spot analysis results of the locations 1–7 in Figure 38(a). EBSD results of the corresponding regions are listed.

Layer	Location	EDS results				EBSD results
		Atomic fraction (%)*			Ni / Ti / Al ratio	Major phases
		Ni	Ti	Al		
NiTi	1	47.7	52.3	0	1.0 / 1.1 / 0.0	NiTi
A	2	35.6	24.6	16.5	2.2 / 1.5 / 1.0	$NiTi_2$, Ni_2Al_3, NiAl, and Ti_3Al
	3	25.4	43	7.6	3.4 / 5.7 / 1.0	
B	4	18.3	37.3	17.8	1.0 / 2.1 / 1.0	$NiTi_2$, $TiAl_2$, Ti_3Al, Ni_2Al_3, NiAl, Ni_3Ti, and un-indexed, decomposed phases†
	5	22.9	41.7	10.2	2.3 / 4.1 / 1.0	
C	6	12.2	36.1	21.4	1.0 / 3.0 / 1.8	Un-indexed, decomposed phases
Ti_2AlC	7	0	43.4	21.3	0.0 / 2.0 / 1.0	Ti_2AlC

* Carbon is not shown in the EDS results because of significant quantifying errors for this specific element.
† Un-indexed, decomposed phases are most likely partially decomposed Ti_2AlC or Ti_3AlC_2 that could not be indexed in EBSD due to severe decomposition and nonstoichiometric chemistry.

indicates that the NiTi close to the interfaces contains a certain amount of $NiTi_2$. The Ti-rich phase resulted from Ni diffusion from the NiTi side towards Ti_2AlC. The Ni diffusion resulted in a decline of Ni concentration in the EDS line profile (Figure 38(b)).

The reaction phases and their sequences on the interfacial layer suggest a reaction path between NiTi and Ti_2AlC as follows:

$$2NiTi \rightarrow Ni + NiTi_2 \quad (28)$$

$$2Ti_2AlC \rightarrow Ti_3AlC_2 + TiAl_x + (1\text{-}x)Al \quad (29a)$$

$$Ti_3AlC_2 \rightarrow 2TiC + Al + Ti \quad (29b)$$

$$Ni + Al \rightarrow NiAl \quad (30a)$$

$$2Ni + 3Al \rightarrow Ni_2Al_3 \quad (30b)$$

$$Al + 2NiAl \rightarrow Ni_2Al_3 \quad (31)$$

$$3Ni + Ti \rightarrow Ni_3Ti \quad (32a)$$

$$2Ni + NiTi \rightarrow Ni_3Ti \quad (32b)$$

According to reaction (28), Ni diffuses out of NiTi into the interfaces, leaving behind $NiTi_2$ (Figure 38(c) and Table 12). This is similar to what occurs on the NiTi side in the $NiTi/Ti_3SiC_2$ composite. The presence of $NiTi_2$ is also confirmed by the EDS line profiles of Ti and Ni (Figure 38(b)), which indicate that the Ti/Ni ratio on the NiTi side immediately next to the reaction layer A is close to 2.0/1.0. Ti_2AlC decomposes into Ti_3AlC_2, $TiAl_x$, and Al according to reaction (29a), and Ti_3AlC_2 decomposes into TiC, Al, and Ti according to reaction (29b); this has been observed in previous studies [134]. Reaction (29b) explains the presence of TiC as shown in the EBSD phase map (Figure 38(c)). Al diffuses towards the interfaces and reacts with Ni to form NiAl and Ni_2Al_3

(reaction (30)). Extra Al could also react with NiAl to form Ni_2Al_3 (reaction (31)). The presence of NiAl and Ni_2Al_3 were observed in the EBSD phase map (Figure 38(c)). However, the high ratio of Ti in spot 3 suggests that the reaction layer A includes Ti-rich phase, most likely $NiTi_2$ and Ti_3Al (the grey phase in Figure 38(c)) that comes from the reactions (28) and (29a), respectively. The transition from the layers A to B is gradual, and the compositions in spot 3 and 5 are close (Figure 38 and Table 12). The layer B also contains Ni_3Ti (Figure 38(c)). Ni_3Ti could be a product of the reaction (32a) or (32b). Based on the Ni/Ti/Al ratio of spot 6, the reaction layer C consists of partially decomposed Ti_2AlC or Ti_3AlC_2 (reaction (29)). Unfortunately, these two Ti-rich phases in this region could not be identified due to decompositions and nonstoichiometric chemistry. However, all phases indexed in EBSD are confirmed in the Al-Ni-Ti phase diagram [135]. Although ternary phases, $TiNi_2Al$ [136], $TiNi_{0.5}Al_{1.5}$ [137], $Ti_6Ni_7Al_{17}$ [138], and $TiNi_{0.25}Al_{2.75}$ [139] may occur in the Al-Ni-Ti system [135], they could not be indexed in EBSD.

Comparing to the NiTi/Ti_3SiC_2 composites, the reaction mechanisms in the NiTi/Ti_2AlC composites are more complex and result in a reaction layer that contains several sub-layers with intermetallic phases. The reactions in the NiTi/Ti_2AlC composites resemble observations in the NiTi/Ti_3SiC_2 composites processed at much higher temperatures, *i.e.* 1373–1573 K [59]; this is not surprising since the activation energy of Ti_3SiC_2 decomposition is larger than that of Ti_2AlC.

Experimental studies [140] have shown that the martensitic transformation temperatures of NiTi strongly depend on composition. One percent change in

composition can result in a change of more than 100 K for the transformation temperatures and in some cases can cause the loss of transformation characteristics and shape memory effects in a desired application temperature range. In the present study, the reactions between NiTi and Ti_3SiC_2 or Ti_2AlC and Ni depletion nearby the reaction interfaces are two major reasons for eventual changes in the composition of NiTi and thus in the transformation capabilities. Therefore, reducing the reactions between NiTi and Ti_3SiC_2 or Ti_2AlC is the key to preserve active shape memory component, *i.e.* transformable NiTi, in the composites during sintering process and to retain shape memory effect in the composites.

The present study suggests two effective means to reduce the reactions. First, the ternary carbide Ti_3SiC_2 is preferable, when compared to Ti_2AlC. At a given sintering temperature and a given soaking time, the reactions between Ti_3SiC_2 and NiTi are slower than those between Ti_2AlC and NiTi because of the slower rate of Si deintercalation from Ti_3SiC_2 (reaction (18)), when compared to that of Al deintercalation from Ti_2AlC (reaction (22a)). Second, the deintercalation of the ternary carbides and the diffusion of the deintercalated elements could be alternatively depressed by lower temperature and shorter time, as shown in the present study by the fast sintering technique - SPS. In fact, the present results suggest that the composition of the NiTi regions that are far away from the interfaces is not altered and is responsible for the transformation and shape memory effect in the composites.

7.3.5. Evaluation of Transformable NiTi

Figure 39(a) shows the DSC curves of the NiTi powder, B-1233-8, and A-1233-8. The NiTi powder shows a characteristic increase in the heat flow during cooling at 337 K that corresponds to a temperature M_s where martensitic phase transformation starts; this increase ends at 318 K that corresponds to a temperature M_f when the transformation finishes. Austenite transforms to martensite at room temperature, which is confirmed by the XRD results (Figure 33(c)). The peaks that correspond to the martensitic phase transformation in the composites are smaller than those in the NiTi powder. The reason is twofold: first, the interface reactions consumed some of the NiTi; second, the amounts of NiTi in the initial powder mixtures are 59 and 61 wt. % (plotted as dash lines in Figure 39(b)), respectively, for the B-1233-8 and the A-1233-8. Although these two composites were processed under the same conditions and had comparable volume of NiTi, the peaks in the B-1233-8 are larger than those in the A-1233-8. The reason lies in the fact that the interface thickness in the B-1233-8 is smaller than that in the A-1233-8, indicating that less NiTi was consumed, and thus more transformable NiTi is preserved in the former.

The enthalpy of phase transformation was calculated from the area under the transformation peaks. The percent of transformable NiTi was then calculated according to equation (1) for two groups of composites: NiTi/Ti_2AlC composites (A-1233-8, A-1233-20, and A-1233-30) and NiTi/Ti_3SiC_2 composite (B-1233-8, B-1233-20, and B-1233-30). The percent of transformable NiTi is plotted as a function of soaking time in Figure 39(b) and listed in Table 11. The percent of transformable NiTi decreases with

increasing soaking time, because longer soaking time allows more reactions which consume more NiTi. At a given soaking time, NiTi/Ti_3SiC_2 composites have a higher percent of transformable NiTi than NiTi/Ti_2AlC composites. This again supports the fact that Ti_3SiC_2 reacts less with NiTi than Ti_2AlC.

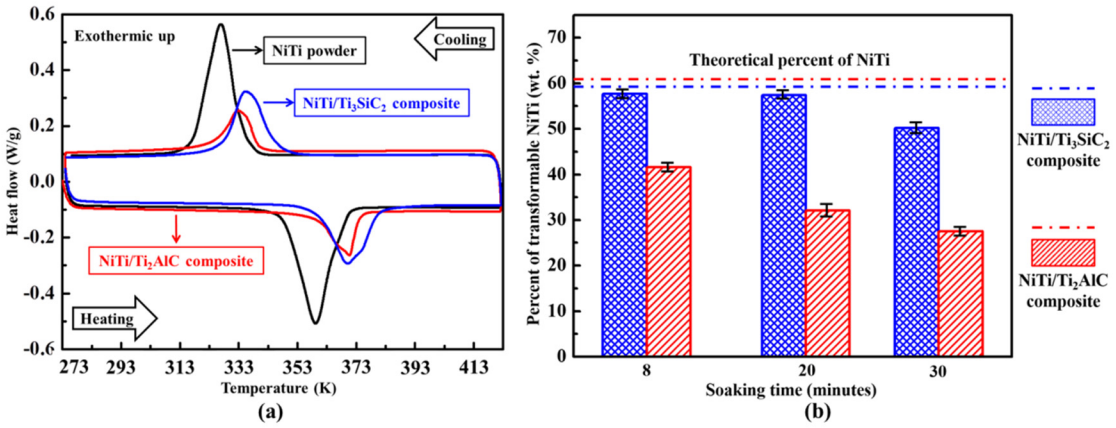

Figure 39. (a) DSC curves of the NiTi powder, B-1233-8, and A-1233-8. Both samples were processed at 1233 K under 100 MPa for 8 minutes. (b) The percent of transformable NiTi (W_{trans}) as a function of soaking time for both the NiTi/Ti_3SiC_2 and NiTi/Ti_2AlC composites.

The percent of transformable NiTi cannot be overestimated because it is a critical parameter for SMA/MAX phase composites with respect to their mechanical responses. Our results on the actuation response of a SMA/MAX phase composite have shown that the stress redistribution associated with martensitic transformation may be used to induce permanent deformations in the MAX phases; these deformations leads to residual stresses. These residual stresses may then be used to take advantage of superior characteristics of the constituents, *e.g.* the improved mechanical response of MAX phases.

7.4. Summary and Conclusions

SMA/MAX phase composites, *i.e.* NiTi/Ti_2AlC and NiTi/Ti_3SiC_2, were fabricated using SPS. Phase transformation behavior of the composites was studied and compared with starting powders to evaluate transformable NiTi in the composites. The effects of starting materials and processing conditions on densification, reaction, and transformable NiTi were studied. The major findings are summarized as follow:

1. 1233 K, 300 MPa, and 8 minutes are optimized processing conditions to produce fully-dense NiTi/Ti_3SiC_2 composites with maximum percent of transformable NiTi.

2. The Ni and the "A" element diffusions, respectively, from NiTi and MAX phases initiate two-phase reactions. The NiTi-Ti_3SiC_2 reactions occurred at a lower rate than the NiTi-Ti_2AlC reactions, so preserved transformable NiTi in the NiTi/Ti_3SiC_2 composites is more than that in the NiTi/Ti_2AlC composites.

3. SPS is a viable technique to fabricate highly reactive ceramic-metal systems with active components.

CHAPTER VIII

TEMPERATURE-DEPENDENT THERMAL PROPERTIES OF A SHAPE MEMORY ALLOY/TERNARY CARBIDE COMPOSITE: EXPERIMENTS AND MODELING *

The previous chapter presented a rapid sintering method (*i.e.* spark plasma sintering) to fabricate SMA/MAX phase composites. In this chapter, thermal properties of a SMA/MAX phase composite, namely NiTi/Ti_3SiC_2, are systematically evaluated as functions of temperature. The thermal diffusivity was measured at both ambient and elevated temperatures up to 1224 K using a laser flash analyzer. The specific heat at constant pressure was measured in 300–600 K range using a differential scanning calorimeter. Thermal conductivity was then calculated from the thermal diffusivity, specific heat, and density in the 300–600 K range. To validate the experimental results, a survey of data on the thermal diffusivity, specific heat, and thermal conductivity of monolithic NiTi and Ti_3SiC_2 was carried out. Finite element modeling was carried out on a micromechanics based representative volume element, in order to predict the thermal conductivity of the NiTi/Ti_3SiC_2 composite. We found an agreement between the experimental and finite element results.

---

* Reprinted from Acta Materialia, Vol. 68, Feifei Cheng, Liangfa Hu, Junuthula N. Reddy, Ibrahim Karaman, Elizabeth Hoffman, Miladin Radovic, Temperature-dependent thermal properties of a shape memory alloy/MAX phase composite: Experiments and modeling, 267–278, Copyright (2014), with permission from Elsevier.

8.1. Introduction

SMA has been implemented in various composites, in order to take advantage of the excellent ductility, high strength, good corrosion resistance, and high damping capability of SMA. Previous efforts have explored the high damping capability of such composites as NiTi/TiC [56], Mg/NiTi [57], and NiTiAl/InSn [58].

A more recent exploration regarding SMA/MAX phase composites was intended for extreme, high-temperature environments. The motivation of combining SMA and MAX phases in the SMA/MAX phase composites is to achieve higher damage tolerance and damping capability. On one hand, different stiffness and thermal expansion of both phases result in not only residual, internal stresses, but also partitioning of externally applied stresses. These could enhance the pseudoelasticity and thus damping capability of the SMA. On the other hand, the shape memory effect of the SMA introduces local, residual stresses, which compressively constrain the MAX phases. The compressive constraint makes the formation and annihilation of kink bands in the MAX phases occur at higher stresses, dissipating more energy and leading to higher damage tolerance and damping capability.

Previous investigations have shown that the reactions between SMA and MAX phases have been well defined in SMA/MAX phase composites, namely NiTi/Ti_2AlC and NiTi/Ti_3SiC_2 [48]. For the first time, the reactivity of NiTi with MAX phases, namely Ti_3SiC_2 and Ti_2AlC, has been studied. Also, a previous investigation has shown a remarkably higher damping capability in a NiTi/Ti_3SiC_2 composite than its pure

constituents, *i.e.* NiTi and Ti_3SiC_2 [49]. In this chapter, we focus on thermal properties of this exciting class of metal/ternary carbide composites.

Micromechanics methods have been used to predict the effective thermal properties of composite materials [141]. For example, Benveniste and Miloh [142] predicted the effective conductivity of a composite media where temperature discontinuity at constituent interfaces reveals thermal boundary resistance. Böhm and Nogales [143] used a Mori-Tanaka scheme to predict the effective thermal conductivity of spherical particle reinforced composites. Dunn and Taya [144] developed an analytical model to predict effective thermal conductivity of multiphase composites reinforced with coated fillers considering the influence of thermal resistance on the filler-matrix interface. All these studies are based on composites with one phase as matrix and a secondary phase as reinforcement. The NiTi/Ti_3SiC_2 composite, however, is an interpenetrating phase composite (IPC), and the presence of pores and reaction interfaces in this composite makes it an even more complicated, four-component (*i.e.* Ti_3SiC_2, NiTi, pore, and interface) system. No computational work has been done on the effective thermal conductivity of an IPC with such complex, microstructural characteristics.

The present study involves measurements of thermal diffusivity and specific heat at constant pressure of a NiTi/Ti_3SiC_2 composite in a range from room temperature to 1224 K, as well as calculations of thermal conductivity using these measured values. This study allows comparison of the NiTi/Ti_3SiC_2 composite against its pure constituents, *i.e.* NiTi and Ti_3SiC_2. To accomplish this, monolithic NiTi and monolithic

Ti_3SiC_2 were prepared for thermal measurements beside the NiTi/Ti_3SiC_2 composite. To validate the measurement results, a survey of data on the thermal diffusivity, specific heat, and thermal conductivity of monolithic NiTi and Ti_3SiC_2 was carried out. In order to predict the thermal conductivity of the composite and compare the prediction with the experimental data, finite element (FE) modeling was also carried out on a micromechanics based representative volume element (RVE).

8.2. Experimental Details

Ti_3SiC_2 powder (MAXthal312, Sandvik, Sweden) with a 45–90 μm particle size range and NiTi prealloyed powder (gas atomized from alloy ingot of nominal composition $Ni_{50}Ti_{50}$) with a 88–105 μm particle size range were used as starting powders. The NiTi powder was acquired from Special Metals, New Hartford, NY. A powder mixture of NiTi/Ti_3SiC_2 with a 50/50 volume ratio was mixed for one hour by ball milling and poured in a graphite die (20 mm in diameter), followed by SPS (25-10, Thermal Technologies, CA) at 960 ^oC under 100 MPa uniaxial pressure for 8 minutes. Detailed optimization of processing conditions is described elsewhere [48]. The heating and cooling rates were 200 ^oC per minute. The whole sintering process was under ultra-high purity, flowing argon, before which the chamber was vacuumed and held at 10^{-6} torr for 10 minutes. Graphite foils were applied between the powder mixture and graphite die before sintering.

Bulk samples of both Ti_3SiC_2 and NiTi were measured as reference materials. A fully-dense Ti_3SiC_2 sample was prepared at 1623 K under 100 MPa uniaxial pressure for

15 minutes. A fully-dense NiTi sample was also acquired from Special Metals, New Hartford, NY for thermal property measurements.

8.2.1. Thermal Diffusivity

The thermal diffusivity, k, was measured at both ambient and elevated temperatures up to 1224 K using a laser flash analyzer (LFA-427, Netzsch Instruments Inc., Germany) as specified in ASTM E1461-01. The specimens were cut into disks with a 10 mm diameter and a 6 mm thickness using electric discharge machining (EDM). Because of their translucency to laser, the specimens were sputter-coated with a graphite layer to ensure complete and uniform absorption of laser pulse. All high temperature thermal diffusivity measurements were conducted in an argon atmosphere. The laser flash method involves heating one side of the specimen with a laser pulse (duration: 0.6 ms; laser voltage: 410 V) and measuring the temperature rise on the other side using an infrared detector. The temperature response was specified in ASTM E1461-01:

$$\Delta T = \Delta T_m \left[1 + 2\sum_{i=1}^{\infty} (-1)^n \exp(\frac{-n^2\pi^2}{H^2} kt) \right] \tag{33}$$

where k and H are thermal diffusivity and thickness of the specimen, respectively; ΔT is the temperature rise of the specimen; ΔT_m is the maximum value of temperature rise; t is the time after pulse heating. The thermal diffusivity is thus determined according to ASTM E1461-01:

$$k = \frac{1.38H^2}{\pi^2 t_{1/2}} \tag{34}$$

where $t_{1/2}$ is the time period during which the temperature rise approaches a half of its maximum value. Each value of thermal diffusivity reported here is the average of measured values from three specimens that were cut from the same sample.

8.2.2. Specific Heat Capacity at Constant Pressure

The specific heat at constant pressure, C_p, was measured in a 300–600 K range using a differential scanning calorimeter (DSC, TA Q20, TA Instruments, DE) as specified in ASTM E1269-11. The specimens were cut into disks with a 4 mm diameter and a 1 mm thickness to fit into the aluminum pan. A synthetic sapphire disk (α-aluminum oxide, TA Instruments, DE) with the same dimensions was used as a reference material. After holding at 213 K for 4 minutes, the specimen was heated up to 653 K at a rate of 20 K/min, and was cooled down to 213 K at the same rate of 20 K/min. Heat flow was measured and recorded as a function of temperature while each specimen continuously tracked 3 cycles of heating and cooling. The DSC apparatus was purged with dry nitrogen at a flow rate of 50 mL/min throughout the experiment. Prior to measuring each specimen, the sapphire disk and the empty aluminum pan were measured separately to calculate the calorimetric sensitivity, E, as specified in ASTM E1269-11:

$$E = \left[\frac{b}{60 \cdot D_{st}}\right]\left[W_{st} \cdot C_p(st)\right] \tag{35}$$

where b (K/min) is the heating rate; D_{st} (mW) is the vertical displacement between heat flow curves of the empty aluminum pan and the sapphire at a given temperature;

W_{st} (mg) is the mass of the sapphire; and $C_p(st)$ $(J/(g \cdot K))$ is the specific heat of the sapphire. Using the calorimetric sensitivity (E), the specific heat capacity of the test specimen is thus determined according to ASTM E1269-11:

$$C_p(s) = \frac{60 \cdot E \cdot D_s}{W_s \cdot b} \tag{36}$$

where $C_p(s)$ $(J/(g \cdot K))$ is the specific heat capacity of the specimen; D_s (mg) is the mass of the specimen; W_s (mW) is the vertical displacement between the heat flow curves of the empty aluminum pan and the specimen at a given temperature. Each value of specific heat is the average of measured values from three specimens that were cut from the same sample.

8.2.3. Thermal Conductivity

Thermal conductivity (λ) was calculated from the measured values of thermal diffusivity (k), density (ρ), and specific heat (C_p):

$$\lambda = k \cdot \rho \cdot C_p \tag{37}$$

The density (ρ) was determined by alcohol immersion method based on Archimedes' principle, as specified in ASTM C20-00. The theoretical density values of 4.52 g/cm^3 [74] and 6.45 g/cm^3 [48] for fully dense Ti_3SiC_2 and NiTi were used to calculate the theoretical ROM density of composite samples. The calculation is based on the assumption that there were no reactions between NiTi and Ti_3SiC_2. The relative density equals the measured density value divided by the ROM density value, *i.e.* 5.48 g/cm^3.

8.3. Results and Discussion

8.3.1. Thermal Diffusivity

Figure 40 shows the measured thermal diffusivity (k) as a function of the measurement temperature during heating of the NiTi/Ti_3SiC_2 composite and its pure constituents, NiTi and Ti_3SiC_2. The thermal diffusivity of Ti_3SiC_2 decreases monotonically with increasing temperature in the 300–1224 K range. The thermal diffusivities of NiTi and NiTi/Ti_3SiC_2 composite, however, decrease and then increase as temperature increases. The martensitic transformation of NiTi accounts for the dramatic change of the thermal diffusivity of monolithic NiTi and the NiTi/Ti_3SiC_2 composite between 340 K and 400 K. Above 400 K, the opposite trends in the change of thermal diffusivity with respect to temperature for the two monolithic phases, *i.e.* increase in NiTi and decrease in Ti_3SiC_2, reveal differences in heat transport of NiTi and Ti_3SiC_2.

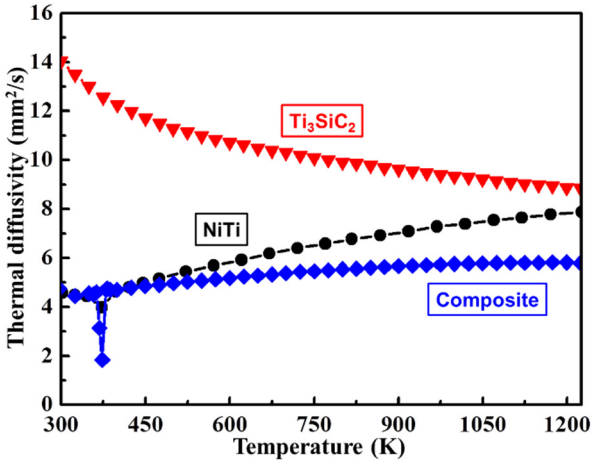

Figure 40. Temperature dependency of the thermal diffusivity upon heating in 300–1224 K range for the NiTi/Ti_3SiC_2 composite. Also included are the corresponding data for monolithic NiTi and Ti_3SiC_2 which were fabricated separately.

The values of thermal diffusivity for the NiTi/Ti_3SiC_2 composite in the 300–1224 K range is much lower than the values predicted by the ROM for two-phase composites. For instance, at room temperature, the ROM value is 9.1 mm^2/K, which is almost two times the measured value (*i.e.* 4.8 mm^2/K). It follows that thermal properties of composite constituents are not merely additive. It also suggests that thermal properties of composites are affected by microstructural features, such as distribution and dispersion of the constituents and discontinuities (*e.g.* pores and grain boundaries). Specifically, a variety of microstructural features (*e.g.* pores and voids, pore/grain boundaries, grain/grain boundaries, and NiTi/Ti_3SiC_2 interfaces) lower the effective thermal diffusivity. The previous work has shown that most of the pores formed in Ti_3SiC_2 are due to the incomplete sintering process, whereas NiTi and the NiTi/Ti_3SiC_2 interfacial area are pore/void free [48]. The pores and voids lower the thermal diffusivity of the Ti_3SiC_2 and thus that of the composite [48]. Moreover, pore/grain boundaries, grain/grain boundaries, and NiTi/Ti_3SiC_2 interfaces provide significant heat scattering to expand the discrepancy between ROM value and measured value of thermal diffusivity.

Similar to NiTi, above 400 K, the thermal diffusivity of the NiTi/Ti_3SiC_2 composite increases with increasing temperature. However, the increase of thermal diffusivity of the composite is smaller than that of NiTi. The opposite trends in the change of thermal diffusivity with respect to temperature for the two pure constituents in the NiTi/Ti_3SiC_2 composite, *i.e.* increase in NiTi and decrease in Ti_3SiC_2, compromise each other and lead to a slower change of thermal diffusivity.

8.3.2. Specific Heat Capacity at Constant Pressure

Figure 41 shows the temperature dependencies of specific heat capacity at constant pressure (C_p) measured upon heating from 300 K to 600 K for the NiTi/Ti_3SiC_2 composite and its pure constituents (*i.e.* NiTi and Ti_3SiC_2). Specific heat at temperatures higher than 600 K was not measured due to the limitation of the instrument. Table 13 presents the specific heat of NiTi and Ti_3SiC_2 in the 300–600 K range in comparison with the literature data. The trend of specific heat with respect to temperature for monolithic Ti_3SiC_2 agrees with literature [145]. The specific heat increases monotonically with increasing temperature. The room temperature value is 0.53 J/g·K, which is close to the reported value of 0.52 J/g·K [48].

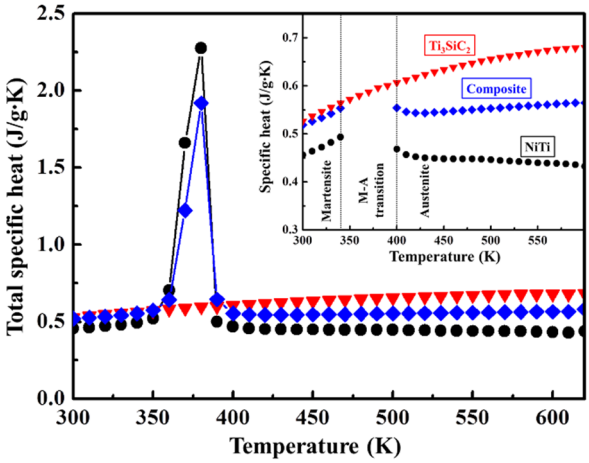

Figure 41. Temperature dependencies of specific heat (C_p) upon heating in 300–600 K range for the NiTi/Ti_3SiC_2 composite and its pure constituents, *i.e.* NiTi and Ti_3SiC_2. Specific heat at higher temperatures than 600 K was not measured due to the instrument limitation. M: martensite, and A: austenite.

Specific heat is known as a sensitive probe for phase transformations involving entropy changes. The data for monolithic NiTi and the NiTi/Ti_3SiC_2 composite between 340 K and 400 K represent not only the heat necessary to change the temperature of NiTi and composite, but also the additional heat generated by the M→A reverse martensitic transformation of NiTi. The same plot without the transformation peaks is shown in the inset of Figure 41 to better compare the magnitude of the specific heat of the NiTi/Ti_3SiC_2 composite and its pure components, *i.e.* NiTi and Ti_3SiC_2. The comparison in Table 13 shows that in 300–600 K range the five sets of experiment data are in reasonable agreement, and the room temperature specific heat for monolithic NiTi in this investigation is 0.46 J/g·K, which agrees well with the corresponding values reported in the literature.

Table 13. The specific heat of NiTi and Ti_3SiC_2 in 300–600 K range in comparison with the literature data.

Temperature, K	NiTi, J/g·K					Ti_3SiC_2, J/g·K	
	This work	Smith *et al.* [a]	Knacke *et al.* [b]	Berman *et al.* [c]	Zanotti *et al.* [d]	This work	Barsoum *et al.* [e]
300	0.46	0.45	0.44	0.45	0.47	0.53	0.52
400	0.47	0.47	0.49	0.47	0.48	0.61	0.59
500	0.45	···	···	···	···	0.65	0.65
600	0.44	0.48	0.53	···	···	0.68	0.67

[a] Reference [146]
[b] Reference [147]
[c] Reference [148]
[d] Reference [149]
[e] Reference [145]

Note that the room temperature specific heat of Ti_3SiC_2 (0.53 J/g·K) is about 15% higher than that of NiTi (0.46 J/g·K). The difference becomes larger and larger as temperature rises, the reason of which is not exactly known at this moment. The specific heat describes the amount of energy a material is able to absorb per unit mass. In the NiTi/Ti_3SiC_2 composite, Ti_3SiC_2 with its high specific heat serves both as a heat sink and as a good thermal disperser. As expected, the specific heat of NiTi/Ti_3SiC_2 composite in 300–600 K range is lower than that of Ti_3SiC_2 but higher than that of NiTi.

8.3.3. Thermal Conductivity

Figure 42 shows the temperature dependencies of thermal conductivity (λ) upon heating from 300 K to 600 K for the NiTi/Ti_3SiC_2 composite and its pure constituents, *i.e.* NiTi and Ti_3SiC_2. Table 14 presents the thermal conductivity of NiTi and Ti_3SiC_2 in 300–600 K range in comparison with the literature data. The room temperature thermal conductivity of Ti_3SiC_2 is 33.4 W/m·K, which is slightly lower than the previously reported value of 36.8 W/m·K [145]. The room temperature thermal conductivity of NiTi is 12.0 W/m·K, which is close to the previously reported values of 11.8 W/m·K [149] and 12.6 W/m·K [150]. The room temperature thermal conductivity of Ti_3SiC_2 is almost three times that of NiTi.

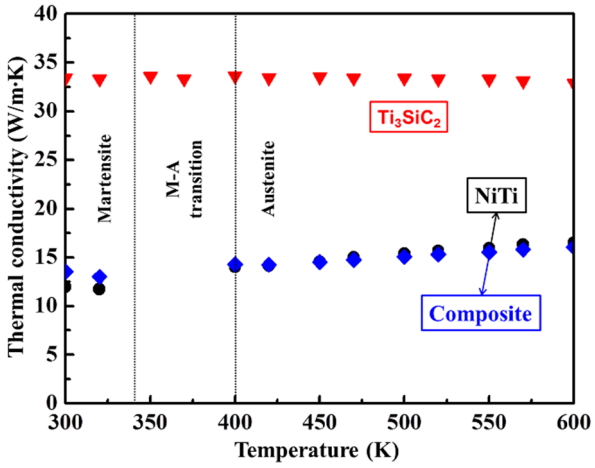

Figure 42. Temperature dependencies of thermal conductivity upon heating in 300–600 K range for the NiTi/Ti_3SiC_2 composite and its pure constituents, *i.e.* NiTi and Ti_3SiC_2.

The electronic contribution to thermal transport follows the Wiedemann-Franz law:

$$\lambda_e = L_0 \sigma T \tag{38}$$

where λ_e is the electronic contribution of the thermal conductivity; L_0 is the *Lorentz* number $2.44 \times 10^{-8} (W \cdot \Omega / K^2)$; σ is electrical conductivity; T is temperature. According to the Wiedemann-Franz law and the fact that the electrical conductivity of Ti_3SiC_2 ($\sigma_{Ti_3SiC_2} = 4.5 \times 10^6 (\Omega^{-1} m^{-1})$ [151]) is about three times that of NiTi ($\sigma_{NiTi} = 1.3 \times 10^6 (\Omega^{-1} m^{-1})$ [152]), the electron contribution to thermal conductivity of Ti_3SiC_2 is about three times that of NiTi. Meanwhile, Barsoum *et al.* [145] pointed out that the electrons dominantly contribute to the room temperature thermal conductivity of Ti_3SiC_2, and Terada *et al.* [153] found out that the carriers of thermal conduction in NiTi is electrons rather than phonons. Therefore, it is expected that the room temperature thermal conductivity of Ti_3SiC_2 is almost three times that of NiTi.

Table 14. Thermal conductivity of NiTi and Ti_3SiC_2 in 300–600 K range in comparison with the literature data.

Temperature, K	NiTi, W/m·K			Ti_3SiC_2, W/m·K	
	This work	Zanotti *et al.*[a]	Chirtoc *et al.*[b]	This work	Barsoum *et al.*[c]
300	12.0	11.8	12.6	33.4	36.8
400	14.0	11.2	15.6	33.6	37.8
500	15.4	12.9	···	33.4	36.1
600	16.5	···	···	32.9	34.0

[a] Reference [149]
[b] Reference [150]
[c] Reference [145]

Similar to thermal diffusivity, the values of thermal conductivity for the $NiTi/Ti_3SiC_2$ composite in 300–600 K range is lower than the ROM values. The reason is that the presence of pores and voids, pore/grain boundaries, grain/grain boundaries and $NiTi/Ti_3SiC_2$ interfaces in the $NiTi/Ti_3SiC_2$ composite lowers the effective thermal conductivity.

8.3.4. Finite Element Modeling

FE modeling was carried out on micromechanics based RVE, in order to predict the effective thermal conductivity for the $NiTi/Ti_3SiC_2$ composite. The phase contents were obtained from experimental data: 16.3 vol.% porosity in Ti_3SiC_2 and 1/1 volume ratio for Ti_3SiC_2 phase and NiTi phase. As mentioned in previous section, the reaction interface layer between Ti_3SiC_2 and NiTi in the composite is an additional feature [48]. Two 3-D RVEs, *i.e.* one considering only porosity and the other taking both porosity and interface into account, were created to investigate the influence of interfaces on effective thermal conductivity.

Porosity with a volume percent of 16% was observed in the Ti_3SiC_2 phase due to incomplete sintering at 960 ^oC, which is well below the sintering temperature of Ti_3SiC_2 but close to the melting temperature of NiTi [48]. Porosity is located within Ti_3SiC_2 phase, while NiTi and the two-phase interface are pore-free, as shown in Figure 43(a). A lot of these pores are interconnected according to the morphology observations. In order to realistically reflect the microstructure of the NiTi/Ti_3SiC_2 composite, pores located within Ti_3SiC_2 phase were explicitly included in the 3-D RVEs, in spite the difficulties in creating such complex geometries and generating mesh in the corresponding FE models. The following numerical analysis is based on the assumption that the pores are filled with air.

Interfaces between Ti_3SiC_2 and NiTi are an additional microstructural feature of the NiTi/Ti_3SiC_2 composite. The thickness of the interface layer is about one micron (Figure 43(b)), and thus 1 μm is assumed as the thickness of all interface layers throughout this composite [48]. Electron backscatter diffraction (EBSD) was used to identify the phase composition in the interface layer, and $NiTi_2$, TiC, and Ti_5Si_3 were found as the main phases [48]. These new phases in the interface layer are assumed to be perfectly bounded with the adjoining Ti_3SiC_2 and NiTi phases. In fact, heat scattering at constituent interfaces due to the differences in vibration properties of dissimilar materials is known as interfacial thermal resistance (or Kapitza resistance) [154]. The interface layer plays an important role in heat transport in the NiTi/Ti_3SiC_2 composite because of the complex phase boundaries formed in interface layer. Therefore, the

influence of interface layer, besides porosity, on the effective thermal conductivity of the NiTi/Ti_3SiC_2 composite was investigated.

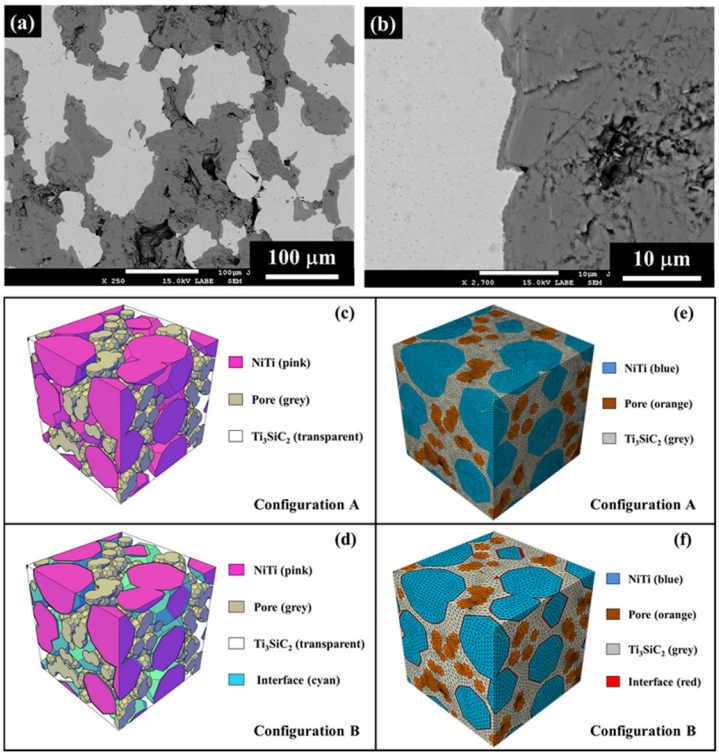

Figure 43. Back scattered SEM images showing (a) phase distribution and morphology and (b) interface. 3-D RVEs of the NiTi/Ti_3SiC_2 composite: (c) in configuration A, grey represents pore, pink NiTi, and transparent Ti_3SiC_2; (d) in configuration B, grey represents pore, pink NiTi, transparent Ti_3SiC_2, and cyan interface; (e) FE meshes on the configuration A RVE; and (f) FE meshes on the configuration B RVE.

Two 3-D RVEs (*i.e.* configurations A and B) are generated based on the microstructural features of the composites. In addition to the two constitutive phases, the configuration A considers only porosity, whereas the configuration B considers both porosity and interfaces, as shown in Figure 43(c) and (d), respectively. The generation of 3-D RVE for configuration A consists of two steps: (i) NiTi particles are randomly placed inside a cube, and rest of the cube is Ti_3SiC_2 with pores; (ii) the pores are

randomly located within the Ti_3SiC_2. The random distributions of NiTi particles and pores in steps (i) and (ii) were achieved by adjusting the distance among the centroids of the NiTi particles and pores. Meanwhile, the desired volume percents of these two phases were achieved by varying the number of particles/pores. For configuration B, a third step was applied to create the interfacial layer. This additional step involves carving out of one or both of NiTi and Ti_3SiC_2 phases along the surface contour. The volume percent of the interface phase were controlled by adjusting the thickness of the interfacial layer. The dimensions of both 3-D RVEs are 200μm × 200 μm × 200 μm. This size is large enough to include all microstructural features (*i.e.* Ti_3SiC_2, NiTi, pores, and interfacial layer), such that the RVE represents local continuum properties of the given composite.

Simplified geometries (*e.g.* limited number of spherical particles and 3-D crosses) have been used to represent the microstructure of IPCs. However, the 3-D crosses cannot reflect the shape of the particle, because the actual cross section of the NiTi particles in the composite is not a perfect circle in 2-D. Therefore, a truncated icosahedron instead of a sphere was adopted to represent the NiTi particles, in order to reflect the irregularity of the outer surface of the interconnected particles. Another advantage of using truncated icosahedrons is that they greatly reduce the element number in the mesh for FE model. The reason is that when we use a perfect spherical shape, there are a lot of tiny segments of curved surface existing due to the connectivity of the particles. It leads to much denser mesh comparing to the truncated icosahedron shape with only flat surfaces which is easier to mesh. Since it is difficult to describe the

size of a truncated icosahedron, the radiuses of the corresponding circumscribed spheres of the truncated icosahedron are used to represent the size of the NiTi particle and voids. And two different sizes for NiTi particles and one size for voids are used in creating 3-D RVEs. The sizes of NiTi particles are 50 μm and 40 μm in radius, whereas the radius of the pores is 12 μm. Each RVE consists of around 33 NiTi particles and 268 pores. It is assumed that the all the consistent phases in the NiTi/Ti_3SiC_2 composite are perfectly bonded. Table 15 lists the volume percent of each phase that are calculated from the two configurations of 3-D RVEs.

Table 15. Volume percent of constituents (*i.e.* Ti_3SiC_2, NiTi, pore, and interfacial layer) in the NiTi/Ti_3SiC_2 composites.

Component	Volume percent, %	
	Configuration A	Configuration B
Ti_3SiC_2	40.5	40.5
NiTi	43.2	40.5
Pore	16.3	16.3
Interface	0.0	2.7

Due to the complex geometry of the 3-D RVEs, they were represented with a mesh with diffusive ten-node quadratic tetrahedral elements in the commercial software ABAQUS. This software is geometrically versatile and convenient to automatically mesh a complex shape. Figure 43(e) and (f) show the meshes for the two RVE configurations. The mesh for configuration A contains 633,718 elements, whereas the one for configuration B contains 452,552 elements.

Temperature gradient boundary conditions were applied along *x, y*, and *z* directions to obtain the effective thermal conductivity in the corresponding directions.

However, it is difficult to include the interfaces into the FE models, because the effective thermal conductivity of interfaces is unknown and difficult to determine experimentally.

One way to gain insight into the effective thermal conductivity of interfaces is to solve an inverse problem: given the best fitting of thermal conductivity values for composite between experimental measurements and FE modelling results, the values used in the modelling for the effective thermal conductivity of interfaces are the predicted values. The prediction was then validated by a bilayer sample through a three-step process: i) make a bilayer sample which contains an interfacial layer with comparable composition and thickness in comparison to the composite; ii) measure the thermal conductivity of the bilayer sample; iii) calculate the effective thermal conductivity of interfaces in the bilayer sample using FE modelling. For simplicity, the interfaces in configuration B were treated as one layer between two phases. The validation of predicted effective thermal conductivity of interfaces is discussed below.

A steady state heat transfer problem was solved to obtain the effective thermal conductivity of the composite. According to the Fourier's law, the effective thermal conductivity is calculated by dividing the heat flux by the corresponding temperature gradient. Experimental results of temperature-dependent thermal conductivities for Ti_3SiC_2 and NiTi (Figure 42) are used as input data for the FE modeling. The thermal conductivity in 340–400 K range was not measured due to the M-A inverse martensitic transformation of NiTi.

8.3.5. Thermal Conductivity: Experiments and Modeling

The simulated effective thermal conductivities of the composite in different directions for the two configurations (*i.e.* configuration A considering only porosity and configuration B considering both porosity and interfaces) are listed in Table 16. It is shown that for configuration A, the maximum difference among λ_x, λ_y, and λ_z for various temperatures is 1.08%, while the corresponding value for configuration B is 0.76%. It suggests that for both configurations, the effective thermal conductivities are approximately isotropic, *i.e.* thermal conductivity being independent of temperature gradient direction. In other words, for the steady state heat transfer problem, the two RVEs achieve approximate isotropy, and furthermore they are statistically homogeneous and can represent the local continuum properties of the NiTi/Ti_3SiC_2 composite.

Table 16. FE results of temperature-dependent thermal conductivity along different temperature-gradient directions, *i.e.* *x*, *y*, and *z*.

Temperature, K	Thermal conductivity, W/m·K							
	Configuration A				Configuration B			
	λ_x	λ_y	λ_z	Standard deviation	λ_x	λ_y	λ_z	Standard deviation
300	16.17	16.11	16.26	0.08	13.83	13.84	13.93	0.06
320	16.03	15.97	16.12	0.08	13.96	13.97	14.06	0.06
450	17.46	17.37	17.54	0.09	15.69	15.66	15.78	0.06
500	17.8	17.71	17.89	0.09	16.12	16.08	16.21	0.07
550	18.04	17.93	18.12	0.10	16.44	16.39	16.53	0.07
600	18.15	18.04	18.23	0.10	16.63	16.58	16.72	0.07

Figure 44 shows the comparison between simulation with experimental results for the two configurations, where the simulation results are the average of λ_x, λ_y, and λ_z.

For configuration A, the simulation overestimates the effective thermal conductivity by 9.2–19.1% as compared to the measured data. The discrepancy between the measured data and the modeling predictions indicates that the presence of interfaces, besides porosity, plays a significant role in thermal transport. In the configuration B, an agreement between the simulation and experimental results was achieved, assuming values of 0.3–1.0 W/m·K for effective thermal conductivity of interface layer in 300–600 K range. The difference between these two sets of data is in 0.04–0.6% range, which is much lower than the corresponding difference in the case where only porosity is considered.

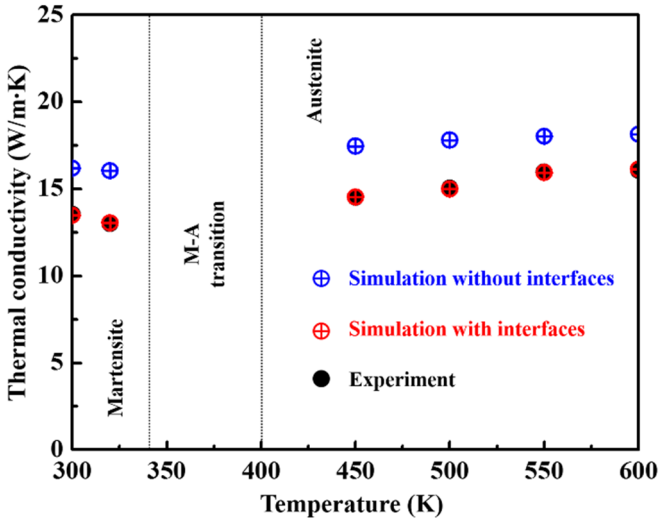

Figure 44. Temperature-dependent thermal conductivity of the NiTi/Ti_3SiC_2 composite: comparison between experiment and simulation results. Simulations results based on both configuration A and B are shown.

8.3.6. Validation of Predicted Thermal Conductivity of Interfaces

To validate the predicted values of the effective thermal conductivity of interfaces, a bilayer sample was prepared by hot pressing two discs, one NiTi and the other Ti_3SiC_2, in the SPS system. The processing conditions were 1273 K, 40 MPa, 30 minutes. Detailed processing conditions are described elsewhere [48]. The composition and thickness of the interfaces formed in the bilayer sample are similar to those formed in the composite. After measuring the thermal conductivity of the bilayer sample, the effective thermal conductivity of the interfaces was calculate using a 2-D axisymmetric FE model created in ABAQUS. Eight-node quadratic axisymmetric heat transfer quadrilateral elements were used in the modeling. Temperature gradient boundary conditions were applied along the thickness direction in the modeling. The calculated values for the interfaces in bilayer sample are plotted against the predicted values of interfaces in composites in Figure 45, as well as the measured thermal conductivity of the composite.

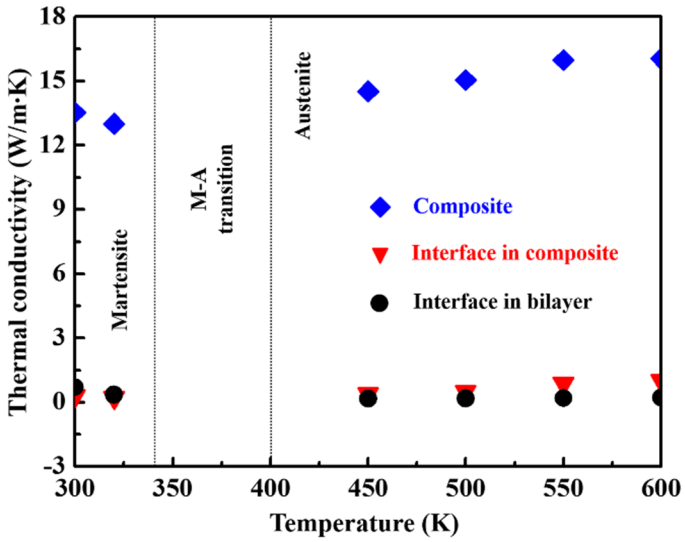

Figure 45. Temperature dependencies of thermal conductivity upon heating in 300–600 K range for the NiTi/Ti_3SiC_2 composite (measured), interface in the composite (FE predicted), and interface in the NiTi-Ti_3SiC_2 bilayer (FE predicted).

Figure 45shows that the effective thermal conductivity of interfaces in the bilayer sample agrees with those predicted for the interfaces in the composite, indicating that predicted effective thermal conductivity of interfaces in composite is valid. Note that the thermal conductivity of interfaces is about one order of magnitude lower than that of composite. The reasons are not clear at this point, but one possible reason lies in interfacial (Kapitza) thermal resistance [155], *i.e.* heat scattering at constituent interfaces due to the differences in vibration properties of dissimilar materials. The dissimilarity could be observed in interfacial microstructures where several interfacial layers with significantly different stiffness formed between NiTi and Ti_3SiC_2.

8.4. Summary and Conclusions

A SMA/MAX phase composite, *i.e.* NiTi/Ti_3SiC_2 composite, was fabricated using SPS. The thermal diffusivity, specific heat, and thermal conductivity were measured for the composite and its constituents, *i.e.* Ti_3SiC_2 and NiTi. The measured data were validated and compared with the literature data. FE modeling was carried out on micromechanics based RVEs, in order to predict the thermal conductivity of the NiTi/Ti_3SiC_2 composite. The modeling results were compared to measured results. The major findings are summarized and listed below.

1. The values of thermal diffusivity and thermal conductivity for the NiTi/Ti_3SiC_2 composite are lower than the ROM values due to the presence of pores and voids, pore/grain boundaries, grain/grain boundaries, and NiTi/Ti_3SiC_2 interfaces.

2. The specific heat of the NiTi/Ti_3SiC_2 composite in 300–600 K range is lower than that of Ti_3SiC_2 but higher than that of NiTi. In the composite system, Ti_3SiC_2 with its high specific heat serves as a heat sink and as a good thermal disperser.

3. The interfacial layer has a low thermal conductivity, which lowers the overall heat flux flowing through the composite, especially in the NiTi phase. The low thermal conductivity is due to the formation of new phase boundaries within the interfacial layer. The new phase boundaries result in a thermal interfacial resistance at constituent interfaces.

CHAPTER IX

CONCLUSIONS AND FUTURE DIRECTIONS

The main accomplishment of the dissertation is that I developed a rapid processing method to create 3 new metal/ternary carbide composites. I also demonstrated desired mechanical and thermal response capabilities of the new composites. The hypothesis is that the rapid processing method could provide controlled multi-phase reactions, offer the opportunity for compositional and microstructural control, and realize materials that are metastable or even far from equilibrium. The rapid processing method was developed based on the SPS system, and 3 new composites (*i.e.* NiTi/Ti_2AlC, NiTi/Ti_3SiC_2, and aluminum alloy/Ti_2AlC) were fabricated using this method. The results show that the new rapid processing method was viable to control multi-phase reactions, composition, and microstructure, leading to tailored and sometimes unprecedented properties. Major conclusions could be summarized as follows:

1. Ti_2AlC foams with a wide range of porosity were fabricated using different volume contents of NaCl powders as pore formers. A wide range of pore size was also fabricated using NaCl powders with different particle sizes.
2. The Ti_2AlC foams were used as preforms to fabricate metal/ternary carbide composites, *i.e.* aluminum alloy/Ti_2AlC, using the CAPAI method. More than 97% of the open porosity in the Ti_2AlC foams were infiltrated with the molten aluminum alloy even after a very short processing time. The results

suggest that this method offers an efficient route for producing ceramic-metal composites with customizable structures by controlling the structure of the ceramic preforms.

3. Little reaction was observed in the aluminum alloy-Ti_2AlC system, which suggests that the CAPAI method can be used to process new, reactive ceramic-metal composite systems that could not otherwise be obtained using conventional methods.
4. This method can result in composites with superior properties in comparison with those of the constituents. The specific compressive strength of the AA6061/Ti_2AlC composites is about 10 times higher at room temperature and 14 times higher at 400 ^oC than the specific yield strength of peak-aged AA6061.
5. CAPAI offers an efficient route to manipulate composite structures by controlling the porosity and pore size of ceramic foams. The ability to manipulate structures cannot be overemphasized, because it could enable complex hierarchical designs to mimic natural composites. These designs have generated enormous interest but have yielded few practical advances.
6. The present study identifies, for the first time, the contributing role of load partitioning in the energy dissipation of metal/MAX phase composites, which not only expands variables responsible for energy dissipation of KNE solids, but also provides an additional tool to tailor the properties of this kind of materials.

7. The optimized processing conditions to produce fully-dense NiTi/Ti_3SiC_2 composites with a maximum percent of transformable NiTi are 1233 K, 300 MPa, and 8 minutes.
8. The Ni and the "A" element diffusions from NiTi and MAX phases, respectively, initiate two-phase reactions. The NiTi-Ti_3SiC_2 reactions occurred at a lower rate than the NiTi-Ti_2AlC reactions, so the amount of preserved transformable NiTi in the NiTi/Ti_3SiC_2 composites is higher than that in the NiTi/Ti_2AlC composites.
9. SPS is a viable technique to fabricate highly reactive ceramic-metal systems with active components.
10. The values of thermal diffusivity and thermal conductivity for the NiTi/Ti_3SiC_2 composite are lower than the corresponding ROM values due to the presence of pores and voids, pore/grain boundaries, grain/grain boundaries, and NiTi/Ti_3SiC_2 interfaces.
11. The specific heat of the NiTi/Ti_3SiC_2 composite in the 300–600 K temperature range is lower than that of Ti_3SiC_2 but higher than that of NiTi. In the composite system, Ti_3SiC_2 with its high specific heat serves both as a relative heat sink and a good thermal disperser.
12. The interfacial layer has a low thermal conductivity, which lowers the overall heat flux flowing through the composite, especially in the NiTi phase. The low thermal conductivity is due to the formation of new phase boundaries

within the interfacial layer. The new phase boundaries result in a thermal interfacial resistance at constituent interfaces.

Overall, through systematic studies on fabrication and characterization, metal/ternary carbide composites showed metastable and non-equilibrium compositions and an unprecedented combination of lightweight, strength, ductility, mechanical energy dissipation. This combination is vital to developing energy efficient technology in a variety of fields, such as aerospace, transportation, power generation, and energy conversion. However, the fabrication methods were applied to only 3 composite systems. Therefore, more work is needed to generalize and apply the methods to more composite systems. One such example is that using conventional methods is challenging when fabricating highly reactive systems, and the preliminary results suggest that newly developed methods in the present work hold a promise to solve the problem.

REFERENCES

[1] Barsoum MW. MAX Phases: Properties of Machinable Ternary Carbides and Nitrides. Weinheim, Germany: Wiley-VCH; 2013.

[2] Eklund P, Beckers M, Jansson U, Hogberg H, Hultman L. The $M_{(n+1)}AX_{(n)}$ phases: Materials science and thin-film processing. Thin Solid Films 2010;518:1851-78.

[3] Dahlqvist M, Alling B, Rosen J. Stability trends of MAX phases from first principles. Phys Rev B 2010;81:4.

[4] Nowotny H, Rogl P, Schuster JC. Structural chemistry of complex carbides and related-compounds. J Solid State Chem 1982;44:126-33.

[5] El-Raghy T, Zavaliangos A, Barsoum M, Kalidindi S. Processing and properties of Ti_3SiC_2. Warrendale, PA: Minerals, Metals & Materials Soc; 1996.

[6] Medvedeva NI, Novikov DL, Ivanovsky AL, Kuznetsov MV, Freeman AJ. Electronic properties of Ti_3SiC_2-based solid solutions. Phys Rev B 1998;58:16042-50.

[7] Holm B, Ahuja R, Johansson B. Ab initio calculations of the mechanical properties of Ti_3SiC_2. Appl Phys Lett 2001;79:1450-2.

[8] Hug G, Jaouen M, Barsoum MW. X-ray absorption spectroscopy, EELS, and full-potential augmented plane wave study of the electronic structure of Ti_2AlC, Ti_2AlN, Nb_2AlC, and $(Ti_{0.5}Nb_{0.5})_2AlC$. Phys Rev B 2005;71:12.

[9] Hug G, Fries E. Full-potential electronic structure of Ti_2AlC and Ti_2AlN. Phys Rev B 2002;65:4.

[10] Sun ZM, Zhou YC. Ab initio calculation of titanium silicon carbide. Phys Rev B 1999;60:1441-3.

[11] Zhou YC, Sun ZM. Electronic structure and bonding properties of layered machinable Ti_2AlC and Ti_2AlN ceramics. Phys Rev B 2000;61:12570-3.

[12] Zhou YC, Sun ZM, Wang XH, Chen SQ. Ab initio geometry optimization and ground state properties of layered ternary carbides Ti_3MC_2 (M = Al, Si and Ge). J Phys Condens Matter 2001;13:10001-10.

[13] Sun ZM, Zhou YC. Electronic structure and structural properties of Ti_4AlN_3 investigated by ab initio calculations. J Phys Soc Jpn 2002;71:1313-7.

[14] Holm B, Ahuja R, Li S, Johansson B. Theory of the ternary layered system Ti-Al-N. J Appl Phys 2002;91:9874-7.

[15] Barsoum MW, Radovic M. Elastic and Mechanical Properties of the MAX Phases. In: Clarke DR, Fratzl P, editors. Annual Review of Materials Research, Vol 41. Palo Alto, CA: Annual Reviews; 2011. p. 195-227.

[16] Radovic M, Barsoum MW. MAX phases: Bridging the gap between metals and ceramics. Am Ceram Soc Bull 2013;92:20-7.

[17] Sundberg M, Malmqvist G, Magnusson A, El-Raghy T. Alumina forming high temperature silicides and carbides. Ceram Inter 2004;30:1899-904.

[18] Farber L, Levin I, Barsoum MW. High-resolution transmission electron microscopy study of a low-angle boundary in plastically deformed Ti_3SiC_2. Philos Mag Lett 1999;79:163-70.

[19] Barsoum MW, Zhen T, Kalidindi SR, Radovic M, Murugaiah A. Fully reversible, dislocation-based compressive deformation of Ti_3SiC_2 to 1GPa. Nat Mater 2003;2:107-11.

[20] Radovic M, Barsoum MW, El-Raghy T, Wiederhom SM, Luecke WE. Effect of temperature, strain rate and grain size on the mechanical response of Ti_3SiC_2 in tension. Acta Mater 2002;50:1297-306.

[21] Wang WJ, Gauthier-Brunet V, Bei GP, Laplanche G, Bonneville J, Joulain A, et al. Powder metallurgy processing and compressive properties of Ti_3AlC_2/Al composites. Mater Sci Eng A 2011;530:168-73.

[22] Hu L, Kothalkar A, O'Neil M, Karaman I, Radovic M. Current-activated, pressure-assisted infiltration: A novel, versatile route for producing interpenetrating ceramic–metal composites. Mater Res Lett 2014;2:124-30.

[23] Amini S, Ni CY, Barsoum MW. Processing, microstructural characterization and mechanical properties of a Ti_2AlC/nanocrystalline Mg-matrix composite. Compos Sci Technol 2009;69:414-20.

[24] Amini S, Barsoum MW. On the effect of texture on the mechanical and damping properties of nanocrystalline Mg-matrix composites reinforced with MAX phases. Mater Sci Eng A 2010;527:3707-18.

[25] Gupta S, Filimonov D, Palanisamy T, El-Raghy T, Barsoum MW. Ta_2AlC and Cr_2AlC Ag-based composites - New solid lubricant materials for use over a wide temperature range against Ni-based superalloys and alumina. Wear 2007;262:1479-89.

[26] Gupta S, Filimonov D, Zaitsev V, Palanisamy T, El-Raghy T, Barsoum MW. Study of tribofilms formed during dry sliding of Ta_2AlC/Ag or Cr_2AlC/Ag composites against Ni-based superalloys and Al_2O_3. Wear 2009;267:1490-500.

[27] Gupta S, Barsoum MW. On the tribology of the MAX phases and their composites during dry sliding: A review. Wear 2011;271:1878-94.

[28] Ngai TL, Zheng W, Li YY. Effect of sintering temperature on the preparation of Cu-Ti_3SiC_2 metal matrix composite. Prog Nat Sci 2013;23:70-6.

[29] Peng LM. Fabrication and properties of Ti_3AlC_2 particulates reinforced copper composites. Scripta Mater 2007;56:729-32.

[30] Wu JY, Zhou YC, Wang JY. Tribological behavior of Ti_2SnC particulate reinforced copper matrix composites. Mater Sci Eng A 2006;422:266-71.

[31] Zhou Y, Chen B, Wang X, Yan C. Mechanical properties of Ti_3SiC_2 particulate reinforced copper prepared by hot pressing of copper coated Ti_3SiC_2 and copper powder. Mater Sci Technol 2004;20:661-5.

[32] Zhang J, Wang JY, Zhou YC. Structure stability of Ti_3AlC_2 in Cu and microstructure evolution of Cu-Ti_3AlC_2 composites. Acta Mater 2007;55:4381-90.

[33] Cui B, Zapata-Solvas E, Reece MJ, Wang CA, Lee WE. Microstructure and High-temperature Oxidation Behavior of Ti_3AlC_2/W Composites. J Am Ceram Soc 2013;96:584-91.

[34] Li H, Peng LM, Gong M, He LH, Zhao JH, Zhang YF. Processing and microstructure of Ti_3SiC_2/M(M=Ni or Co) composites. Mater Lett 2005;59:2647-9.

[35] Gu WL, Zhou YC. Reactions between Ti and Ti_3SiC_2 in temperature range of 1273-1573 K. Trans Nonferrous Met Soc China 2006;16:1281-8.

[36] Mabuchi H, Harada K, Tsuda H, Nakayama Y. Fabrication of Ti_2AlC/TiAl composites using combustion reaction process. Iro Ste Inst Jap Int 1991;31:1272-8.

[37] Mabuchi H, Tsuda H, Nakayama Y, Sukedai E. Processing of TiAl-Ti_2AlN composites and their compressive properties. J Mater Res 1992;7:894-900.

[38] Whittenberger JD, Ray R, Farmer SC. Elevated-temperature deformation properties of in-situ carbide particle strengthened Ti-48Al materials. Intermetallics 1994;2:167-78.

[39] Kakitsuji A, Ramkumar J, Kinose J, Mabuchi H, Tsuda H, Morii K. Synthesis of TiAl(Cr)/Ti_2AlC composites by reactive arc-melting. Mater Trans 2002;43:2589-92.

[40] Yeh CL, Shen YG. Formation of TiAl-Ti_2AlC in situ composites by combustion synthesis. Intermetallics 2009;17:169-73.

[41] Mei BC, Miyamoto Y. Investigation of TiAl/Ti_2AlC composites prepared by spark plasma sintering. Mater Chem Phys 2002;75:291-5.

[42] Chen YL, Yan M, Sun YM, Mei BC, Zhu JQ. The phase transformation and microstructure of TiAl/Ti_2AlC composites caused by hot pressing. Ceram Int 2009;35:1807-12.

[43] Shu SL, Qiu F, Jin SB, Lu JB, Jiang QC. Compression properties and work-hardening behavior of Ti_2AlC/TiAl composites fabricated by combustion synthesis and hot press consolidation in the Ti-Al-Nb-C system. Mater Des 2011;32:5061-5.

[44] Shu SL, Qiu F, Xing B, Jin SB, Wang YW, Jiang QC. Study of effect of Mn addition on the mechanical properties of Ti_2AlC/TiAl composites through first principles study and experimental investigation. Intermetallics 2012;28:65-70.

[45] Shu SL, Qiu F, Lu SJ, Jin SB, Jiang QC. Phase transitions and compression properties of Ti_2AlC/TiAl composites fabricated by combustion synthesis reaction. Mater Sci Eng A 2012;539:344-8.

[46] Ramaseshan R, Kakitsuji A, Seshadri SK, Nair NG, Mabuchi H, Tsuda H, et al. Microstructure and some properties of TiAl-Ti_2AlC composites produced by reactive processing. Intermetallics 1999;7:571-7.

[47] Shi XL, Wang M, Zhai WZ, Xu ZS, Zhang QX, Chen Y. Influence of Ti_3SiC_2 content on tribological properties of NiAl matrix self-lubricating composites. Mater Des 2013;45:179-89.

[48] Hu L, Kothalkar A, Proust G, Karaman I, Radovic M. Fabrication and characterization of NiTi/Ti_3SiC_2 and NiTi/Ti_2AlC composites. J Alloys Compd 2014;610:635-44.

[49] Kothalkar A, Benitez R, Hu L, Radovic M, Karaman I. Thermo-mechanical response and damping behavior of shape memory alloy/MAX phase composites. Metall Mater Trans A 2014;45:2646-58.

[50] Cheng F, Hu L, Reddy JN, Karaman I, Hoffman E, Radovic M. Temperature-dependent thermal properties of a shape memory alloy/MAX phase composite: Experiments and modeling. Acta Mater 2014;68:267-78.

[51] Zheng LY, Wang JY, Chen JX, Liu MY, Sun YJ, Zhou YC. Preparation, microstructure, and mechanical properties of Nb_4AlC_3-$Nb_5(Si, Al)_3$ composites. J Am Ceram Soc 2013;96:365-8.

[52] Garcia-Cordovilla C, Louis E, Narciso J. Pressure infiltration of packed ceramic particulates by liquid metals. Acta Mater 1999;47:4461-79.

[53] Liu J, Sinner J, Higginson R, Zhou ZX. Interfacial reactions and wetting in Al-Mg/oxide ceramic interpenetrating composites made by a pressureless infiltration technique. Compos Sci Technol 2012;72:886-93.

[54] Viala JC, Vincent C, Vincent H, Bouix J. Thermodynamic approach of the chemical interaction between Al and TiC. Mater Res Bull 1990;25:457-64.

[55] Ma J, Karaman I, Noebe RD. High temperature shape memory alloys. Int Mater Rev 2010;55:257-315.

[56] Mari D, Dunand DC. NiTi and NiTi-TiC composites: Transformation and thermal cycling behavior. Metall Mater Trans A 1995;26:2833-47.

[57] Li DS, Zhang XP, Xiong ZP, Mai YW. Lightweight NiTi shape memory alloy based composites with high damping capacity and high strength. J Alloy Compd 2010;490:L15-L9.

[58] Barrado M, Lopez GA, No ML, San Juan J. Composites with ultra high damping capacity based on powder metallurgy shape memory alloys. Mater Sci Eng A 2009;521-22:363-7.

[59] Basu S, Ozaydin MF, Kothalkar A, Karaman I, Radovic M. Phase and morphology evolution in high-temperature Ti_3SiC_2-NiTi diffusion-bonded joints. Scripta Mater 2011;65:237-40.

[60] Gil R, Kennedy AR. Capillarity-Driven Infiltration of Alumina Foams with an Al-Mg Alloy: Processing, Microstructure, and Properties. J Mater Eng Perform 2012;21:714-20.

[61] McWilliams B, Yu J, Klier E, Yen CF. Mechanical response of discontinuous ceramic fiber reinforced metal matrix composites under quasi-static and dynamic loadings. Mater Sci Eng A 2014;590:21-9.

[62] Kouzeli M, Dunand DC. Effect of reinforcement connectivity on the elasto-plastic behavior of aluminum composites containing sub-micron alumina particles. Acta Mater 2003;51:6105-21.

[63] Srivatsan TS, Ibrahim IA, Mohamed FA, Lavernia EJ. Processing techniques for particulate-reinforced metal aluminum matrix composites. J Mater Sci 1991;26:5965-78.

[64] Liu B, Huang WM, Wang HW, Wang ML, Li XF. Study on the load partition behaviors of high particle content B_4C/Al composites in compression. J Compos Mater 2014;48:355-64.

[65] Jung JW, Kang SH. Advances in manufacturing boron carbide-aluminum composites. J Am Ceram Soc 2004;87:47-54.

[66] Hulbert DM, Jiang D, Anselmi-Tamburini U, Unuvar C, Mukherjee AK. Experiments and modeling of spark plasma sintered, functionally graded boron carbide–aluminum composites. Mater Sci Eng A 2008;488:333-8.

[67] Wilkes TE, Young ML, Sepulveda RE, Dunand DC, Faber KT. Composites by aluminum infiltration of porous silicon carbide derived from wood precursors. Scripta Mater 2006;55:1083-6.

[68] McDanels DL. Analysis of stress-strain, fracture, and ductility behavior of aluminum matrix composites containing discontinuous silicon-carbide reinforcement. Metall Trans A 1985;16:1105-15.

[69] Alaneme KK, Aluko AO. Fracture toughness (K_{Ic}) and tensile properties of as-cast and age-hardened aluminium (6063)-silicon carbide particulate composites. Sci Iran 2012;19:992-6.

[70] Wang WJ, Gauthier-Brunet V, Bei GP, Laplanche G, Bonneville J, Joulain A, et al. Powder metallurgy processing and compressive properties of Ti_3AlC_2/Al composites. Mater Sci Eng A 2011;530:168-73.

[71] Guo JM, Wang BS, Chen KX, Zhou HP. Machinable Ti_2AlC ceramics produced by spark plasma sintering. Rare Metal Mater Eng 2007;36:865-8.

[72] Zhou WB, Mei BC, Zhu JQ, Hong XL. Fabrication of high purity dense Ti_2AlC-Ti_3AlC_2 composite by spark plasma sintering method. J Mater Sci 2005;40:3559-60.

[73] Ross RB. Metallic Materials Specification Handbook. 4 ed. London: Chapman & Hall; 1992.

[74] Barsoum MW. The $M_{(n+1)}AX_{(n)}$ phases: A new class of solids; Thermodynamically stable nanolaminates. Prog Solid State Chem 2000;28:201-81.

[75] Wei ZG, Sandstrom R, Miyazaki S. Shape-memory materials and hybrid composites for smart systems - Part I Shape-memory materials. J Mater Sci 1998;33:3743-62.

[76] ASTM. Standard test method for transformation temperature of nickel–titanium alloys by thermal analysis. ASTM International 2004;F2004-05.

[77] Hu L, Benitez R, Basu S, Karaman I, Radovic M. Processing and characterization of porous Ti_2AlC with controlled porosity and pore size. Acta Mater 2012;60:6266-77.

[78] ASTM. Standard test methods for determining average grain size. ASTM International 2013;E112-13.

[79] Gil R, Jinnapat A, Kennedy AR. Pressure-assisted infiltration of molten aluminium into open cell ceramic foams: Experimental observations and infiltration modelling. Compos Pt A 2012;43:880-4.

[80] Mattern A, Huchler B, Staudenecker D, Oberacker R, Nagel A, Hoffmann MJ. Preparation of interpenetrating ceramic-metal composites. J Eur Ceram Soc 2004;24:3399-408.

[81] Fraczkiewicz M, Zhou AG, Barsoum MW. Mechanical damping in porous Ti_3SiC_2. Acta Mater 2006;54:5261-70.

[82] Zhou AG, Barsoum MW, Basu S, Kalidindi SR, El-Raghy T. Incipient and regular kink bands in fully dense and 10 vol.% porous Ti_2AlC. Acta Mater 2006;54:1631-9.

[83] Sun ZM, Murugaiah A, Zhen T, Zhou A, Barsoum MW. Microstructure and mechanical properties of porous Ti_3SiC_2. Acta Mater 2005;53:4359-66.

[84] Brodnikovskii NP, Burka MP, Verbilo DG, Demidik AN, Ivanova, II, Koval AY, et al. Structure and mechanical properties of porous titanosilicon carbide Ti_3SiC_2. Powder Metall Met Ceram 2003;42:424-32.

[85] Ziqi S, Ying L, Meishuan L, Yanchun Z. Preparation of reticulated MAX-phase support with morphology-controllable nanostructured ceria coating for gas exhaust catalyst devices. J Am Ceram Soc 2010;93:2591-7.

[86] Polonsky L, Lipson S, Markus H. Lightweight cellular metal. Modern Cast 1961;39:57-9.

[87] San Marchi C, Mortensen A. Deformation of open-cell aluminum foam. Acta Mater 2001;49:3959-69.

[88] Despois JF, Marmottant A, Conde Y, Goodall R, Salvo L, San Marchi C, et al. Microstructural tailoring of open-pore microcellular aluminium by replication processing. In: Umakoshi Y, Fujimoto S, editors. Advanced Structural and Functional Materials Design, Proceedings. Zurich-Uetikon, Switzerland: Trans Tech Publications Ltd; 2006. p. 281-8.

[89] Zhao Y, Sun D. A novel sintering-dissolution process for manufacturing Al foams. Scripta Mater 2001;44:105-10.

[90] Bansiddhi A, Dunand DC. Shape memory NiTi foams produced by replication of NaCl space holders. Acta Biomater 2008;4:1996-2007.

[91] Bansiddhi A, Dunand DC. Shape-memory NiTi-Nb foams. J Mater Res 2009;24:2107-17.

[92] Ye B, Dunand DC. Titanium foams produced by solid-state replication of NaCl powders. Mater Sci Eng A 2010;528:691-7.

[93] Pekala RW, Hopper RW. Low-density microcellular carbon foams. J Mater Sci 1987;22:1840-4.

[94] Fitzgerald TJ, Michaud VJ, Mortensen A. Processing of microcellular SiC foams: Ceramic foam production. J Mater Sci 1995;30:1037-45.

[95] Radovic M, Lara-Curzio E. Elastic properties of nickel-based anodes for solid oxide fuel cells as a function of the fraction of reduced NiO. J Am Ceram Soc 2004;87:2242-6.

[96] Radovic M, Barsoum MW, Ganguly A, Zhen T, Finkel P, Kalidindi SR, et al. On the elastic properties and mechanical damping of Ti_3SiC_2, Ti_3GeC_2, $Ti_3Si_{0.5}Al_{0.5}C_2$ and Ti_2AlC in the 300-1573 K temperature range. Acta Mater 2006;54:2757-67.

[97] Migliori A, Sarrao, JL. Resonant ultrasound spectroscopy: applications to physics, materials measurements, and nondestructive evaluation. New York: John Wiley; 1997.

[98] Radovic M, Lara-Curzio E, Riester L. Comparison of different experimental techniques for determination of elastic properties of solids. Mater Sci Eng A 2004;368:56-70.

[99] Spencer CB, Cordoba JM, Obando N, Sakulich A, Radovic M, Oden M, et al. Phase evaluation in Al_2O_3 fiber-reinforced Ti_2AlC during sintering in the 1300-1500 ^oC temperature range. J Am Ceram Soc 2011;94:3327-34.

[100] Turkdogan E. Physical chemistry of high-temperature technology. New York: Academic Press; 1980.

[101] Barin I, Knacke, O. Thermochemical properties of inorganic substances. Berlin, Germany and New York, USA: Springer-Verlag; 1973.

[102] Sun ZM, Li S, Ahuja R, Schneider JM. Calculated elastic properties of M_2AlC (M = Ti, V, Cr, Nb and Ta). Solid State Commun 2004;129:589-92.

[103] Spriggs RM. Expression for effect of porosity on elastic modulus of polycrystalline refractory materials, particularly alumium oxide. J Am Ceram Soc 1961;44:628-9.

[104] Knudsen FP. Effect of porosity on Young modulus of alumina. J Am Ceram Soc 1962;45:94-5.

[105] Hasselman DPH. On the porosity dependence of the elastic moduli of polycrystalline refractory materials. J Am Ceram Soc 1962;45:452-3.

[106] Hashin Z. Elasticity of ceramic systems. Boulder, CO: Westview Press; 1977.

[107] Ramakrishnan N, Arunachalam VS. Effective elastic-moduli of porous solids. J Mater Sci 1990;25:3930-7.

[108] Ramakrishnan N, Arunachalam VS. Effective elastic-moduli of porous ceramic materials. J Am Ceram Soc 1993;76:2745-52.

[109] Rice R. Porosity of ceramics. New York: Marcel Dekker; 1998.

[110] Hu L, Wang CA. Effect of sintering temperature on compressive strength of porous yttria-stabilized zirconia ceramics. Ceram Int 2010;36:1697-701.

[111] Saito S. Fine ceramics. New York: Elsevier; 1988.

[112] Griffith AA. The phenomena of rapture and flow in solids. Phil Trans R Soc Lond 1920;A221:163-198.

[113] Hu L, Wang CA, Huang Y. Porous YSZ ceramics with unidirectionally aligned pore channel structure: Lowering thermal conductivity by silica aerogels impregnation. J Eur Ceram Soc 2011;31:2915-22.

[114] Bruggeman DAG. Calculation of various physics constants in heterogenous substances I: Dielectricity constants and conductivity of mixed bodies from isotropic substances. Ann Phys-Berlin 1935;24:636-64.

[115] Hashin Z, Shtrikman S. A variational approach to theory of effective magnetic permeability of multiphase materials. J Appl Phys 1962;33:3125-35.

[116] Hu L, Wang CA, Huang Y. Porous yttria-stabilized zirconia ceramics with ultra-low thermal conductivity. J Mater Sci 2010;45:3242-6.

[117] Hu L, Wang CA, Hu ZJ, Lu S, Sun CC, Huang Y. Porous yttria-stabilized zirconia ceramics with ultra-low thermal conductivity. Part II: temperature dependence of thermophysical properties. J Mater Sci 2011;46:623-8.

[118] Hu L, Wang CA, Huang Y, Sun CC, Lu S, Hu ZJ. Control of pore channel size during freeze casting of porous YSZ ceramics with unidirectionally aligned channels using different freezing temperatures. J Eur Ceram Soc 2010;30:3389-96.

[119] Sun ZM. Progress in research and development on MAX phases: a family of layered ternary compounds. Int Mater Rev 2011;56:143-66.

[120] Carson JK, Lovatt SJ, Tanner DJ, Cleland AC. Thermal conductivity bounds for isotropic, porous materials. Int J Heat Mass Transfer 2005;48:2150-8.

[121] Landauer R. The electrical resistance of binary metallic mixtures. J Appl Phys 1952;23:779-84.

[122] ASTM. Standard test methods for apparent porosity, water absorption, apparent specific gravity, and bulk density of burned refractory brick and shapes by boiling water. ASTM International 2010;C20-00.

[123] Launey ME, Munch E, Alsem DH, Saiz E, Tomsia AP, Ritchie RO. A novel biomimetic approach to the design of high-performance ceramic-metal composites. J R Soc Interface 2010;7:741-53.

[124] Viala JC, Peillon N, Bosselet F, Bouix J. Phase equilibria at 1000 degrees C in the Al-C-Si-Ti quaternary system: an experimental approach. Mater Sci Eng A 1997;229:95-113.

[125] Park JK, Lucas JP. Moisture effect on SiC_p/6061 Al MMC: Dissolution of interfacial Al_4C_3. Scripta Mater 1997;37:511-6.

[126] Gu WL, Yan CK, Zhou YC. Reactions between Al and Ti_3SiC_2 in temperature range of 600-650 degrees C. Scripta Mater 2003;49:1075-80.

[127] El-Raghy T, Barsoum MW, Sika M. Reaction of Al with Ti_3SiC_2 in the 800-1000 degrees C temperature range. Mater Sci Eng A 2001;298:174-8.

[128] Zhang J, Zhou YC. Microstructure, mechanical, and electrical properties of Cu-Ti_3AlC_2 and in situ Cu-TiC_x composites. J Mater Res 2008;23:924-32.

[129] Jones NG, Humphrey C, Connor LD, Wilhelmsson O, Hultman L, Stone HJ, et al. On the relevance of kinking to reversible hysteresis in MAX phases. Acta Mater 2014;69:149-61.

[130] Callister Jr. W, Rethwisch D. Materials Science and Engineering: An Introduction. New York: John Wiley and Sons; 2014.

[131] Guo JM, Wang BS, Chen KX, Zhou HP. Machinable Ti_2AlC ceramics produced by spark plasma sintering. Rare Metal Mat Eng 2007;36:865-8.

[132] El-Raghy T, Barsoum MW. Diffusion kinetics of the carburization and silicidation of Ti_3SiC_2. J Appl Phys 1998;83:112-9.

[133] Du Y, He CY, Schuster JC, Liu SH, Xu HH. Thermodynamic description of the Ni-Si-Ti ternary system. Int J Mater Res 2006;97:543-55.

[134] Spencer CB, Cordoba JM, Obando NH, Radovic M, Oden M, Hultman L, et al. The reactivity of Ti_2AlC and Ti_3SiC_2 with SiC fibers and powders up to temperatures of 1550 degrees C. J Am Ceram Soc 2011;94:1737-43.

[135] Lee KJ, Nash P. The Ni-P (Nickel-Phosphorus) System, Phase Diagrams of Binary Nickel Alloys, P. Nash, Ed., ASM International, Materials Park, OH, 1991, p 235-246J Phase Equilib 1991;12:551-62.

[136] Huneau B, Ding JJ, Rogl P, Bauer J, Ding XY, Bohn M. Experimental investigation in the quaternary systems Ti-Ni-Al-N and Ti-Ni-Al-O. J Solid State Chem 2000;155:71-7.

[137] Huneau B, Rogl P, Zeng K, Schmid-Fetzer R, Bohn M, Bauer J. The ternary system Al-Ni-Ti Part I: Isothermal section at 900 ^oC; Experimental investigation and thermodynamic calculation. Intermetallics 1999;7:1337-45.

[138] Grytsiv A, Ding JJ, Rogl P, Weill F, Chevalier B, Etourneau J, et al. Crystal chemistry of the G-phases in the systems Ti-{Fe, Co, Ni}-Al with a novel filled variant of the Th_6Mn_{23}-type. Intermetallics 2003;11:351-9.

[139] Grytsiv A, Rogl P, Schmidt H, Giester G, Hundegger P, Wiesinger G, et al. Formation and crystal chemistry of cubic ternary phases with filled Th_6Mn_{23}-type and $AuCu_3$-type in the systems Ti-M^{VIII}-Al. Intermetallics 2004;12:563-77.

[140] Otsuka K, Ren X. Physical metallurgy of Ti-Ni-based shape memory alloys. Prog Mater Sci 2005;50:511-678.

[141] Hale DK. The physical properties of composite materials. J Mater Sci 1976;11:2105-41.

[142] Benveniste Y, Miloh T. The effective conductivity of composites with imperfect thermal contact at constituent interfaces. Inter J Eng Sci 1986;24:1537-52.

[143] Böhm HJ, Nogales S. Mori-Tanaka models for the thermal conductivity of composites with interfacial resistance and particle size distributions. Comp Sci Tech 2008;68:1181-7.

[144] Dunn ML, Taya M. The effective thermal conductivity of composites with coated reinforcement and the application to imperfect interfaces. J Appl Phys 1993;73:1711-22.

[145] Barsoum MW, El-Raghy T, Rawn CJ, Porter WD, Wang H, Payzant EA, et al. Thermal properties of Ti_3SiC_2. J Phys Chem Solids 1999;60:429-39.

[146] Smith JF, Lück R, Jiang Q, Predel B. The heat capacity of solid Ni-Ti alloys in the temperature range 120 to 800 K. J Phase Equil 1993;14:494-500.

[147] Knacke O, Kubaschewski O, Haesselmann K. Thermochemical properties of inorganic substances. Berlin, Germany: Springer; 1991.

[148] Berman HA, West ED, Rozner AG. Anomalous heat capacity of TiNi. J Appl Phy 1967;38:4473-6.

[149] Zanotti C, Giuliani P, Chrysanthou A. Martensitic-austenitic phase transformation of Ni-Ti SMAs: Thermal properties. Intermetallics 2012;24:106-14.

[150] Chirtoc M, Gibkes J, Wernhardt R, Pelzl J, Wieck A. Temperature-dependent quantitative 3 omega scanning thermal microscopy: Local thermal conductivity changes in NiTi microstructures induced by martensite-austenite phase transition. Rev Sci Instrum 2008;79.

[151] Barsoum MW, El-Raghy T. Synthesis and characterization of a remarkable ceramic: Ti_3SiC_2. J Am Ceram Soc 1996;79:1953-6.

[152] Goff JF. Dependence of tranport properties of transition metal alloys and compounds on the electron number. J Appl Phys 1968;39:2208-12.

[153] Terada Y, Ohkubo K, Mohri T, Suzuki T. Thermal conductivity of intermetallic compounds with metallic bonding. Mater Trans 2002;43:3167-76.

[154] Collected Papers of P.L. Kapitza, edited by ter Haar D; Oxford, UK: Pergamon Press; Vol.1, 1964.

[155] Hasselman DPH, Johnson LF. Effective thermal conductivity of composites with interfacial thermal barrier resistance. J Comp Mater 1987;21:508-15.